The Dissertation Committee for Sukant Khurana certifies that this is the approved version of the following dissertation:

ROLES OF VOLTAGE-GATED ION CHANNELS IN REGULATING THE RESPONSES OF PRINCIPAL NEURONS OF THE MEDIAL SUPERIOR OLIVE

Committee:

_____

Nace Golding, Supervisor

_____

Dennis McFadden

_____

Richard Aldrich

_____

Harold Zakon

_____

Hitoshi Morikawa

ROLES OF VOLTAGE-GATED ION CHANNELS IN REGULATING

THE RESPONSES OF PRINCIPAL NEURONS OF THE MEDIAL

SUPERIOR OLIVE

by

Sukant Khurana, M.S.; B.Sc. (Hons.)

Dissertation

Presented to the Faculty of the Graduate School of
The University of Texas at Austin
in Partial Fulfillment
of the Requirements
for the Degree of

Doctor of Philosophy

The University of Texas at Austin,
December 2009

Dedication

To the foolhardy notion, that we will understand the functioning of brain in a "meaningful way"*, of at least one smart animal** in my lifetime.

* The definition of meaningful is subject to change and based on convenience.
** Need not be the "mind" of the naked ape or a specially blessed rodent.

Acknowledgements

conductance and low voltage activated potassium conductance, in form of a point-neuron model) presented in this thesis was done in close collaboration with Dr. Michiel Remme and Prof. John Rinzel, at New York University. Collaboration with Michiel is currently resulting in the exploration of role of dendretic processing in auditory physiology, which is extension of work presented in this thesis.

The highlights of PhD experience at UT have been those "it's funny" moments (usually referred to as the "Eureka moments", by people who have decided to be an authority on declaring themselves to be an authority in a certain field, which by the nature of it's exclusiveness, is no one else's concern, except for the almighty self proclaimed authority). It remains to be seen if those funny moments will make any difference to the study of neuroscience or science in general.

ROLES OF VOLTAGE-GATED ION CHANNELS IN REGULATING THE

RESPONSES OF PRINCIPAL NEURONS OF THE MEDIAL SUPERIOR OLIVE

Sukant Khurana, Ph.D.
The University of Texas at Austin, 2009

Supervisor: Nace Golding

The principal neurons of the medial superior olive (MSO) are considered to be responsible for transforming the temporal information present in the binaural acoustic stimulus into an output encoding sound location along the horizontal axis. Spatial resolution of sound localization depends critically on the time resolution with which MSO neurons can detect microsecond differences in the timing of inputs from the two ears. This fast temporal processing is contingent on voltage gated ion channels. The work presented in this thesis demonstrates that two currents, namely a hyperpolarization activated cationic current and low voltage activated potassium current dynamically interact to regulate the intrinsic time resolution of MSO neurons. We observe that the ability of MSO neurons to perform sub-millisecond temporal processing matures after birth, especially around the time of the clearing of the auditory canal. Hyperpolarization activated cationic current was found to be one of the underlying mechanisms transforming slow immature MSO neurons into temporally precise adult MSO neurons.

Table of Contents

List of Figures

PROLOGUE

"Men trust their ears less than their eyes." - Herodotus

"Our problem is that sound is not important in our culture. We know the world from the visual, not from the other senses. I had to be taught other ways of understanding." - Bernie Krause, sound recordist.

Humans like all other mammals rely on multisensory information for their survival, but we tend to know the world more through visual senses. Nonetheless the need for auditory stimulus for human existence becomes quite obvious in the case of deafness.

"The problems of deafness are deeper and more complex, if not more important than those of blindness. Deafness is a much worse misfortune. For it means the loss of the most vital stimulus - the sound of the voice that brings language, sets thoughts astir, and keeps us in the intellectual company of man. ……… Blindess separates us from things but deafness separates us from people."   - Helen Keller

Whether the apparent visual preference, in our understanding of the world is cultural or biological is not entirely obvious. Many other cultures, other than the contemporary western culture, tend to pay more attention to sound, as evinced by creation myths, multitude of tonal languages and the use of music in everyday activities.

The pre Judaic-Christian-Islamic Babylonianís religion spoke of a "lil", that existed between heaven and earth: "a word which the nearest meaning would be wind, air, breath, or spirit; its essential characteristics seem to have been...movement and expansion" (Doresse, 1986). The Jewish mystical tradition – Kabballa, further extends the role of sound in creation.

In the greater Indies (originally a British colonial term, now frequently used in a historical sense by Indologists; encompassing "hither India", i.e. South Asia and "further India", encompassing most of South East Asia), the sound seems to play an important role in everyday life, as evinced by multiple creation myths. Lord Shiva is said to have heard the anahad nada, the original sound of creation of universe, during samadhi in the Himalayas. Many eastern creation stories start with the word "Om".

"And whatever else that transcends threefold time - that, too, is just the word Om." (Mandukya Upanisad)

The fact that a significant number of non-Indo-European languages are tonal, underlines the emphasis of sounds in various cultures.

All that, is not to say that Western tradition does not have appreciation of non-visual senses, as evinced by the below mentioned quote from Shakespeare or rich masterpieces created by Ludwig Van Beethoven; but a shift both in the popular culture and scientific attitude is needed for a richer understanding of sensory perception.

"Warble, child, make passionate my sense of hearing." - William Shakespeare. Armado, in Love's Labor's Lost, act 3, sc. 1, l. 1.

Chapter 1

INTRODUCTION

Whether it be our ability to understand the speech of one person in a noisy environment – the cocktail party problem (Cherry, 1953; Kuyper, 1972; Jones and Litovsky, 2008) or the ability of a barn owl to localize prey in complete darkness, an animal's ability to localize sound sources is vital to the survival of the individual. Unlike the retina, where there is a spatial map of the world, the auditory system has to extract the spatial information from the amplitude, frequency and temporal information present in the accoustic stimulus. Both monaural and binaural cues are used by the auditory system to extract the spatial location of the sound sources. Although binaural cues are considered to be the predominant cues for the localization of sound along the azimuthal axis, there can exist sufficient information in the monaural cues for sound source localization.

Inter-aural time disparity cues

In the 19th century Lord Rayleigh explored the acoustical cues for sound localization. Employing tuning forks, he used pure-tone stimuli for most of his experiments (Rayleigh, 1877; Rayleigh, 1937). He observed that in human

subjects, the primary cue for localization of sound frequencies above 1500 Hz was the inter-aural difference in sound-pressure levels (Interaural level disparities: ILDs). Using a pair of mistuned low-frequency tuning forks, Rayleigh established that humans are sensitive to inter-aural differences in the binaural disparities in the time of arrival of low-frequency sounds (Interaural time disparities: ITDs). Indeed, modern psychophysical studies show that the sensitivity to ongoing (not onset) ITDs is limited to frequencies below about 1.3 kHz for pure tones but not complex, real world broadband sounds (Hughes, 1940). Rayleigh's understanding of the use of two acoustical cues in different, but as we now know, overlapping frequency domains for localization of tones in the azimuthal dimension has come to be known as the ''Duplex Theory'' of sound localization. This theory is primarily relevant for pure tone stimuli.

Many studies demonstrate that ITDs dominate listeners' judgments of the location of broadband sound sources that contain low-frequency components (Wightman and Kistler, 1992). Even an imposition of an ILD imbalance of 10–20 dB had little impact on azimuthal sound localization (Wightman and Kistler, 1992). Abundant evidence exists, demonstrating that the auditory system is capable of extracting temporal information from the envelopes of higher-frequency sounds that contain multiple frequency components (Henning, 1974; McFadden and Pasanen, 1975; McFadden and Pasanen, 1976).

Unlike the pure tones used to establish the duplex theory, most sounds in the

5

real world have bandwidths of several octaves, and a listener is rarely exposed to a pure tone. ITDs are valid cue for the entire audible sound spectrum, with cycle-by-cycle differences at low frequencies and envelope time differences across the spectrum being used for sound localization.

Adaptations of the auditory system for preserving binaural temporal information

The auditory system has many interesting structural specializations in the periphery, adaptations in the circuitry, synaptic, and cellular properties to encode, transmit and transform the timing information present in the sound stimuli (Pickles, 2008; Wang and Brown, 2006; Oertel, 1997; Oertel, 1999; Trussell, 1999).

Apart from processing the inter-aural time differences for binaural sound source localization listeners use temporal cues in the encoding of low frequency information in language processing – the vowel sounds. When the basilar membrane vibrates in response to signals, below about 4 kHz, the hair cells in the region of vibration exhibit an alternating excitation-inhibition at the frequencies of vibration, which in turn generates action potentials (APs) in the auditory nerve (AN) fibers attached to the inner hair cells. For a simple sine wave, the impulses are generated around a particular point on the sine-wave

cycle, a process that is referred to as phase-locking. Because of the refractory period in the action potential firing, an AN fiber cannot respond to every successive cycle of a stimulus. When it responds, however, it does so around a constant phase angle of the stimulus resulting in impulses around integral multiples of the period of the sine-wave stimulus. When populations of AN fibers phase lock to same stimulus the time sequence of AN fibers spiking is called volleying. Each fiber is incapable of responding to every cycle of the stimulus, but collectively they fire on each cycle.

The spherical bushy cells (SBC) are a subpopulation of neurons in the anterior ventral cochlear nucleus (AVCN) that convey well-preserved phase-locked excitatory synaptic information from the ANs bilaterally to the medial superior olive (MSO). MSO is the first binaural brainstem nucleus receiving intensity-resistant ITD information (Goldberg and Brown, 1969; Yin and Chan, 1990). Although it should be noted that the cells of the lateral superior olive (LSO), an adjacent nucleus, are also sensitive to ITDs of the envelope of sinusoidally amplitude-modulated signals below a modulation frequency of 800 Hz (Joris and Yin, 1998). Medial superior olive neurons are known for phasic responses to intracellular square pulse injections and brief responses to coincident binaural excitation (Moushegian et al., 1967; Smith, 1995; Scott et al., 2005). Well-timed inhibitory inputs from the Medial nucleus of the trapezoid body (MNTB) also synapse on to the MSO neurons (Oertel, 1997). Globular bushy cells in the ventral cochlear nucleus send axons to the contralateral MNTB, where they

synapse via the calyx of Held on the MNTB principle cells. The Calyx of Held are the largest synapse in the brain (Morest, 1968) named, due to its flower-petal like shape and are adapted for fast, efficient transportation of information from one cell to the next. The related end bulbs of Held are synapses between AN and the bushy cells of cochlear nucleus. Though smaller in size, like the calyx of Held these synapses promote fast and efficient information transfer (Trussell, 1999). Lateral nucleus of the trapezoid body (LNTB) provides another inhibitory input to MSO (Oertel, 1997; Oertel, 1999). The role of this input is currently being explored, but preliminary results suggest that it is likely playing a role in the regulation of excitability of MSO neurons and may not be temporally as precise as the MNTB inputs (Personal communication by Dr. Michael Roberts, Wenke Li, and Dr. Nace Golding).

In the avian auditory system large size of the excitatory post synaptic potential (EPSP) in nucleus magnocellularis (an analogous nucleus to cochlear nucleus) ensures uniform latencies by reducing the time required to reach threshold for spiking, thus reducing the variability or the jitter in the synaptic transmission (Zhang and Trussell, 1994; Trussell, 1999).

All the modifications in synaptic transmission would be of no use if the post-synaptic neurons of the auditory brainstem circuitry did not have mechanisms to ensure the reliable transmission of the temporally precise information. The neurons in these pathways, including the MSO, exhibit many biophysical

specializations, like adaptations in the voltage-gated ion channels and the dendritic morphology that enables them to signal robustly with little temporal jitter (Scott et al., 2005; Agmon-Snir et al., 1998) (Mathews et al., in review, personal communication). In the medial superior olive, two major currents, a low-voltage-activated potassium current (I_{K-LVA}) and a hyperpolarization activated cyclic nucleotide gated current called I_h (h for hyperpolarization-activated), shape the responses of neurons. I_{K-LVA} is known to enhance the phase-locking, increase the signal-to-noise ratio, and limit the spiking of neurons, enabling phasic responses (Bal and Oertel, 2001; Golding et al., 1995; Kuba et al., 2002; Kuba et al., 2005; Rothman and Manis, 2003; Rothman and Manis, 2003; Scott et al., 2005; Zhao and Wu, 2001; Svirskis et al., 2002; Day et al., 2008) (Mathews, personal communication).

Computational models of ITD detection

In a seminal paper published in 1948, Jeffress proposed a scheme to transform acoustic timing difference into a spatial map of neural activity (Jeffress, 1948). Many of the key assumptions of this model have been confirmed over the years, particularly in birds. The Jeffress model has three key assumptions: (1) there exists a binaural channel that receives convergent information from monaural channels containing temporal information from the left and right ears; (2) cells in that binaural nucleus discharge only when they receive coincident inputs from

monaural inputs and (3) the monaural channels project with ladder-like branching patterns forming delay lines of various conduction delays to different binaural channels, making a spatial map of the binaural channels that fire in response to different sound differences.

MSO is the first site for ITD encoding in mammals. Many pieces of evidence support the original Jeffress model. Phase-locked inputs from the AN fibers are transmitted through the bushy cells of AVCN to the MSO. In fact, phase locking in bushy cells is more precise than in the AN fibers (Joris et al., 1994). The enhancement in phase locking is considered to be due to the convergence of AN inputs in the bushy cells (Joris et al., 1994). Bushy cell axons are known to project bilaterally to MSO in cats (Smith et al., 1993; Beckius et al., 1999). Evidence for delay lines in mammals comes from cats (Smith et al., 1993; Beckius et al., 1999). Smith *et al*. found that the contralateral afferents exhibited delay-line-like architecture but not the ipsilateral ones. It is important to note that the model still works with one-sided delay line. In chicks and barn owlsa ladder-like equally forked configuration of both ipsi- and contralateral afferents has been observed (Young and Rubel, 1983; Carr and Konishi, 1988; Carr and Konishi, 1990).

Characteristic frequency is the frequency that evokes maximal spiking in cells. In the inferior colliculus (IC) the best delay on average is small at the higher characteristic frequency and large at the lower characteristic frequency

(McAlpine et al., 2001; Hancock and Delgutte, 2004). To fit the Jeffress model, these findings would imply longer axonal delay lines at the lower characteristic frequencies than at the higher characteristic frequencies. The MSO performs cross-correlation over narrow frequency bands. Given the cochlear tonotopy, converging inputs encoding sounds of different frequencies can potentially trigger post-synaptic excitation with different temporal delays. A timing mismatch because of the underlying slight frequency mismatch from the two channels can result in an additional twist for the cross correlation model. Thus an alternative model of ITD-detection based on a bilateral mismatch in frequency tuning, called the 'stereausis' model has been advanced in recent years (Joris et al., 2006; Fischer and Peña, 2009), although a thorough validation is far from complete.

Inhibition seems to play an important role in the functioning of the MSO. Pharmacological blocking of the inhibitory inputs results in drastic shifts in the ITD encoding, thus leading to speculations about the importance of the precise timing of inhibition (McAlpine and Palmer, 2002; Brand et al., 2002; Pecka et al., 2008). Despite the differing opinions amongst the supporters of different models of ITD detection, all agree on the coincidence of the excitatory inputs arriving from binaural cochlear nucleus neurons arriving on the separate dendrites of the MSO. This makes the exploration of the synaptic integration properties of MSO relevant independent of the exact model of ITD computation in consideration.

Given that many post-natal developmental changes in the auditory system of gerbils occur around the clearance of auditory canal, laying a foundation of the developmental changes in the cellular properties of MSO is also very important before one can ask the role of hearing in shaping the development of MSO. In gerbils the auditory canal opens around post–natal day (PND) 12. Before the time of clearance of auditory canal there is bone conduction of sounds but low intensity hearing starts only after the clearance of auditory canal. From here on we refer to the clearance of auditory canal as "hearing onset", though one should keep in mind that hearing thresholds gradually reach mature levels in around ten days after clearance of auditory canal. All my research has been done using patch-clamp recordings of MSO neurons in the brain slices obtained from Mongolian Gerbils (*Meriones unguiculatus*). Given that I_h and I_{K-LVA} are two of the major determinants of MSO neuron properties, yet there is almost no knowledge of I_h in MSO, I have made I_h the focus of my research. In the remaining introduction, I will elaborate on MSO development and I_h properties, which should enable the reader to put the experimental results in a proper perspective.

Post-natal development of auditory brainstem, especially MSO

Around the hearing onset many changes in the auditory system are taking place, including in the auditory brainstem. Apart from hearing onset, a second change

that is more progressive and continues even later in development than few days of hearing onset is an increase in the head size. This increase in the head size corresponds to continuous changes in the ITDs. During this postnatal development there are changes in the kinetics of synaptic responses, refinement of synaptic projections, maturation of circuitry, axonal conduction velocities, active properties of neurons and intracellular ionic concentrations, which will determine the impact of a synaptic conductance on MSO responses.

Before assuming that MSO cells are experiencing changes in ITD one should consider data from one human study. In humans a dramatic increase in the conduction velocity from cochlear nucleus to the MSO (as measured by the interval between 3rd and 4th peak of ABR, reflecting the asynaptic path) more than compensates for the increase in the skull size during post-natal development (Moore et al., 1996). This is an example of change in the axonal conduction velocity during development. The underlying mechanism in the speeding of conduction velocity may be in axonal morphology, active properties, increased myelination, or combination of all three. These mechanistic questions remain to be explored.

Many synaptic properties, like kinetics change over development enable fast temporal processing abilities of the mature auditory system. In gerbil MSO, the inhibitory synaptic inputs become fast in kinetics due to the synchronization of miniature IPSPs during postnatal development (Magnusson et al., 2005). During

postnatal development in rats, the AMPA subunits in the superior olivary complex also undergo changes (Caicedo and Eybalin, 1999).

Apart from changes in the synaptic properties, the projections of different inputs to MSO and the output target of the MSO change over the post–natal development. Before the hearing onset the inhibitory inputs are present both on the soma and the dendrites. After auditory experience inhibitory inputs becomes perisomatic and exhibit refinement in the distribution across tonotopic axis of MSO (Sanes and Takács, 1993; Werthat et al., 2008). These changes occur in a sensory experience dependant manner (Sanes and Takács, 1993; Werthat et al., 2008). In the adult MSO, excitatory synaptic projections from the ipsi-lateral AVCN side project to the lateral dendrite of the MSO, while from the contra-lateral side to the medial dendrite. This connection specificity also seems to be developmentally refined like that of the inhibitory connections. Unilateral cochlear damage manifests in synaptic contacts from the un-ablated cochlea projecting to both the dendretic branches (Kitzes et al., 1995). Even the projections of MSO are undergoing maturation during this period. One retrograde tracing study suggests that a majority of the MSO neurons meet their post-synaptic target only during the post-natal development (Okoyama et al., 1995).

Even the cellular morphology is not immune to developmental plasticity. The dendrites of the MSO neurons in gerbils reduce in the complexity of dendretic branching after hearing onset (Chirila et al., 2007; Rautenberg et al., 2009). Even

14

though the volume of the MSO neurons increases after hearing onset, the total surface area decreases, contributing to faster membrane time constants in the mature MSO neurons (Rautenberg et al., 2009). Unilateral cochlear removal has been shown to result in dendretic atrophy on the ablated side, especially in the caudal MSO gerbils, suggesting that sensory activity is required in governing even the cellular morphology (Russell and Moore, 1999).

Apart from changes in morphology, synaptic properties, many cellular properties of MSO neurons are likely to undergo developmental plasticity. The change in the polarity of synaptic inputs is one such drastic developmental maturation. Glycinergic and GABAergic transmission shifts from depolarizing to hyperpolarizing during pre-hearing development (Kullmann and Kandler, 2001), along with corresponding changes in the expression levels of chloride transporters (Becker et al., 2003).

Apart from all the above-mentioned changes the voltage-gated ion channels are also likely to undergo maturation with development. Nonetheless there is only one published study broaching this issue (Scott et al., 2005). There is a significant increase in the conductance of the low-voltage-gated potassium channels after the hearing onset (Scott et al., 2005), though currently no knowledge in available of the pre–hearing MSO.

Taken together, the emerging evidence alters the old view of a robust, inflexible brainstem, with cortex having the sole or at least the lion's share of plasticity to cope with changing sensory world.

Almost all the changes in MSO properties seem to be tightly correlated with changes in the sensory inputs. Also disruption of the sensory inputs alters the projections of the inhibitory (Werthat et al., 2008) and the excitatory inputs (Kitzes et al., 1995), and even the cellular morphology (Russell and Moore, 1999). ITD curves of animals raised in omini-directional sound (measured in DNLL, a projection area of MSO) are akin to younger animals with limited auditory experience, suggesting a crucial role of auditory experience in shaping MSO neuron properties (Seidl and Grothe, 2005). In an adjoining nucleus of the lateral superior olive (LSO), sensory deprivation by the means of contralateral cochlear ablation causes a transient increase in the I_h conductance (g_h). Thus MSO may be an excellent preparation for understanding the role of sensory activity in development.

Physiology and function of I_h

The molecular substrates for I_h are Hyperpolarization-activated, Cyclic Nucleotide–sensitive, Cation Non-selective channels (abbreviated to HCN) (Santoro and Tibbs, 1999): from HCN1 to 4 in mammals (Santoro et al., 1997;

16

Santoro et al., 1998; Ludwig et al., 1998). The term Cyclic Nucleotide–sensitive, in HCN comes from the known role of cyclic-adenosine-monophosphate (cAMP) regulation of the kinetics and voltage dependence of I_h activation. Unlike many other voltage-gated ion channels, HCN channels open in response to hyperpolarization. HCN channels show a preference in permeability to potassium over sodium such that the reversal potential is around -35 mV. Thus, at rest, the opening of HCN channels results in an inward current. Hormones and transmitters can induce a significant shift in the voltage dependence of I_h activation (DiFrancesco and Mangoni, 1994; Pape, 1996). Modulation of cardiac pacemaking by norepinephrine, through alterations in cAMP pathway is one example of hormonal regulation of I_h (Maccaferri and McBain, 1996). I_h was first described in the Sinoatrial node of heart (DiFrancesco, 1984; DiFrancesco, 1984; Hagiwara and Irisawa, 1989) and in calf purkinje neurons (DiFrancesco, 1981; DiFrancesco, 1981). I_h is also described as I_f (f for funny) in heart. It is now known that the underlying channels for I_h and I_f are the same HCN channels (Santoro and Tibbs, 1999).

HCN channels play various roles in different neuron types. In some neurons, like thalamocortical neurons, the HCN channels play a genuine pacemaking role as after-hyperpolarization following the AP activates I_h, which depolarizes the cells to back to the AP threshold (Pape, 1996). In some other neurons, like cerebellar Purkinje neurons, HCN channels counteract long lasting inhibition, which would otherwise inhibit burst firing (Williams et al., 2002), thus enabling membrane

potentials to be in the range amenable for other channels to control pacemaking (Robinson and Siegelbaum, 2003). HCN channels, present in increasing density in the distal dendrites of *Cornu Ammonis* 1 (CA1) pyramidal neurons of hippocampus, have been shown to play a role in synaptic normalization of EPSPs by active hyperpolarization in response to depolarization and also by providing more shunt with increasing length in the dendrites (Magee, 1998; Magee, 1999). Actin-dependent interaction of HCN channels in the crayfish neuromuscular junctions has been suggested to play a role in the synaptic plasticity (Beaumont and Zucker, 2000; Beaumont et al., 2002). Recently, the sub-threshold resonance frequency of CA1 pyramidal neurons was found to be distance dependent, increasing with increase in g_h (Narayanan and Johnston, 2007). These location-dependent changes in channel densities confer an ability to differentially regulate internal time delays within neurons, potentially providing a mechanism to have temporal control over synaptic integration (Narayanan and Johnston, 2008).

Expression of HCN subunits

There have been a few studies exploring the expression of different HCN subunits in whole brain sections in mice and rats at transcript level, using *in-situ hybridization* (Santoro et al., 1997; Moosmang et al., 1999; Santoro et al., 2000) and one study exploring protein levels using immunohistochemistry approaches

(Notomi and Shigemoto, 2004). There is little data on the expression of HCN subunits in MSO, but detailed information from many other brainstem neurons is available. HCN1 is predominant in the neocortex, the hippocampus, and the cerebellar cortex. Using antibody staining, Leao et al. found high expression in the LSO and the anterior-ventral cochlear nucleus (AVCN) (Leao et al., 2005). The LSO, the ventral nucleus of lateral leminiscus (VNLL), the octopus neurons and the bushy cells of ventral cochlear nucleus (VCN), a subpopulation of neurons in central nucleus of inferior colliculus and to a lesser extent the MNTB express HCN1, as explored by the use of antibody staining (Koch et al., 2004). The above-mentioned study (Koch et al., 2004) on auditory brainstem of rats (P20-30) claimed that HCN1 is expressed in significant amounts in MSO, although the published image quality did not lend itself to an objective judgment of the subunit composition. The subunit analysis in auditory brainstem has been conducted on rats, where the MSO is diminutive and considered vestigial in mature animals, leaving the question of exact nature of HCN subunits in MSO, to be an open one.

The pattern of HCN2 expression is more ubiquitous with the highest density in the thalamus and the brainstem. HCN2 staining has been observed in the MNTB, the dorsal nucleus of lateral leminisus (DNLL), the bushy cells of VCN and a subpopulation of neurons in the central nucleus of the inferior colliculus (Koch et al., 2004). HCN3 is expressed in the central nervous system (CNS) only at low levels, with significant expression in the olfactory bulb and the hypothalamus

(Herrmann et al., 2007). HCN4 seems to be more specific in expression, with significant expression in some thalamic nuclei and the mitral cells of the olfactory bulb (Herrmann et al., 2007). HCN4 was found to have strong expression in the AVCN and the MNTB, but weak staining in the LSO (Leao et al., 2005). Given that HCN1 has more depolarized voltage of activation, neurons with more HCN1 are likely to have more I_h open at the resting potentials than ones with dominant HCN2 and HCN4. Thus neurons with more HCN1 are likely to have a lower input resistance and hence a brief temporal window for synaptic integration, than if they expressed other HCN subunits.

Different subunit expression can in part explain different physiological properties observed in the different brain regions. A knockout of different HCN subunits with different patho-physiologies adds some credence to the idea of different roles for different subunits. HCN1 knockout impairs motor learning but improves spatial learning and memory (Nolan et al., 2003; Nolan et al., 2004). HCN2 knockout manifests in absence epilepsy, ataxia and sinus node dysfunction (Herrmann et al., 2007). HCN4 mice do not develop sinoatrial node-like action potentials and are embryonic lethal (Stieber et al., 2003; Stieber et al., 2006). Although knockout mice have been used to explore the function of different ion channels in the auditory system (Pyott et al., 2007), knockouts of different HCN subunits have yet to be employed for this purpose.

Structure and function of HCN channels

HCN channels belong to the large superfamily of pore-loop cation channels. Along with the cyclic nucleotide gated (CNG) and the Eag-like K^+ channels they belong to the subfamily of the cyclic-nucleotide-regulated cation channels. The architecture of HCN channels, like many other pore-loop channels, with a tetramer around a central pore, constitutes a functional channel. Each subunit has a trans-membrane core and a cytosolic c-terminus domain. HCN channels conduct sodium and potassium, with some recent evidence also pointing towards a limited calcium permeability (Yu et al., 2004; Yu et al., 2007; Michels et al., 2008). A potassium selectivity motif, glycine-tyrosine-glycine (GYG) in the pore region of potassium channels is supposed to be responsible for potassium permeability. HCN channels have the same selectivity motif and yet are permeable to sodium also. The permeability of the different cations through HCN channels, despite the potassium selectivity motif, currently remains a mystery. The c-terminal of all subunits contains the cyclic-nucleotide-binding domain (CNBD). Typically the voltage of half activation ($V_{1/2}$) varies across the subunits, with HCN1 > HCN3 > HCN4 > HCN2 being the order from the depolarized to the hyperpolarized $V_{1/2}$. The HCN single channel conductance is quite low (<1pS), making single channel recordings very difficult (DiFrancesco, 1986; Kole et al., 2006; Michels et al., 2005; Simeone et al., 2005).

The activation time courses of channels vary depending on the subunit and expression system, but the usual values for HCN1 are between 25 to 300 ms and for HCN4 between a few hundred milliseconds to a few seconds. Both HCN2 and 3 exhibit values intermediate to HCN1 and 4 (Wahl-Schott and Biel, 2009).

In some subunits, binding of cAMP modulates HCN channel properties drastically, like speeding the channel opening and shifting the voltage activation curve (*VAC*) to the depolarizing direction. For HCN2 and HCN4, cAMP causes a +10 to +25 mV shift in $V_{1/2}$ (Wahl-Schott and Biel, 2009). The crystal structure of CNBD has shed some important light in cAMP regulation of I_h (Zagotta et al., 2003). HCN1 and HCN3 show weak or no changes due to cAMP (Altomare et al., 2003). It is suggested that binding of cAMP increases channel activity by removing tonic channel inhibition conferred by CNBD (Wainger et al., 2001; Wang et al., 2001). Quite surprisingly, when CNBD of cAMP sensitive HCN4 is replaced by CNBD of cAMP insensitive HCN3, cAMP sensitivity is fully maintained. This suggests that in HCN3 the CNBD might be functionally silenced by changes in domains that communicate cAMP binding with the channel gating (Taraska, and Zagotta, 2007).

Co-assembly of different subunits (heteromultimerization) can result in increased variation in HCN physiology (Altomare et al., 2003; Much et al., 2003). Alternative splicing is reported in the invertebrate HCN channels (Gisselmann et al., 2005; Ouyang et al., 2007). Heteromultimerization, accessory subunits, translational,

post-translational and biochemical regulation of HCN are probably playing equally, if not more important roles in the observed differences in HCN properties in different the brain regions.

Regulation of HCN channels

Apart from cAMP, many proteins, metabolites, ions and accessory subunits can alter the properties of the HCN channels. Membrane phophoinositides, including phosophatidylinositol-4, 5-bisphosphate (PIP$_2$), act as allosteric ligands, shifting the *VAC* toward positive potentials, independent of the action of cyclic nucleotides (Zolles et al., 2006; Pian et al., 2006). HCN channels are sensitive to both intracellular and extracellular protons (implicated as one mechanism for sensation of sour taste (Zong et al., 2001; Munsch and Pape, 1999; Stevens et al., 2001). Both extracellular and intracellular chloride modulates HCN channels (Wahl-Schott et al., 2005). The extracellular effect of chloride seems to be pronounced for HCN2 and 4, while rather weak for HCN1 channels (Wahl-Schott et al., 2005). Intracellular chloride was recently shown to selectively occlude the instantaneous component of I_h (Mistrík et al., 2006), while having almost no effect on the longer lasting component.

It seems that phosphorylation modulates the properties of HCN channels. Non-receptor tyrosine kinase c-Src constitutively binds to HCN2 and is known to

enhance the activation kinetics of the channel (Zong et al., 2005; Li et al., 2008). Apart from c-Src, another kinase p38-MAP kinase (P38MAPK) is known to regulate I_h by shifting the voltage-dependent activation towards more positive potentials (Poolos et al., 2006).

In expression systems many membrane-bound, cytoplasmic, and cytoskeleton-related interacting proteins have been found to affect the properties of HCN channels. Roles of many accessory proteins in brain regions are as yet based on correlations. Nonetheless, the potential ability of these proteins to modulate the kinetics, the voltage dependence of activation, and the cAMP sensitivity of HCN channels could underlie differences in I_h properties in different neurons. Thus, neurons with faster I_h or more I_h available at resting potential need not necessarily have predominantly HCN1 subunit but underlying change in signaling altering the channel properties of potentially other HCN subunits.

The MinK-related protein MiRP1 (encoded by the gene KCNE2) is a member of a family of single transmembrane-spanning proteins and is an established auxiliary subunit of the HERG delayed rectifier K^+ channel (Abbott et al., 1999; Tinel et al., 2000; Zhang et al., 2001). MiRP1 increases current densities and accelerates activation kinetics of HCN2 (Yu et al., 2001; Qu et al., 2004). By contrast, MiRP1 does not affect the voltage-dependence of the HCN2 activation. In the HCN4, MiRP1 increases current densities, slows down kinetics and induces a negative shift in the activation curve of this channel (Decher et al., 2003). KCR1, which is

a protein like MiRP1, containing 12 putative transmembrane domains and known to interact with the HERG K$^+$ channel, is known to reduce HCN2 current densities and affect single channel characteristics (Michels et al., 2008).

HCN2 is known to interact with scaffold proteins Mint2 and S-SCAM (Kimura et al., 2004). Of all HCN subunits, only HCN2 selectively interacts with tamalin (Kimura et al., 2004). HCN1 is known to selectively interact with filamin A (Gravante et al., 2004). It is suspected that filamin causes clustering and slows down both the activation and deactivation kinetics of HCN1. Interaction of HCN channels with the lipid rafts, the caveolae and the effects of cholestrol depletion have been well documented in expression systems (Barbuti et al., 2004; Barbuti et al., 2007).

In recent years Trip8b (for tetratricopeptide-repeat containing Rab8b-interacting protein), also called Pex5R (for peroxisomal import 5-related protein), which specifically interacts with at least three of four HCN channel subtypes (HCN1, -2, and -4), has been the center of HCN regulation studies and some interesting controversies (Lipscombe and Pan, 2009). Although the details vary depending on specific experimental condition and the research group, it seems that different splice variants of Trip8b can have stimulatory or inhibitory effects on HCN channel activity and can account for hastening of HCN2 and cAMP insensitivity of HCN2 (Santoro et al., 2004; Lewis et al., 2009; Santoro et al., 2009; Zolles et al., 2009). Based on the properties of HCN channels in some fast auditory

neurons like octopus neurons, a previous explanation has been the predominance of HCN1 in fast auditory brainstem neurons (Bal and Oertel, 2000). Interaction with the accessory subunits and the scaffold proteins can be an underlying substrate for the different properties of HCN channels in different neurons, thus we need not necessarily expect HCN1 to be a major contributor to HCN channel properties observed in the fast auditory brainstem neurons, like the MSO.

Developmental changes in I_h

Age-related changes in the subunits have been observed in many different neurons, including both the up-regulation and down-regulation of g_h, positive or negative shifts in the *VAC* and changes in kinetics. In a few cases evidence of underlying subunit transition and changes in signaling has accumulated. However, barring few exceptions, our understanding of the functional consequences of the development related changes in the I_h properties are quite scanty. In the hippocampus, one group working on mice has reported a developmental doubling in the cAMP levels, yet a decline in cAMP sensitivity between PND 5 to PND 28, which they have attributed to decrease in cAMP-sensitive subunits (Surges et al. 2006). Looking at both RNA and protein level, the same group later found that in the hippocampus CA1 pyramidal neurons HCN1 increases with age with a reciprocal reduction of HCN4 and relative

stability of the HCN2 levels (Brewster et al., 2007). In *Cornu Ammonis* 3 (CA3) pyramidal neurons, HCN1 channels are present neonatally, while HCN2 increases with age (Brewster et al., 2007). Taking together the studies of Baram's group, the consistent trend is a decline in the HCN4 subunit in the hippocampus and the decline of cAMP-sensitivity of HCN channels in the mature neurons. In rat CA3 neurons g_h measured at -80 mV triples and quintuples in the CA1, which viewed along with an increase in membrane area corresponds to a maximum HCN density at PND5 (Vasilyev and Barish, 2002). During the same developmental time, activation times fell sevenfold in the CA3 and tenfold in the CA1 and of the dual activation they fitted to activation, the faster component increased in amplitude from 35 to 74% (at -90mV). This group found an increase in the total HCN1, 2 and 4 with age (Vasilyev and Barish, 2002). So, in this study a subunit transition for change in HCN properties was not a valid explanation. The discrepancies between the Barish and Baram's groups could be the result of use of different rodent species or using different antibodies. This is further complicated by the fact that specificity of almost all the available HCN antibodies is only marginally satisfactory. Interesting data from one peripheral neuron type suggests a developmental decline in the total g_h. In the intra-cardiac neurons the $V_{1/2}$ shifts depolarized by 10 mV and the kinetics hasten with age, despite the fact that current density (normalized for capacitance) becomes half that of the neonatal animals, showing independent modulation of total conductance and biochemical or subunit modulation associated with development (Hogg et al., 2001).

Organization of the dissertation

I am interested in understanding the active properties of MSO neurons that enable them to perform fine temporal processing. I have made I_h in MSO the focus of this research. This thesis focuses on understanding the voltage-dependent properties of the principal neurons of the MSO, especially the role of I_h and its interaction with I_{K-LVA} in regulating the properties of principal neurons of MSO. Given that we know that auditory system is undergoing drastic changes around hearing onset, I wondered if there are any changes in MSO during this period. Once we know what are the changes in the post-natal development of MSO, one can ask if sensory experience plays any role in shaping the changes or if the changes are developmentally predetermined. Thus apart from the interaction of I_h and I_{K-LVA}, I explored the development of MSO, with special emphasis on I_h.

Chapter 2 contains methods, which are common across all chapters. Chapter 3 describes the intrinsic properties of MSO neurons, developmental changes in the intrinsic properties around hearing onset and underlying changes in I_h. Chapter 4 explores the dynamic interaction of I_h with I_{K-LVA}. Chapter 4 is the first cellular physiology exploration of MSO neuron responses to trains of excitatory inputs. I conducted all the experimental work in chapter 4, but the computational modeling is a result of collaborative work with Drs. Michiel Remme and John Rinzel of New

York University and Dr. Nace Golding. Chapter 5 explores broad directions of MSO research, strengths and weaknesses of my research, and specific future directions arising out my work.

Chapter 2

MATERIALS AND METHODS

Because there is a significant overlap in the methods used in all of the experiments, the methods are compiled as a single chapter to avoid redundancy. The age ranges of the gerbils and small methodological details that are different are mentioned with the specific results.

Slice preparation

Mongolian gerbils (*Meriones unguiculatus*) were obtained from Charles River Laboratories (Wilmington, MA) or bred at the Animal Resource Center at the University of Texas at Austin. Gerbils were anesthetized with halothane and the brain removed while the head was submerged in warmed (32°C), oxygenated artificial cerebrospinal fluid (ACSF, in mM: 125 NaCl, 2.5 KCl, 2 CaCl$_2$, 20 NaHCO$_3$, 1.25 NaH$_2$PO$_4$, 25 glucose, 1.0 MgCl$_2$; pH 7.45 with NaOH). 200-μm thick horizontal sections were cut using an oscillating tissue slicer (VT-1000S and VT-1200S; Leica, Solms, Germany) and then transferred to an incubating chamber containing oxygenated ACSF at 35°C. Like most other brain slice preparations, MSO slices were incubated at 35°C for 30 minutes, to give

sufficient time for recovery of tissue from the slicing process. After 30 minutes of recovery time, slices were held at room temperature until recording. Individual slices were transferred to a recording stage, bathed with oxygenated ACSF and maintained at 35°C during recording. In ~>PND16 gerbils one obtains three, 200 µm slices containing MSO, while in younger animals one dissection usually yields two slices. Given that most experiments involve pharmacological manipulations with the control and the drug case, only one cell from each slice was obtained. 100% of the cells recorded in healthy state within defined standards of series resistance (detailed in whole-cell voltage/current/dynamic-clamp recording sections below) were included in the analysis. Thus one dissection can maximally provide three MSO recordings, although three is the maximal limit, with other experimental constraints governing the yield.

Whole-cell voltage-clamp recording

MSO neurons were visualized using infrared differential interference contrast microscopy (Axioskop 2FS Plus; Zeiss, Oberkochen, Germany) in combination with a Newvicon tube camera (Dage-MTI, Michigan City, IN). Borosilicate patch micromicromicropipettes (1.65 mm outer diameter; World Precision Instruments, Sarasota, FL) were heat polished and had open tip resistances of 2-4 MΩ when filled with a potassium-based internal solution.

For I_h measurements, the micropipette solution contained (in mM): 127 potassium gluconate, 8 KCl, 10 sodium phosphocreatine, 10 HEPES, 0.5 EGTA, 4 MgATP, 0.3 NaGTP, pH 7.3, with KOH. I_h was isolated pharmacologically by including the following in the normal ACSF (in mM): 1 3,4-Diaminopyridine, 0.2 4AP, 10 TEA-Cl, 0.2 $BaCl_2$, 0.001 TTX-citrate, 0.05 $NiCl_2$, and 0.2 $CoCl_2$. These drugs block voltage-gated and inwardly rectifying potassium currents as well as voltage-gated sodium and calcium currents. In addition, 10 µM CNQX, 50 µM AP-5, and 2 µM strychnine were included in the ACSF to block AMPA, NMDA and glycine receptors. In experiments involving pharmacological block of I_h ZD7288 (50 µM) was added to the bath to block I_h. TTX-citrate was obtained from Tocris Cookson (Ellisville, MO). 3,4-Diaminopyridine, 4AP, TEA-Cl, $BaCl_2$, $NiCl_2$, and $CoCl_2$ were obtained from Sigma (St. Louis, MO). All synaptic blockers were obtained from Tocris Cookson, except for strychnine, which was obtained from Sigma.

Data were recorded with an Axopatch 200B (Molecular Devices, Sunnyvale, CA), filtered at 1 kHz, digitized at 50 kHz and acquired using custom macros programmed in IgorPro (WaveMetrics, Lake Oswego, OR). Stray electrode capacitance was reduced by wrapping electrodes with parafilm (Pechiney Plastic Packaging, Chicago, IL) and remaining capacitance was further reduced using the electrode-capacitance-compensation circuitry of the amplifier. Series resistance and whole-cell capacitance was compensated between 85 to 95%. All

recordings were performed at 35°C. All voltages reported are corrected for a liquid junction potential of 9 mV.

To study the signaling pathways that regulate *VAC* of HCN channels, agonists and antagonists of various signaling pathway were applied to the MSO neurons. To ensure that effective concentration of the drug was bathing MSO neurons, after control recordings, ACSF with the drug was washed in the recording chamber for at least 10 minutes. In cases of pre-incubation with drug, the pharmacological agent was diluted in the incubating chamber and in the recording ACSF. All pre-incubations were at least 30 minutes. 10 μM of wortmannin, a PIP_2 antagonist was used to study the PIP_2 signaling. 10 μM of SB203580 and 30 μM of SB202190, both P38MAPK antagonists were employed to study the effects of P38MAPK on HCN channels. 20 μM of forskolin: a cAMP enhancer, 20 μM of Rp-cAMPs and Sp-cAMPs: both modulators of the indirect effects of cAMP through cAMP dependent protein kinases, 1 mM of 8-Bromo-cyclic AMP: a non-hydrolysable analog of cAMP, 1 mM of dibutyryl-cAMP: a membrane permeable analog of cAMP, were employed to study modulation of HCN channels in response to cAMP. In cases, were modulators were applied intracellularly recording were only conducted after 5 minutes of breaking in to ensure that intracellular drug had reached equilibrium levels in the neurons.

To study the development of I_h deactivation during excitatory-post-synaptic potentials (EPSPs) in voltage-clamp, an EPSP-shaped waveform was scaled to

33

different peak voltages and concatenated with itself multiple times to form a 1 s long stimulus train of 500 Hz. The changes in I_h deactivation as a result of the EPSP train were measured by stepping the membrane potential at the end of the train to –100 mV (tail-current analysis). The non-I_h leak and capacitative current were measured in the presence of 50 µM ZD7288 in the same experiment.

The same stimulus used to study I_h deactivation was used to test the $I_{K\text{-}LVA}$ inactivation. As $I_{K\text{-}LVA}$ kinetics is much faster than I_h kinetics, no tail current analysis was performed at the end of the stimulus. To isolate $I_{K\text{-}LVA}$, the following were added to ACSF (in mM): 0.05 ZD7288, 1 TEA, 0.2 $BaCl_2$, 0.001 TTX, 0.05 $NiCl_2$, 0.2 $CoCl_2$, 0.01 CNQX, 0.05 AP-5, and 0.002 Strychnine.

Activation of the synaptic inputs to the MSO neurons was achieved by delivering brief (100-µs) electrical pulses medial to the MSO through glass micromicromicropipettes with tip diameters of 10 to 15 µm. A bipolar stimulating electrode was used to stimulate wide areas of contralateral excitatory projections to the MSO. This was achieved by placing two glass micropipettes with separation of 2 to 6 mm. Pulses were generated by a constant current stimulator (Digitimer, Welwyn Garden City, UK).

Whole-cell current-clamp recordings

Whole-cell patch-clamp recordings were made from visually identified MSO principal neurons prepared as outlined above. The same potassium gluconate-based internal solution was used as in the voltage-clamp recordings, and micromicropipettes had an open tip resistances of 2-5 MΩ when filled with this potassium-based internal solution. Recordings were included if the series resistance was <15 MΩ and the resting potential was negative to –55 mV (after the junction potential correction of 9 mV). Data were low-pass filtered at 5 kHz and acquired to a computer at 50 kHz. All recordings were corrected for a liquid junction potential of 9 mV.

Simulated excitatory post synaptic currents (EPSC) waveforms were generated using a biexponential function of the form: $f(t)=A*(-exp(-t/\tau_1) + exp(-t/\tau_2))$, where A is the current amplitude and τ_1 and τ_2 are the time constants of the PSC rise and decay, respectively. For EPSCs, τ_1 and τ_2 were 0.2 and 0.201 ms. Stimulus-induced changes in input resistance were calculated using brief hyperpolarizing pulses (3-5 mV, 10 ms duration) before and after the stimulus (50 and 10 ms, respectively).

To study if the changes in MSO excitability are sensitive to fine stimulus statistics or just integrate the overall depolarization, in a subset of experiments the regularity of the brief depolarizing current pulses (0.5 ms) in a stimulus train was

varied while the mean stimulus frequency was held constant at 350 Hz (1s overall train duration). The interstimulus interval was generated with a Gaussian noise function, with upper and lower bounds imposed (15 and 0.2 ms, respectively). Regularity was expressed as the standard deviation of the interstimulus interval. Ten random stimuli were generated and tested exhibiting 4 different degrees of regularity, with standard deviations (SDs) of 0.5, 1.0, 1.5, and 2.0 ms), as well as a single train exhibiting perfect regularity (SD = 0 ms).

To study the coincidence window of MSO neurons, inhibitory glycinergic synaptic inputs were blocked by 2µM strychnine. Bilateral excitatory synaptic inputs were activated by 100-µs electrical pulses. Pulses were delivered via ACSF-filled glass electrodes, each with one wire in the electrode and another wrapped around it. Two glass electrodes were placed medially and laterally of the MSO in a 200 µm thick horizontal slice. The amplitudes of stimulation were modified to obtain similar somatic EPSP amplitude from each side so that when delivered together with perfect coincidence, the EPSP amplitude was just sufficient for initiation of an AP.

Dynamic-clamp recording

Dynamic clamp was implemented during current-clamp recordings using commercial software (SM-2 software, Cambridge Conductance, Cambridge, UK)

in conjunction with a Toro-8 analog DSP board running at 40 kHz. To assess the influence of I_h on the dynamic range of MSO principal neuron output, we injected trains of simulated EPSCs (to evoke EPSP trains), whose amplitudes were adjusted to match five different patterns of synaptically evoked EPSCs recorded in a representative voltage-clamp experiment (1 s, 500 Hz). This procedure allowed the pattern of synchronous synaptic currents to be mimicked in the absence of stimulation artifacts. Injected simulated EPSC trains were scaled relative to the first EPSC in the train, which was adjusted between 1500 to 5000 pA in 500 pA increments. Following control responses, I_h was blocked with 50 µM ZD7288 and the dynamic clamp was used to introduce a static leak exhibiting a reversal potential of -40 mV ("static g_h", or $g_{h(S)}$). The magnitude of $g_{h(S)}$ was adjusted until the membrane time constant, resting potential, input resistance and EPSP matched control values. The conductance injection varied from 12 to 39 nS. Series resistance and capacitance compensation were employed, and recordings were discontinued if the series resistance exceeded 10 MΩ.

Data Analyses

All analyses were performed using IgorPro. In current-clamp experiments, peak and steady-state V–I plots were generated from peak and steady state voltage responses to 100 ms current steps. The input resistance was obtained from the slope of the peak V–I plot between 0 and 10 mV below rest. The membrane time

constant was obtained from a single exponential fit from baseline to the peak of a hyperpolarizing voltage response (3–5 mV from rest). Relative changes in the input resistance (R_N) during trains of synaptic-like depolarizations were quantified as $[(R_{N(posttrain)} - R_{N(pretrain)}) / R_{N(pretrain)}] * 100$.

In voltage-clamp experiments, the voltage-dependence of I_h activation was measured from peak tail currents (after the end of capacitative transient) arising from a step to –100 mV following 1-s prepulses to voltages between -30 mV and -110 mV in 10-mV increments. These currents were normalized to maximum and minimum values. The normalized G-V curve was fit with a Boltzmann equation of the form: $f(V) = 1/(1+exp[(V_{1/2}-V)/k])$, where V is the membrane voltage, $V_{1/2}$ is the half-maximal activation voltage, and k is the slope factor. To measure the reversal potential, I_h was activated with a 1-s pulse to -100 mV, followed by steps between –100 and –60 mV and the linear fit to points extrapolated to zero current value. Instantaneous tail currents were plotted vs. membrane potential, and the reversal potential was calculated from the zero crossing of the linear fit. For group comparisons, means are presented ± SEM and statistical significance was assessed using either a two-way ANOVA or Student's t test at a significance level of 0.05.

Computational modeling

A single compartment model was constructed. The model includes three central

sub-threshold membrane currents: the voltage-dependent K-LVA-type and h-type currents, and a leak current. The current balance equation takes the form

$$C_m \frac{dV}{dt} = -g_L(V - E_L) - \overline{g}_{K-LVA}w^4 z(V - E_K) - \overline{g}_h(k_r r_f + (1 - k_r)r_s)(V - E_h) + I(t)$$

with whole-cell capacitance C_m = 25 pF, peak conductances g_L = 15 nS, $\overline{g}_{K-LVA}$ = 190 nS and $\overline{g}_h$ = 70 nS, and reversal potentials E_L = −77.5 mV, E_K = 106 mV and E_h = −37 mV. The cell had a resting membrane potential V_{rest} = −58 mV. Parameters and current descriptions were based on whole-cell measurements from MSO cells. The current model for I_{K-LVA} was taken from Mathews et al. (personal communication). The I_h model was based on our experimental data and fitted using Neurofit (Willms, 2002). The kinetics are described by the sum of a fast (r_f) and a slow (r_s) gating variable with the fast component accounting for a fraction k_r = 0.65 of the total I_h. Unknown parameters ($\overline{g}_{K-LVA}$, g_L, E_L) were set such that we could account for experimental measurements of the input resistance R_N, membrane time constant τ_m, and the resting membrane potential V_{rest}. Excitatory synaptic input $I(t)$ was modeled as a current injection with the time course described by an alpha function with a time constant of 0.6 ms.

The voltage V_{aft} (t) after the input $I(t)$ ends at time t can be obtained by solving the implicit equation

$$g_L(V_{aft} - E_L) + \overline{g}_{K-LVA}w_\infty^4(V_{aft})z(t)(V_{aft} - E_K) + \overline{g}_h r(t)(V_{aft} - E_h) = 0$$

with $r(t) = k_r\, r_f(t) + (1 - k_r)\, r_s(t)$. Note that we take into account that the time constant of $I_{\text{K-LVA}}$ activation is fast ($\sim$ 1 ms) and quickly reaches steady state values, $w_\infty(V_{\text{aft}})$. To compute the input resistance $R_N(t)$ we first linearized the current balance equation around the voltage V_{aft}. Inactivation of $I_{\text{K-LVA}}$ and (de)activation of I_h is much slower than $I_{\text{K-LVA}}$ activation such that $R_N(t)$ for a 10-ms current pulse can be computed as

$$R_N(t, V_{aft}) = \frac{1}{g_L + \overline{g}_{K\text{-}LVA\text{-}eff}(t, V_{aft}) + g_h(t)}$$

where

$$g_h(t) = \overline{g}_h r(t)$$

and

$$g_{K\text{-}LVA\text{-}eff}(t, V_{aft}) = \overline{g}_{K\text{-}LVA} w_\infty^4(V_{aft}) z(t) + g_w(t, V_{aft}) = 0$$

with

$$g_w(t, V_{aft}) = 4\overline{g}_{K\text{-}LVA} w_\infty^3(V_{aft}) z(t)(V_{aft} - E_K) w_\infty'(V_{aft})$$

where $w_\infty'(V_{aft})$ is the derivative of the $I_{\text{K-LVA}}$ activation function with respect to V evaluated at V_{aft}. If the system reaches its steady state with a mean voltage V_{mean}, we can set the gating variables to their respective steady state values $z(t) = z_\infty(V_{mean})$ and $r(t) = r_\infty(V_{mean})$.

Chapter 3

Developmental changes in the I_h of MSO

ABSTRACT

Principal neurons of the mature medial superior olive (MSO) are known for a phasic, temporally precise and brief response to binaural inputs; however, we observed that immature MSO neurons have slow membrane time constants and even exhibit burst spiking to unilateral excitatory inputs. We found that the maturation of a hyperpolarization activated cyclic nucleotide gated current called I_h is one of the important underlying changes responsible for the maturation of MSO properties. We observed that in the post-natal development around hearing onset I_h kinetics hasten, the total conductance increases ten fold and quite surprisingly, the *VAC* shifts in the depolarized direction by 30 mV. Along with an increase in the conductance of low voltage activated potassium channels (I_{K-LVA}) after hearing onset (Scott et al., 2005), a combination of increased g_h and shifted *VAC*, makes 100 fold more I_h available at the resting potential. Using bilateral synaptic stimulation of varying inter-stimulus intervals, we assessed the coincidence window of MSO neurons and found that blocking I_h in the adult gerbils results in a 3-fold increase in the synaptic-coincidence window. In adult MSO neurons we found that the *VAC* of I_h is sensitive to P38MAP kinase and

PIP$_2$ signaling. A modulation in the *VAC* of I_h by P38MAPK resulted in a significant shift in the synaptic-coincidence window, suggesting that the properties of I_h are an important underlying substrate for plasticity of the adult MSO properties. To study the underlying mechanisms in changes of the *VAC* of I_h, we used cAMP analogs at different stages of development, because different HCN subunits have varying sensitivity to cAMP. We found that cAMP sensitivity declined steadily with development, suggesting an underlying change from HCN2 to HCN1. However, an alternative explanation of the expression of accessory subunits and post-translational mechanisms, which can alter cAMP sensitivity and kinetics of I_h (Zolles et al., 2009) cannot be ruled out. Thus we find that after hearing onset massive changes occur in the total g_h and the *VAC*, which are accompanied by reduced sensitivity to cAMP, and are responsible for significant brevity of MSO neuron responses.

INTRODUCTION

In gerbils there are two sources of postnatal changes in the auditory experience: hearing onset (~P12 to P13) and an increase in the head size of animals with age. Many changes in the conduction velocity (Moore et al., 1996), synaptic transmission (Caicedo and Eybalin, 1999; Kullmann and Kandler, 2001; Magnusson et al., 2005), projection and spatial distribution of both the inhibitory and excitatory synaptic contacts (Kitzes et al., 1995; Sanes and Takács, 1993;

Werthat et al., 2008) dendritic complexity (Chirila et al., 2007; Rautenberg et al., 2009) and even the axonal projections of MSO (Okoyama et al., 1995)   are observed during this time period.   Altering binaural auditory experience, by means of unilateral cochlear ablation (Russell and Moore, 1999) or ominidirectional sound (Seidl and Grothe, 2005) effects the unilateral dendritic morphology and MSO output respectively, suggesting an important role of sensory experience in the postnatal auditory experience.

Our current understanding of development of active properties of MSO is confined to an increase in the conductance of low voltage activated potassium channels, G_{K-LVA} in the week after hearing onset (Scott et al., 2005). Because data presented in this thesis implicates I_h to be one of the major determinants of MSO properties, developmental changes in HCN properties of MSO neurons and functional consequences of changes in I_h were explored in this chapter.

In expression systems, different HCN subunits have varying cAMP sensitivity, with HCN1 and 3 being almost insensitive to cAMP, while HCN2 and 4 exhibit between +10 to +25 mV shift in *VAC* in response to saturating levels of cAMP (Altomare et al., 2003). In expression systems, the voltage of half activation ($V_{1/2}$) varies from subunits, with the $V_{1/2}$ from the depolarized end to the hyperpolarized end in the following order HCN1>HCN3>HCN4>HCN2. HCN1 has fastest kinetics while HCN4 is the slowest with the kinetics of HCN2 and 3 being intermediate between HCN1 and 4. Developmental changes in I_h kinetics, cAMP

sensitivity, and $V_{1/2}$ have frequently been interpreted as being due to the changes in subunit composition; nonetheless there has been no single study which clearly establishes a causal relation in the change of subunits and cAMP insensitivity. In the mouse hippocampus, cAMP levels increase with age, yet cAMP sensitivity declines with age (Surges et al., 2006). In CA1 pyramidal neurons, HCN1 increases with age, with reciprocal reduction of HCN4 and relatively stable HCN2 levels, while in the CA3 pyramidal neurons HCN1 channels are present neonatally, while HCN2 increases with age (Brewster et al., 2007). During the same period in rat hippocampus, the kinetics of I_h hasten, suggesting HCN1-like response but molecular data show an increase in all the HCN1, 2 and 4 with age (Vasilyev and Barish, 2002).

Alternative mechanisms of HCN modulation, apart from subunit transition are not unheard of, like hetero-multi-merization, which can result in increased variation of HCN physiology (Much et al., 2003). Alternative splicing is reported in the invertebrate HCN channels (Gisselmann et al., 2005; Ouyang et al., 2007). HCN channels are modulated by various intracellular signaling pathways, like PIP_2 (Zolles et al., 2006; Pian et al., 2006), P38MAPK (Poolos et al., 2006), c-Src (Zong et al., 2005; Li et al., 2008), cytoskeletal elements (Kimura et al., 2004; Gravante et al., 2004), pH (Stevens et al., 2001); association with rafts (Barbuti et al., 2004), and chloride levels (Mistrík et al., 2006). In recent years many auxillary subunits that can modify HCN properties have been isolated, including

44

MiRP1 (Qu et al., 2004), KCR1 (Michels et al., 2008) and Trip8b (Lipscombe and Pan, 2009).

In the lateral superior olive (LSO), an adjacent nucleus to MSO, sensory deprivation by means of a contralateral cochlear ablation causes a transient increase in the g_h (Hassfurth et al., 2009). Increase in the g_h seemed short lived (Hassfurth et al., 2009). This study is further complicated due the effects of injury. Thus the role of I_h and it's developmental changes in MSO and auditory brainstem in general, are an unexplored question.

RESULTS

MSO neurons become temporally precise in a week after hearing onset

After hearing onset I_{K-LVA} increases (Scott et al., 2005) and MSO neuron input resistance also decreases (Scott et al., 2005; Chirila et al., 2007). Using whole–cell current–clamp recordings from the somata, we observed many developmental changes in the MSO neurons of different ages (Figure 1.1). One of the striking and novel features that we observed was the repetitive firing (burst–firing) of MSO neurons to square current injections and order–of–magnitude slower synaptic responses than the older neurons (data not presented). These spikes were found to have an underlying sodium and calcium electrogenesis. Burst–firing quickly disappeared around the hearing onset (Figure 1.1C). Another researcher in laboratory is now following my initial studies

on the burst–firing properties and exploring the role of NMDA receptors in slow synaptic responses observed during these ages.

We obtained voltage–current relationships using somatic current steps and calculated input resistance using the slope of the V-I function (Figure 1.1A). After hearing onset, we observed a decline in the input resistance of MSO neurons (Figure 1.1B) consistent with a previous study (Chirila et al., 2007). An order–of–magnitude difference in the membrane time constants was also observed (Figure 1.1A).

Given the important role of I_h in many auditory brainstem neurons (Oertel, 1999), we looked to see if there is evidence of change in I_h over this developmental time period. We observed that blocking I_h using 50 µM ZD7288 caused an increase in the input resistance at all ages (Figure 1.1B), suggesting an important role of I_h. Another curious observation was a depolarizing shift observed in the resting membrane potential of MSO neurons over the developmental period (Figure 1.1D) and a depolarizing shift in the potential where depolarizing sag (threshold for sag = 2mV) in hyperpolarizing voltage responses is obvious (Figure 1.1E). Because I_h is a depolarizing conductance and is considered to be responsible for voltage sag, we expect an increase in the level of I_h with age. Nonetheless, to explore developmental I_h changes quantitatively current–clamp observations are not sufficient, thus we used the whole–cell voltage–clamp recordings to explore this issue.
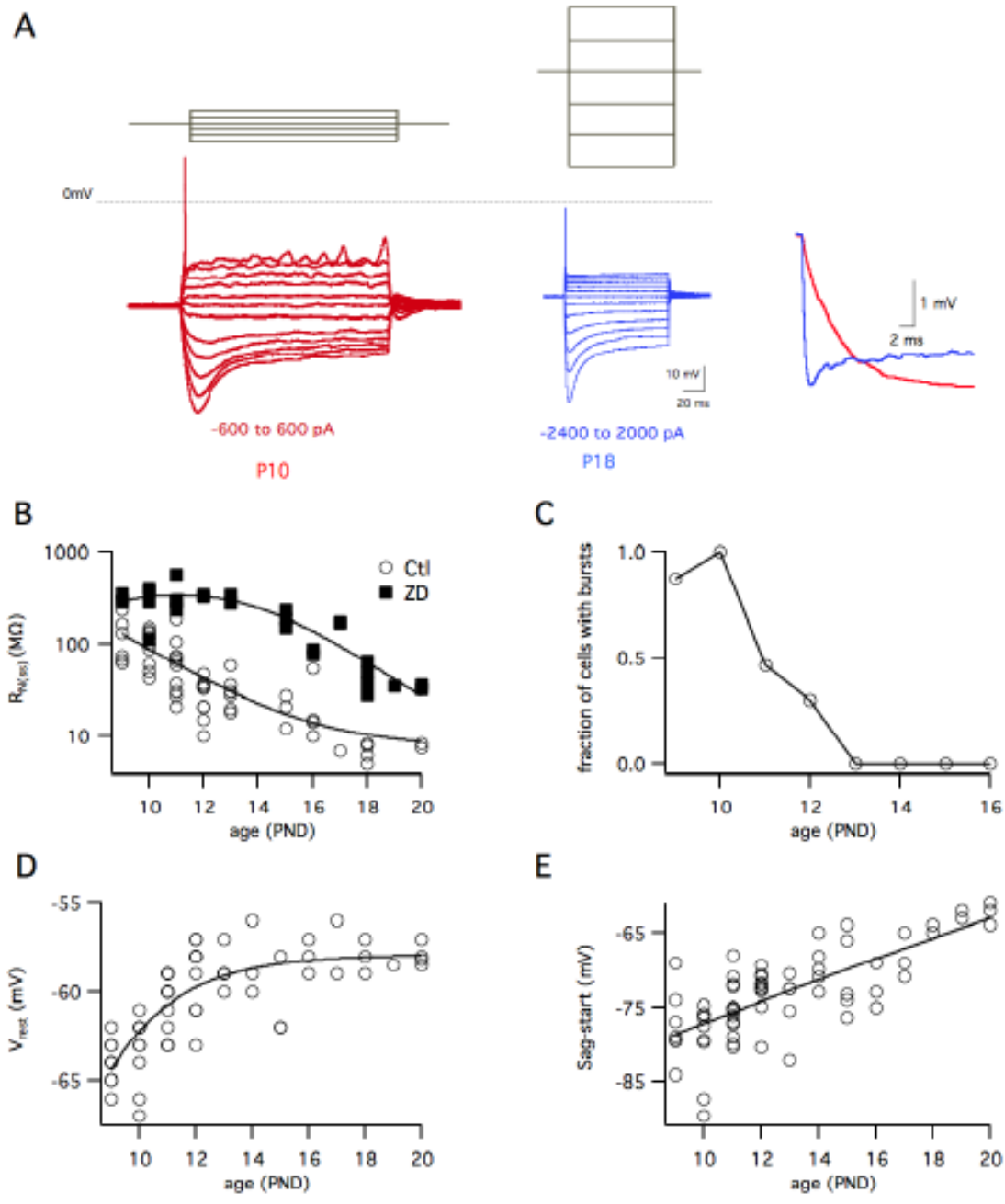
Figure 1.1 MSO properties undergo rapid maturation after hearing onset. A. Top is the schematic of current injection. In red is the response of a representative PND 10 MSO neuron and in blue is the response from a PND 18 MSO neuron. For PND 10 the square current injection was from -600 to +600 pA, while for PND 18 from -2.4 to +2 nA. On the right hand side, brief hyperpolarizing response to a small negative current injection from two ages are overlaid, illustrating the order of magnitude difference in membrane time constants across the two ages. B. Steady state input resistance shows a drastic reduction over few days of MSO development. Open circles are measurements from control (Ctl) condition and closed squares are measurements from 50 μM ZD7288 (ZD) condition. Each point is the measurement from one cell. $R_{N(ss)}$ was calculated as the slope of the fit of the hyperpolarizing part of steady state VI plot. C. Fraction of cells as a function of age exhibiting burst–spiking in response to square depolarizing pulse (n≥24 cells). D. Resting potential shows small depolarization (~ 5 mV) as a function of age. Each datum point is the

measurement from one cell. E. The membrane potential at which sag started (labeled as sag start) appearing in response to square current injection underwent a depolarizing shift with development. Each datum point is the measurement from one cell.

Developmental changes in conductance, kinetics and *VAC* of I_h

To obtain conductance estimates, using whole–cell–voltage clamp recordings, MSO neurons were stepped from -30 mV to hyperpolarizing potentials and then to obtain tail currents we stepped the membrane to -110 mV. Different maximal currents were activated at different ages (Figure 1.2A, 1.2C), indicating an increase in the total conductance during development. On average a nine-fold increase in the total conductance was observed. Apart from the increases in conductance, hastening of kinetics of I_h activation was also observed during development. A five-fold decrease in the fast time constant and a four-fold decrease in the slow time constant of activation were observed over the developmental time period. Given that MSO neurons decrease in dendritic complexity and increase in axial diameter during development (Rautenberg et al., 2009), the space clamp problems should be more acute in the younger ages. Thus, if the somato-dendritic spatial distribution of HCN channels is similar across ages, then our measurements of the differences in kinetics across MSO development are a conservative estimate and cannot be explained by space clamp problems.

When the responses to hyperpolarizing steps were observed, the *VAC* obtained by tail current analysis (see methods) was found to be progressively shifted in

the depolarized direction with age (Figure 1.2B, 1.2D), thus making in effect almost no I_h available at resting potential in young animals, and more than 100 fold more of it available in one week after the hearing onset.
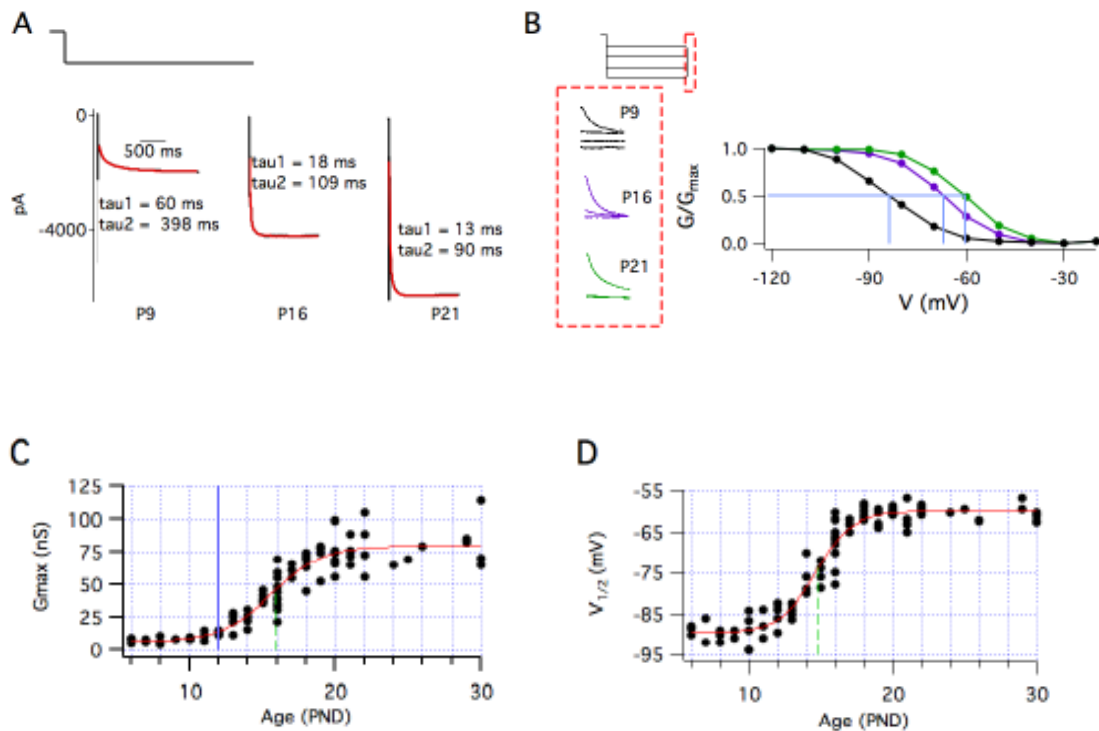
Figure 1.2 Development of I_h properties. A. The kinetics of I_h become faster and the total conductance in MSO neurons increases with postnatal development. In response to a hyperpolarizing pulse to -100mV from a holding potential of –30 mV, the pharmacologically isolated I_h exhibits significant currents in old age. B. The $V_{1/2}$ of I_h also shifts in the depolarizing direction with age. In response to a family of hyperpolarizing pulses, the tail currents show saturation at more depolarized potentials in older animals. The normalized conductance (G/G_{max}) plot shows a successive depolarized shift with the age of animals. PND12 is the day of hearing onset. C. Shows group data for maximal g_h. D. The $V_{1/2}$ exhibited a 30 mV depolarization shift during the postnatal development. Each point in C. and D. represents the value obtained from one cell, while A and B are representative experiments.

cAMP sensitivity of I_h

One interpretation from the hastening of kinetics and depolarizing shift in the $V_{1/2}$, is that there are developmental change in HCN subunits. Given that HCN1 subunits are less sensitive to cAMP than other HCN subunits (Altomare et al., 2003; Wahl-Schott and Biel, 2009) it is likely that cAMP sensitivity of adult MSO neurons declines compared to young MSO neurons. Forskolin is known to increase internal concentrations of cAMP, while Rp-cAMPs and Sp-cAMPs modulate the indirect effects of cAMP through cAMP dependent protein kinases. 8-Bromo-cyclic AMP is a non-hydrolysable analog of cAMP, while dibutyryl-cAMP is a membrane-permeable analog of cAMP. In adult MSO 20 μM forskolin was not found to have any effect on the *VAC* of PND 18 MSO (Figure 1.3A, 1.3E). Similarly 20 μM of Rp-cAMPs (Figure 1.3B, 1.3E) and 1 mM of 8Bromo-cAMP (Figure 1.3C, 1.3E) had no effect on the adult MSO. The MNTB, which is an adjoining nucleus of MSO, is known to express HCN channels sensitive to cAMP (Banks et. al. 1993). Mature MNTB was used as a control to ensure that our preparation was working (Figure 1.3D, 1.3F). After hearing onset I_h in MSO neurons exhibited strong sensitivity to cAMP signaling, as obvious from Figure 1.3F, where by PND10, *VAC* underwent a depolarizing shift in response to 1 mM of dibutyryl-cAMP (Figure 1.3F). MSO neurons show similar shifts in the $V_{1/2}$ for both dibutyryl-cAMP and forskolin (Figure 1.3 F, 1.3G). Thus HCN in MSO exhibits cAMP sensitivity at young ages but within a week after hearing onset it is completely lost. This is congruent with the limited immunocytochemistry data that suggests HCN1 dominating HCN channels in the adult MSO (Koch et. al., 2004).

Nonetheless, these experiments do not rule out changes in biochemical signaling, association with auxiliary subunits and many other post-translational mechanisms, which may be responsible for the reduced cAMP sensitivity (see discussion section of this chapter for details)
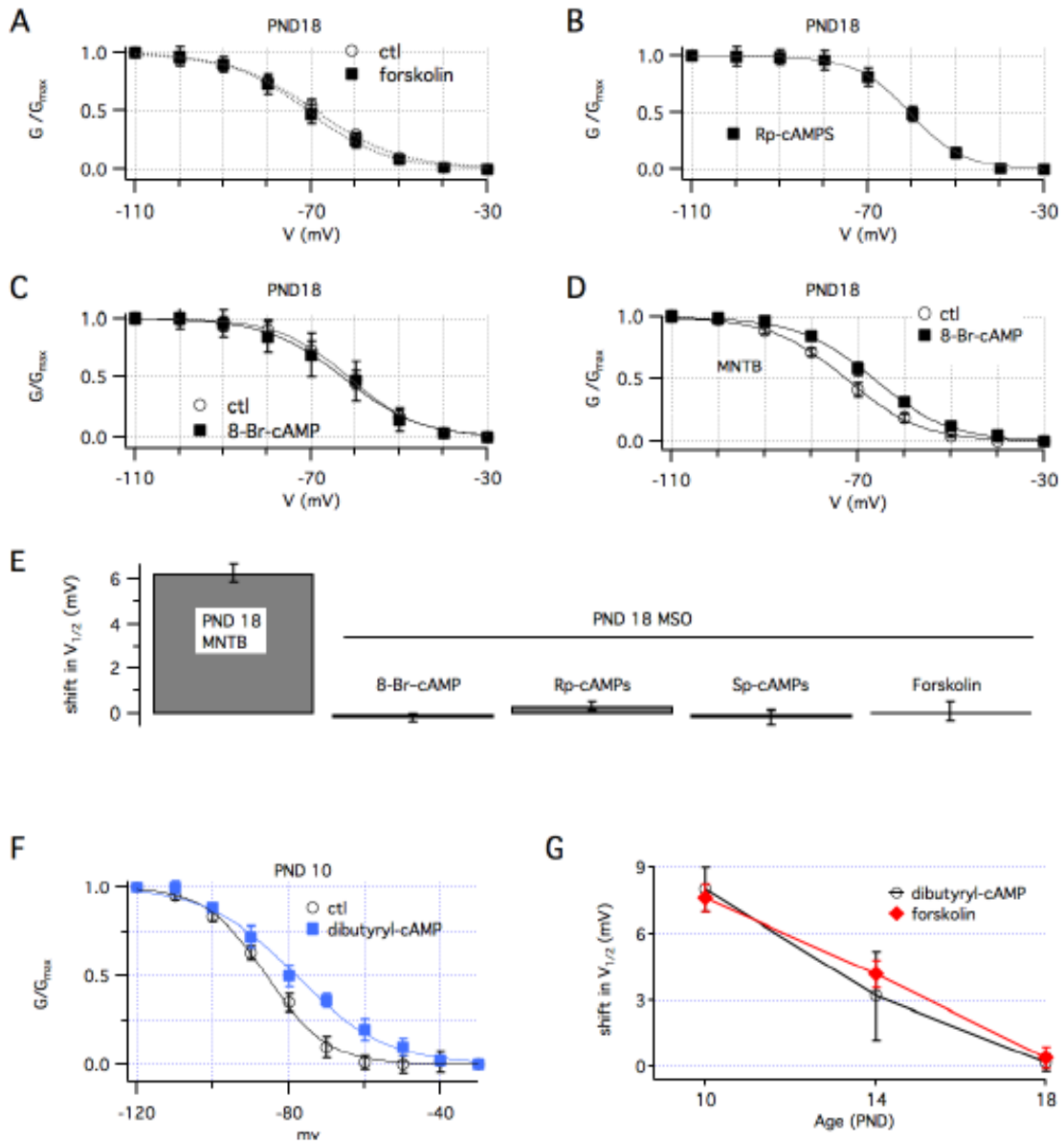

Figure 1.3 Cyclic AMP signaling is effective in the I_h of the young MSO. A through C. I_h in MSO of PND 18 animals does not show sensitivity to cAMP analogs/cAMP level enhancers (n= 7 cells for each drug). D. Neurons of the medial nucleus of the trapezoid body (MNTB), exhibit a significant

depolarizing shift in presence of 8 Bromo-cyclic-AMP (n= 6 cells). E Group data of $V_{1/2}$ shift due to cyclic AMP signaling in PND 18 animals shows that after one week of hearing onset there is no cAMP sensitivity in HCN channels. F. In pre-hearing animals I_h exhibits cAMP sensitivity, as shown by a shift in the *VAC* of a PND10 MSO (n = 6 cells). G. cAMP sensitivity of I_h decreases with age, as evident from group data on the shift in the $V_{1/2}$ (n ≥ 6 cells for each age range).

Sensitivity of to I_h other signaling pathways

Both PIP$_2$ and P38MAPK signaling are known to modulate the HCN properties irrespective of subunit composition of HCN channels. Given the unusually depolarized $V_{1/2}$ of I_h in MSO, I wondered, apart from the putative subunit of HCN1 in adult MSO, if some of the known modulators could be behind the properties of I_h in the adult MSO neurons. 10 µM of wortmannin, a PIP$_2$ antagonist, shifted the $V_{1/2}$ of I_h in MSO (Figure 1.4) by ~9mV. Two P38MAPK antagonists (10 µM) SB203580 and (30 µM) SB202190, both shifted $V_{1/2}$ of I_h by ~10mV (Figure 1.5). Taking together the cAMP, PIP$_2$ and P38MAPK data, both a potential subunit change and intracellular signaling are likely to be responsible for unusually depolarized *VAC* of the I_h in the MSO neurons.
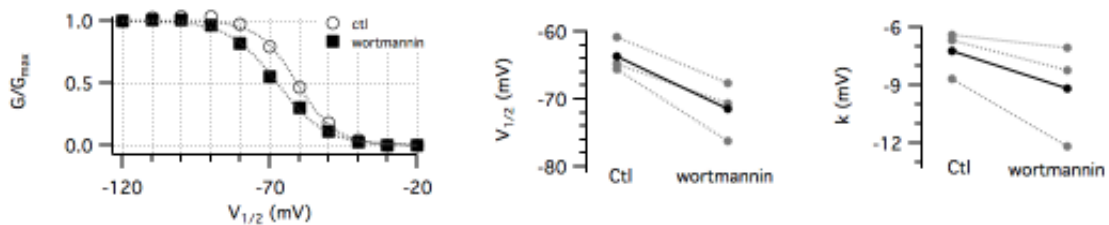

Figure 1.4 PIP$_2$ signaling modulates I_h in mature MSO neurons. On the left side is a representative experiment with Ctl and 10 µM Wortmannin conditions. 10 µM Wortmannin, an antagonist of PIP$_2$ resulted in a ~9mV shift in the *VAC*, as measured by the difference in $V_{1/2}$ (p< 0.5). PIP$_2$ signaling also modulates the slope of *VAC* (k) (p< 0.5).

52

Functional significance of I_h properties

From the decreased input resistance and increased g_h with age, an important role of I_h in setting the MSO input resistance and hence time constants is not entirely unexpected. Because MSO neurons analyze coincidence of binaural excitatory inputs, I asked what is the impact of removing or modulating I_h on the synaptic coincidence window of the MSO. Bilateral excitatory inputs (corresponding to binaural excitatory inputs, coming via AVCN) were stimulated to evoke near equal synaptic responses from both the sides to amplitudes such that at zero inter-pulse-interval (IPI), i.e. at perfect coincidence, the EPSPs just barely resulted in spikes each time (probability of action potential = 1). For each IPI 10 to 20 repetitions were conducted to obtain probability of spiking. In a representative experiment in Figure 1.6B, one can see five repetitions of 0, 200, and 400 µs IPI. In control (Ctl), the probability of firing action potentials declines more rapidly than when I_h is blocked by 50µM ZD7288 and the cell is brought back to the same resting potential as the control case by means of a constant–current injection in the somata (Figure 1.6B, 1.6C). Using P38MAK antagonist, which we know hyperpolarizes the *VAC* of the I_h in the MSO (Figure 5), I asked if by modulating HCN channels instead of blocking I_h, can one change the synaptic coincidence window. By blocking P38MAPK signaling, the MSO neurons hyperpolarized due to shift in *VAC* of I_h (Figure 6.1A). Thus even after the injection of artificial current to bring the cells to control potentials, less I_h was available at the resting potential. Even when the cell was brought back to control resting potential by artificial current injection, the depolarizing sag on

hyperpolarization was much reduced in the case of 20 µM of SB203580 (Figure

1.6A). In case of SB203580, with cell being at same resting potential as control,

the synaptic coincidence window almost doubled (Figure 1.6C). Addition of 50

µM ZD7288 on top of P38MAPK only slightly increased the synaptic coincidence

window, thus emphasizing that not just I_h but its unique properties in the MSO

are a key to determining the synaptic integration properties in MSO and thus are

important in regulating the encoding of inter-aural time disparity.
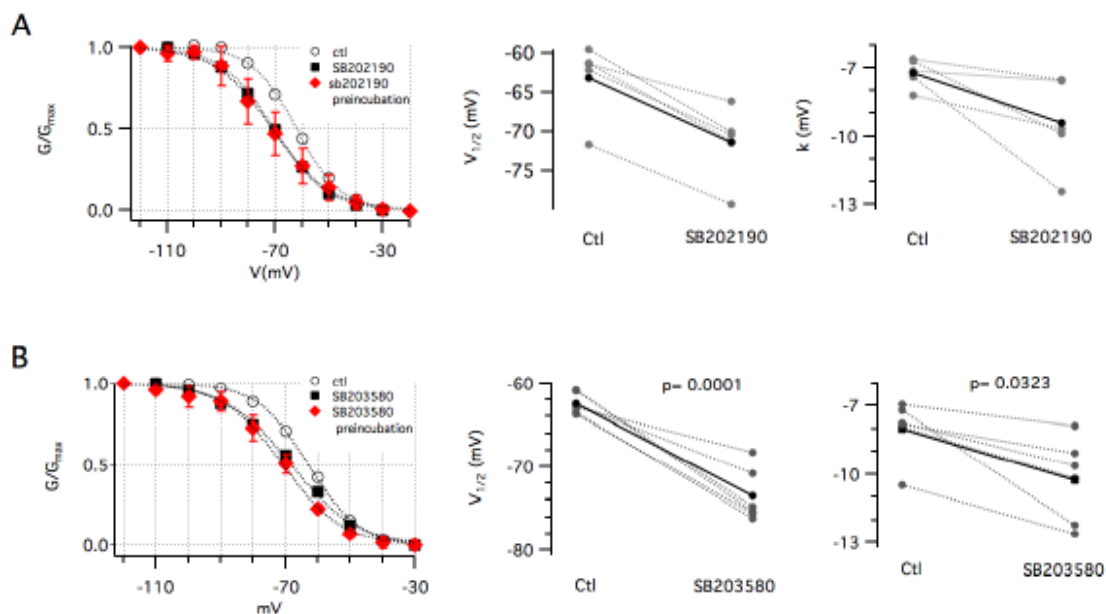
Figure 1.5 P38MAPK signaling modulates the *VAC* of I_h in adult MSO. 30 µM of SB202190 (A)
and 20 µM of SB203580 (B), both antagonists of P38MAPK results in ~10mV shift in *VAC* (p<
0.5) of I_h. Both these antagonists also result in increase in the slope of *VAC* (*k*) (p< 0.5). On the
left panels in both A and B is one representative experiment in Ctl and P38MAPK blocked case
(black). Also on the left panels are the pre-incubation with drug condition (red).
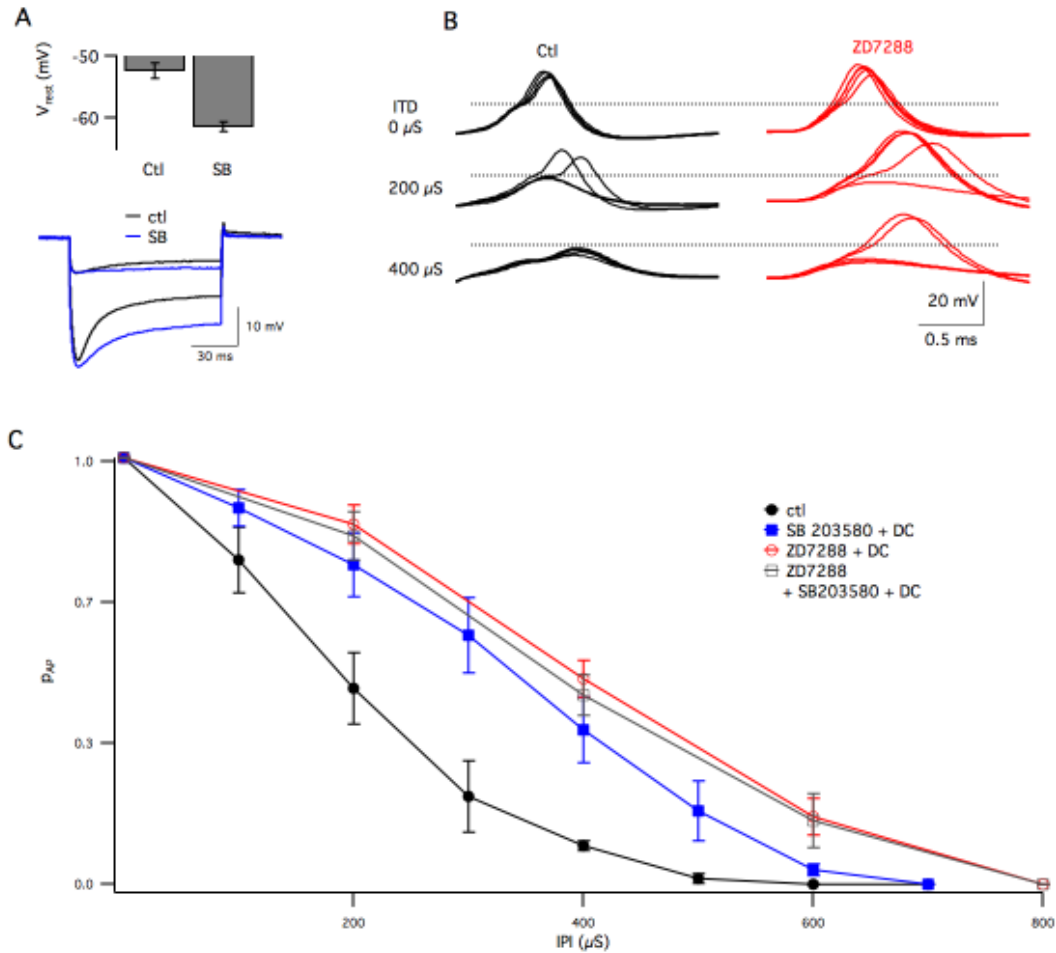
Figure 1.6 I_h properties are responsible for maintaining the brief synaptic coincidence window of MSO neurons. A. Not just presence of I_h but *VAC* is a key determinant of MSO neuron properties. In current clamp recordings, application of 20 µM SB203580 results in ~9mV shift in the resting potential of MSO. SB203580 also manifests in terms of reduced sag in response to hyperpolarization. The top panel shows group data for the change in resting potential, while at the bottom are traces from one representative experiment. B and C. The synaptic coincidence window of MSO was explored using bilateral synaptic EPSPs of near equal amplitude. In the control case (black traces) the probability of spiking decreases more than half in less than 200 µs, while in case of I_h using 50 µM ZD7288 (red traces), even when cell is artificially restored to same resting potential as control, the probability of spiking remains very high for comparable durations as control. This is demonstrated by overlapping 5 repetitions for different inter-pulse intervals (IPIs). The dashed lines are drawn to indicate the threshold for APs. The effect of modulating the *VAC* of I_h to hyperpolarizing potentials (by 20 µM SB203580) was almost the same as 50µM ZD7288. (n≥5 cells for each point).

DISCUSSION

In all mammals, the head size increases during postnatal development, manifesting in changes of auditory experience, especially the binaural timing information. We show that after hearing onset in gerbils (PND12) many developmental changes including changes in I_h, a key determinant of MSO properties takes place. We show that I_h conductance increases 9 fold, its *VAC* shifts by 30 mV, and kinetics hasten by 4 to 5 fold during one week of post-natal development. These changes correlate with a decreasing sensitivity of cAMP. In adult MSO we also find that PIP_2 and P38MAPK contribute to depolarizing *VAC* of I_h. I tested the functional consequences of I_h in MSO by exploring its role in the synaptic coincidence window. HCN channels and their unique properties in MSO were found to be the key determinants of ability of MSO neurons to perform sub-millisecond coincidence detection.

A parsimonious explanation for changes in the cAMP signaling during development is a transition from cAMP–sensitive subunits to cAMP–insensitive subunits; i.e. probably a transition from a mix of HCN2 and HCN1 to predominantly HCN1, especially if one considers the wealth of information from the expression systems (Altomare et al., 2003; Wahl-Schott and Biel, 2009). Nonetheless, caution needs to be observed in this interpretation because many other preparations where HCN2 is present in significant fraction still show developmental changes like hastening of kinetics and insensitivity to cAMP

(Vasilyev and Barish, 2002). In fact in some instances there is evidence of increase in cAMP levels in cells (Surges et al., 2006), yet a decline in cAMP signaling that researchers have argued as either a change of subunit or other modifications occluding cAMP signaling to HCN. Thus, if one considers the claim of HCN subunit identity based on the antibody staining data from rats (Koch et al., 2004) to be valid, along with my cAMP modulation data, one may argue for a subunit transition to HCN1 in the adult MSO.

In recent years, data on the potential of hetero-multi-merization (Much et al., 2003) many post-translational modifications, associations with rafts (Barbuti et al., 2004), even alternate splicing in invertebrates (Gisselmann et al., 2005; Ouyang et al., 2007) etc. makes the earlier opinion of cAMP insensitivity of I_h in some auditory brainstem neurons, like octopus neurons (Bal and Oertel, 2000) arising out of HCN1 subunit composition somewhat muddy.

Many auxillary subunits modify HCN properties, like MiRP1 (Qu et al., 2004), KCR1 (Michels et al., 2008) and Trip8b (Lipscombe and Pan, 2009). Of all auxiliary subunits, Trip8b seems like the strongest candidate for HCN modulation in MSO because its splice variants can have variable impact on I_h, including on cAMP sensitivity (Santoro et al., 2004; Lewis et al., 2009; Santoro et al., 2009; Zolles et al., 2009).

In LSO, a contralateral cochlear ablation causes a transient increase in g_h (Hassfurth et al., 2009), suggesting a role of activity in determining LSO I_h properties. The next steps in exploring development of HCN channels in MSO are two fold: whether high frequency activity, unusual for other brain regions is responsible for unique I_h properties and what is the underlying basis of cAMP insensitivity in adult MSO.

Chapter 4

Dynamic interactions between I_h and I_{K-LVA} shapes MSO responses to trains of inputs.

ABSTRACT

The bipolar neurons of the medial superior olive (MSO) have been postulated to encode sound–location cues, by detecting sub–millisecond coincidence of binaural inputs. There is no *in vitro* study of MSO neuron responses to physiological frequencies and durations. We used electrophysiological recordings from gerbil brainstem slices (35°C) and a point neuron model to address how the responses of MSO neurons are regulated by the dynamics of the two major conductances controlling the subthreshold synaptic integration: a low–voltage–activated potassium current (I_{K-LVA}) and a hyperpolarization–activated cation current (I_h). In the whole–cell–current and voltage–clamp recordings, we observed that both channel types contribute strongly to the resting membrane conductance. In current clamp, we found that for trains of simulated EPSPs (100–500 Hz), there was little change in peak depolarizations, due to the counteracting action of currents from these channels. On the other hand, as a result of cumulative I_h deactivation and I_{K-LVA} inactivation, input resistance increased during high–frequency EPSP trains (up to 60% for 1 to 2 s long, 15 mV EPSP train). These changes in membrane excitability accumulate and decay

gradually, at the time scales of physiological auditory stimuli, thus reporting linearly the frequency and amplitude of inputs. At the end of train the opposing currents of recovery from I_{K-LVA} inactivation and I_h deactivation counterbalance, resulting in a rapid reset of membrane potential to pre–train values. Thus, we find that the interaction of I_{K-LVA} and I_h is likely playing a central role in regulating the dynamical encoding of ongoing inter–aural sound disparity in MSO.

INTRODUCTION

The principal neurons of the medial superior olive (MSO) serve as the first stage for the processing of low–frequency binaural acoustic information. They signal the degree of temporal coincidence of inputs at the two ears through changes in firing rate (Goldberg and Brown, 1969; Yin and Chan, 1990; Brand et al., 2002; Grothe, 2003; Joris and Yin, 2007). This information is conveyed to the ipsilateral inferior colliculus (Henkel and Spangler, 1983). Apart from specializations in circuitry (Oertel, 1999), adaptations in the voltage– and ligand–gated conductances (Trussell, 1999) enable the transformation of phase–locked, temporally precise information, into cues for localization of sounds along the horizontal spatial axis.

Low–voltage–activated potassium channels (I_{K-LVA}) and mixed cationic hyperpolarization activated channels (I_h) are the two major conductances in the MSO, operating near resting potential (Svirskis et al., 2002; Scott et al., 2005) (Mathews et al. personal communication; Figure 2.1). I_h contributes to the high

resting membrane conductance and depolarized resting potentials of many neurons early in the auditory pathway, apparently enabling submillisecond temporal firing precision (Banks et al., 1993; Golding et al., 1995; Rodrigues and Oertel, 2006). I_{K-LVA} is also present in many early stations of auditory processing, enhancing the phase–locking and signal–to–noise ratio, and limiting the AP firing (Forsythe and Barnes-Davies, 1993; Reyes et al., 1994; Rothman and Manis, 2003; Rothman and Manis, 2003; Scott et al., 2005; Svirskis et al., 2002; Day et al., 2008) (Matthews, personal communication).

A modeling study has suggested a crucial role of I_h dynamics in the auditory encoding (Hooper et al., 2002). The dynamic role of I_h in regulation of excitability has been explored in non–auditory neurons (Magee, 1998; Magee, 1999) yet despite very high densities of I_h in auditory system no such experimental study has been conducted. I_{K-LVA} inactivation in avian analogous brainstem neurons is known to result in increase of firing rate and loss of spike timing precision (Slee et al., 2005; Kuznetsova et al., 2008).

In non–auditory systems, I_h is known to interact with various potassium channels. I_h inhibits EPSPs by interacting with M–type potassium channels (George et al., 2009) and is co–regulated in an activity–independent manner with A–type potassium channels (MacLean et al., 2005). I_h and I_{K-LVA} are co–expressed in many auditory neurons, sometimes in fixed proportions (Golding et al., 1999; Cao et al., 2007; Oertel et al., 2008) and are found to be co–localized in the same membrane regions of bushy cells (Oertel et al., 2008). Given the overlap in the

voltage range of I_h and I_{K-LVA} in many auditory neurons, a functional interaction is highly likely, yet currently unexplored.

In the absence of an understanding of the dynamic role of I_h and its interaction with I_{K-LVA}, we looked at the role of these conductances in MSO in response to high–frequency, simulated somatic current injections (EPSCs), enabling us to focus on post–synaptic mechanisms. We employed a point–neuron model to better dissect the dynamical interactions of these conductances during the trains of inputs. Using a combination of whole–cell current and voltage–clamp recordings and modeling, we observed that an interplay of the two channels results in a stable EPSP amplitude in MSO, using trains of high–frequency uniform amplitude stimuli. The opposition of the two conductances results in a rapid reset of membrane potential at the end of the train to pre–train values. We observed that the interaction of the two channels generates a history function of previous auditory stimulus in the form of an increased input resistance that accumulates over trains and decays much after the end of trains, over durations akin to physiological sound stimuli. We show that one role of cumulative I_h deactivation and I_{K-LVA} inhibition is to counterbalance the synaptic depression and this may be an important mechanism for limiting short–term adaptation to auditory stimuli. Overall, we observe that interactions between I_{K-LVA} and I_h are dynamically regulating the encoding of interaural time disparity by the MSO.

RESULTS

I_h and I_{K-LVA} determine membrane properties

We examined the electrophysiological properties of 206 principal neurons of the MSO. Principal neurons were readily distinguishable in current–clamp recordings, based on criteria established in previous *in vitro* patch–clamp studies (Scott et al., 2005; Svirskis et al., 2002). The features of principal neurons of MSO include bipolar morphology of their dendrites as viewed under IR–DIC optics, the display of strong outward rectification in the voltage range depolarized to the resting potential, and the initiation of a single small action potential in response to all suprathreshold current stimuli (Figure 2.1A). MSO principal neurons consistently exhibited low input resistances (average 8.2 ± 0.6 MΩ, n=9), apparent in the voltage–current relationship (Figure 2.1A, 2.1E, 2.1F). In the presence of 50 µM extracellular ZD7288 or 20 µM intracellular ZD7288 or 10 mM cesium, all of which are blockers of I_h, the resting potential hyperpolarizes, hyperpolarization induced sag is abolished and input resistance and membrane time constant increase substantially (Figure 2.1B, 2.1D, 2.1E, 2.2F, 2.1G). In presence of 80 nM DTX–k or combination of 1 mM 3,4 Di–AP and 200–µM 4–AP, blockers of Kv1.1 channels we observed an increase in action potential amplitude, reduction in after–hyperpolarization (AHP) and a significant increase in input resistance and membrane time constant (Figures 2.1C, 2.1D, 2.1E, 1.1F, 2.1G). Together, these results indicate that I_h and I_{K-LVA} are active at the resting

potential, and provide a powerful contribution to the low input resistance of MSO

principal neurons at resting potentials.
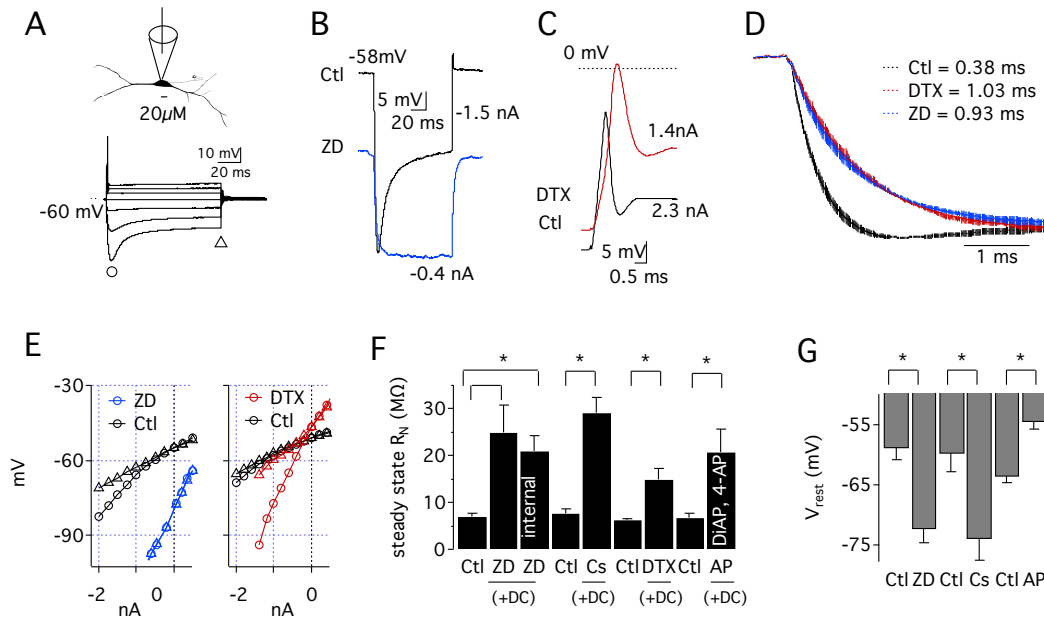
Figure 2.1. I_h and I_{K-LVA} determine the membrane properties of MSO. A. The bipolar neurons of MSO (top) fire phasically (bottom) in response to depolarizing square current pulses. Peak input resistance is measured for hyperpolarizing square current injection at open circles, while steady state input resistance is measured at open triangle. B. Application of I_h blocker (50µM ZD7288) results in hyperpolarization, an increase of input resistance and block of sag in hyperpolarization. C. Application of 80 nM DTX-K, a selective blocker of Kv1.1 results in increase of input resistance and broadening of action potentials. D. MSO neurons have fast membrane time constants, which are prolonged on blocking I_{K-LVA} and I_h. The traces are average of responses of different cells normalized to 1mV (n= 12 ctl, n=7 ZD, n=6 DTX). Time constants for ctl, DTX and ZD case are 0.38 ± 0.005, 1.03 ± 0.006 and 0.93 ± 0.005 ms respectively. E. Voltage current relationship of MSO neurons in control and I_{K-LVA} and I_h blocked conditions. In presence of ZD the cell hyperpolarizes and the input resistance increases significantly. In presence of DTX there is a similar increase in input resistance. F. Steady state input resistance of MSO neuron in case of I_h block (50 µM ZD7288, n=6 or 20 µM intracellular ZD7288, n= 4 or 10 Mm Cs, n=5) and I_{K-LVA} block (80 nM DTX-K, n=6 or 1 mM 3,4 DiAP + 200 µM 4-AP, n= 9) increases significantly. G. I_h and I_{K-LVA} contribute to resting potential of MSO. I_h is blocked by 50µM ZD7288 (n=6) or 10 mM Cs (n=5) and I_{K-LVA} is blocked by 1 mM 3,4 DiAP + 200 µM 4-AP (n= 9).

I_h has depolarized range of activation, hyperpolarized reversal potential, and high conductance in MSO

Given that I_h and I_{K-LVA} determine the input resistance of MSO, even when the cell is artificially brought to the same resting potential as control (Figure 2.1F), it is highly likely that these conductances are open at rest. I_{K-LVA} is well studied, including in MSO (Scott et al., 2005; Svirskis et al., 2002) but currently there is no biophysical characterization of I_h in MSO. Using whole–cell–voltage–clamp recordings in MSO, slow, non–inactivating inward currents were elicited with current steps from a holding potential of -30 mV to voltages between -40 and -110 mV. Subsequent blockade of the majority of the non–leak portion of the current by 50 μM ZD7288 (89.7±3.3% at -60 mV, n=5) confirmed that that these hyperpolarization–activated currents corresponded to I_h (Figure 2.2A). The activation of the channel was measured using tail currents generated at -100 mV following steps to voltages between -110 mV and -30 mV (Figure 2.2B). Conductances were calculated from the peak tail currents, and normalized to the maximum and minimum conductances. The normalized–conductance plot was fit well by a Boltzmann equation of the form $g/g_{max} = 1/(1+\exp[(V-V_{1/2})/k])$, where $V_{1/2}$ is the half–maximal activation voltage, and k is the slope factor. The average $V_{1/2}$ was -60.3 ± 0.2 mV with a k of -7.3 ± 0.2 mV (n=12). We are aware of the limitations of space–lamp problems in whole cell recordings (Williams and Mitchell 2008). Even when one considers space–clamp issues, the conductance estimates from MSO (average = 70.3 ± 9.0 nS, n=12) are at best an underestimate, placing it in one of the neurons with largest g_h. The reversal

potential of I_h was estimated using tail–current analysis. Maximal I_h was evoked with a 1 s step from -30 to -100 mV, followed by 1 s test pulses to voltages between -100 and -60 mV in 5 mV increments (Figure 2.2C). The reversal potential was estimated from linear fits to I–V relation extrapolated to 0 mV. The reversal potential averaged -40.1 ± 1.3 mV (n=12), which is quite negative for non–auditory neurons, but is comparable to auditory neurons with large g_h. The relatively negative reversal potential results in a small driving force for I_h during trains of EPSPs.
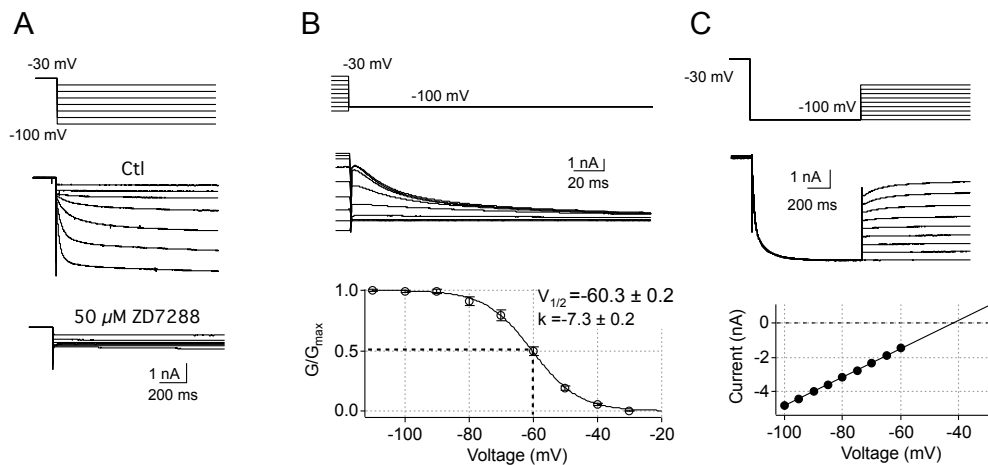
Figure 2.2. MSO has large resting h-conductance due to unique properties of I_h. A. Hyperpolarization-activated currents elicited by voltage commands from –30 mV to levels between –40 and –100 mV, at –10 mV increments. Non-leak currents are blocked extensively in the presence of 50 µM ZD7288 by (83% at –60 mV in this cell; avg = 89.7±3.3% at -60 mV, n=5). B. Voltage-dependence of I_h activation. I_h was activated with 2 s steps to voltages between –30 mV and -110 mV (10 mV steps, upper schematic diagram), and instantaneous tail currents were recorded at -100 mV (middle traces). Bottom graph: average instantaneous tail currents in 12 cells were converted to conductance and normalized to maximum and minimum values. The total g_h on average is = 70.3 ± 9.0 nS, n=12. C. Reversal potential of I_h. Activation of I_H is achieved with a 1 s prepulse to –100 mV, followed by a 1 s test pulse to voltages between -100 mV and -60 mV (5 mV increments, upper schematic diagram and middle traces). Bottom graph: The reversal potential of –41 mV in this cell was extrapolated from a linear fit to the instantaneous I-V relation of tail currents (solid line). Avg = -40.1 ± 1.3 mV (n=12).

Trains of brief EPSPs result in cumulative deactivation and inactivation of

I_h and I_{K-LVA}, respectively

Voltage–dependent changes in activation and deactivation of I_h and I_{K-LVA}

channels during trains of synaptic activity provide a powerful influence on resting

membrane properties. Although the brief duration of individual EPSPs in MSO

neurons (~1–2 ms) would not be expected to provide substantial changes in the

slow processes like I_h deactivation or I_{K-LVA} inactivation, such changes might

accumulate over a longer time window during repetitive synaptic activity. To

examine this question, we made whole–cell voltage clamp recordings from MSO

neurons and examined changes in resting I_h or I_{K-LVA} during trains of simulated

EPSPs (3–15 mV) delivered at 500 Hz from a holding potential of -60 mV (Figure

2.3, n=5). In I_h recordings trains of EPSP commands elicited not only the

corresponding trains of leak and capacitive currents, but a more slowly

developing outward current as well (Figure 2.3B). To quantify the amount of

current deactivated, we used tail current analysis by stepping the cell to -100 mV

at the end of trains (schematic, Figure 2.3C). This current is proportional to the

amplitude of the EPSP voltage commands (3–15 mV), and was blocked by >91%

in the presence of 50 µM ZD7288 (Figure 2.3B, 2.3D). Thus the slow outward

current was mediated by the cumulative deactivation of I_h during the train. In

each of these recordings, measurements were made of the voltage dependence

of I_h activation as well as its reversal potential using the stimulus protocols in

Figures 2.2B and 2.2C. From these data, we calculated the change in

conductance during the train relative to the resting conductance at -60 mV (Figure 2.3D, 2.3E). All these calculations are only exact if the neuron is a spherical, iso–potential object, with no cables (dendrites), but in a real neuron they serve to qualitatively illustrate the nature of change in conductance due to trains of EPSPs.

The same stimulus as in Figure 2.3A was used to study $I_{K–LVA}$ inactivation. Because of fast kinetics of $I_{K–LVA}$, tail–current analysis akin to I_h deactivation could not be applied for $I_{K–LVA}$ inactivation. In control (Ctl) case ($I_{K–LVA}$ isolated), apart from fast fluctuating dynamics of $I_{K–LVA}$ activation and deactivation, there is capacitative current and slowly developing $I_{K–LVA}$ inactivation (Figure 2.3F). The $I_{K–LVA}$ inactivation was converted to conductance by taking the potassium reversal to be –106 mV in MSO (Matthews, personal communication). Apart from these currents, during control cases, there is a conventional leak current and a leak component of $I_{K–LVA}$ open at –60 mV. Due to $I_{K–LVA}$ open at –60 mV, the percentage of $I_{K–LVA}$ inactivation as a fraction of $I_{K–LVA}$ activated, cannot be measured. Thus we measured percentage of $I_{K–LVA}$ inactivation as a fraction of total current (Figure 2.3H). These experiments demonstrate that both I_h and $I_{K–LVA}$ exhibit cumulative changes in conductance over long duration of individually brief inputs.
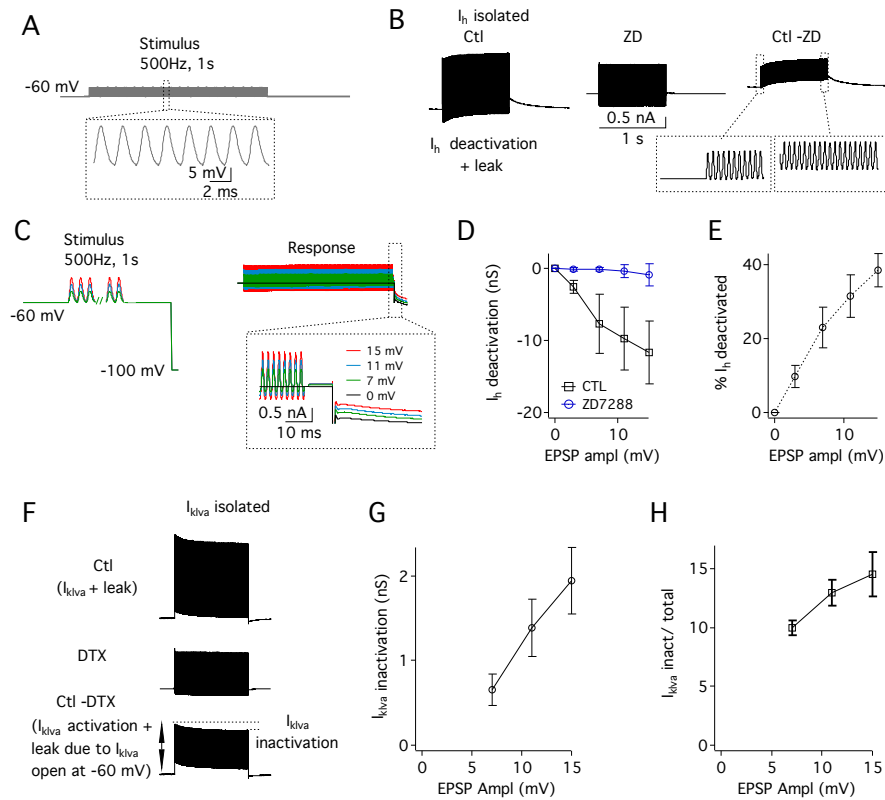
Figure 2.3. Trains of EPSPs can result in a cumulative deactivation of I_h and I_{K-LVA}. A. I_H was isolated pharmacologically in whole-cell voltage clamp recordings and voltage commands were delivered consisting of 500 Hz trains of EPSP-shaped waveforms between 0 and 15 mV). B. The current responses to each stimulus (only 15 mV shown here) consisted of both leak and capacitive currents over longer time scales a slowly developing outward current (Ctl) is apparent that is blocked in the presence of 50 µM ZD7288 (*expanded traces, bottom*). The ZD-sensitive current reflects both the contribution of HCN channels to the resting leak conductance as well as deactivation during EPSP train commands (Ctl-ZD7288). C. Stimulus protocol (left) as in A of variable EPSP amplitudes followed by a step to -100 mV to measure the tail currents. Right: Increasing amplitudes of the EPSP trains result in increasing I_H deactivation. D. Group data showing the average magnitude of g_h deactivated during EPSP trains between 0 and 15 mV (ΔG). Progressively larger stimuli led in turn to progressively larger deactivation of g_h up to 12 nS (n= 6). E. Percentage change in resting g_h following EPSP trains from 0 to 15 mV (ΔG /G_{max}*100). Subthreshold EPSPs of 15 mV can result in deactivation of ~40% of the resting g_h on average (n=6). F. The whole cell I_{K-LVA} isolated recordings to stimulus as used for I_H in A., shows a cumulative inactivation. The Ctl (I_{K-LVA} isolated) has leak, capacitive current and I_{K-LVA}, which exhibits both activation due to stimulus and steady activation component at –60 mV. 80 nM DTX-K blocks I_{K-LVA} G. Group data for voltage dependent increase in G_{klva} inactivation. H. Average percentage of I_{K-LVA} inactivated as a fraction of total I_{K-LVA} isolated (n=5).

69

An interaction of I_h and I_{K-LVA} maintains a relatively constant output of MSO over trains of EPSPs and rapidly resets membrane potential

Because EPSP trains result in a large change in I_{K-LVA} inactivation and I_h deactivation (Figure 2.3), a significant change in the EPSP amplitude over the trains and a significant change in resting potential might be expected in current–clamp recordings. Surprisingly, the absolute amplitude of the EPSPs during the train does not change much, as evinced by comparison of first, middle and the last two responses to a 500 Hz, 2 s long alpha current EPSP train normalized to second EPSP at the beginning of the train (Figure 2.4A, n=8). The after–train hyperpolarization (V_{aft}) also returns quickly to MSO resting potential at the end of the train. An increase in the frequency of the stimulus (9 mV EPSP train) up to 500 Hz only results in approximately 1 mV V_{aft} (n=8, Figure 2.4B left). Similarly V_{aft} is quite small for 500 Hz EPSP train of varying amplitudes (n=8, Figure 2.4B right).

In case of I_h block (extracellular 50 µM ZD7288 or intracellular 20 µM ZD7288) EPSPs show summation due to increased input resistance, with after–train potential showing small depolarization, which is a manifestation of underlying I_{K-LVA} inactivation (Figure 2.4C, Figure 2.7). The V_{aft} shows small depolarization in case of ZD7288 (Figure 2.4C, 2.4D).

When I_{K-LVA} was blocked by DTX–K (80 nM) the absolute EPSP amplitude declines over the train, while the V_{aft} is hyperpolarized (Figure 2.4C, 2.4D). The

70

individual response to single alpha current injection is much broader than control due to an increase in the input resistance of the neuron and the lack of active hyperpolarization of EPSPs. The shape of the EPSP train is affected by the lack of I_{K-LVA} inactivation. In case of I_{K-LVA} block, more I_h is deactivated due to larger integral depolarization. A combination of increased I_h deactivation and high input resistance results in large V_{aft} (Figure 2.4C).

Thus, in control conditions, a balance of I_{K-LVA} inactivation and I_h deactivation during the trains results in a net constant amplitude of EPSP amplitude over the trains and a "clamped" resting potential at the end of the train. These pharmacological manipulations are highly suggestive of interplay of I_h and I_{K-LVA} resulting in the output of MSO.
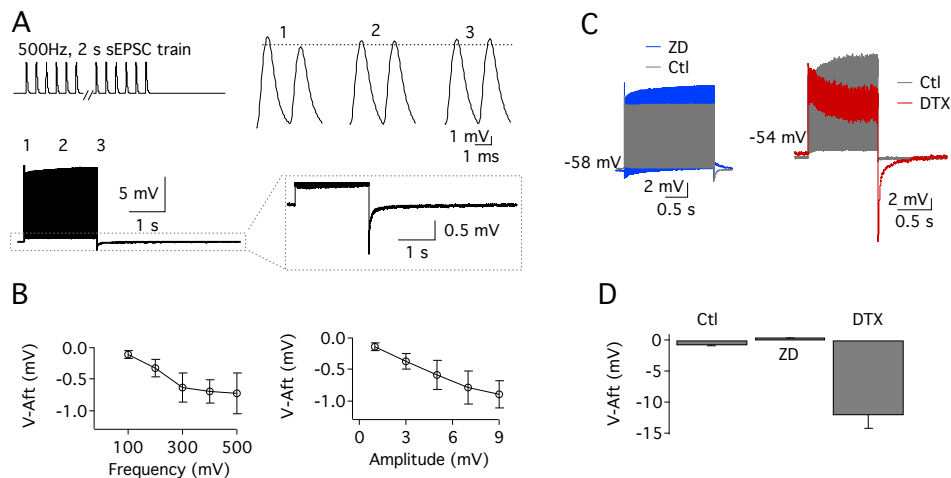
Figure 2.4. MSO neurons regulate constant amplitude of EPSPs and exhibit quick return to resting potential. A. In response to constant amplitude simulated somatic current injected EPSCs (schematic: top left), the amplitude of EPSPs were measured. The responses of 8 neurons (with second EPSP response ~9 mV) were normalized to second EPSP and averaged. Top right shows the EPSP amplitude of the first, middle and last two EPSPs of the train. The after-hyperpolarization at the end of the train (V_{aft}) also returns quickly to original resting potential

values (bottom left). B. Increase in the frequency (left) of 9mV or amplitude (right) of 500Hz, 1s long EPSC train does not result in a strong increase in AHP (n=8). C. Blocking I_H or I_{K-LVA} perturbs the constancy of MSO response to trains of inputs. Voltage responses to the stimulus protocol in A. recorded in normal ACSF (Ctl, gray), and in 50 µM ZD7288 (left, blue) and 80 nM DTX-K (right, red). D. Blocking I_H results in slightly depolarizing V_{aft} while blocking I_{K-LVA} results in strongly hyperpolarizing V_{aft} (n=15 ctl, n = 9 ZD and n=8 DTX).

EPSP trains result in a large increase in input resistance, with the amplitude and frequency of stimulus.

The functional impact of the cumulative deactivation of I_h and I_{K-LVA} during and after the EPSP train is to offset the membrane potential, but, given that both these conductances contribute heavily to the input resistance, one may expect an increase in the membrane excitability at the end of long EPSC trains. We made whole–cell current–clamp recordings from the somata of the MSO principal neurons, and injected trains of simulated EPSCs (500 Hz, 1s duration; n=11). In these experiments the amplitude of the current injection was adjusted to elicit EPSPs of between 8–10 mV, which required currents of between 0.8 and 3.2 nA. To monitor the state of resting conductances, the input resistance was measured with small hyperpolarizing current pulses (10 ms duration, 100–450 pA pulses resulting in 3–5 mV hyperpolarization), delivered 150 ms before and 10 ms after the stimulus train (schematic top Figure 2.5A). The input resistance increased by an average of 39.2±3.9% (ranging from 31% to 72%) when measured 10 ms after stimulus offset, when deactivation of low voltage potassium current was complete.

To understand what aspects of the stimulus train were critical for regulating the input resistance, we manipulated stimulus frequency and amplitude independently of one another (Figure 2.5B). In one set of experiments, stimulus amplitude and duration were kept constant (9 mV, 1 s), and stimulus frequency was varied from 100 to 500 Hz (n=5). A small increase in input resistance was detected at 100 Hz, and these changes increased linearly with frequency reaching a maximum of 23.7%, at a rate of 4.5% per 100 Hz (Figure 2.5B, left graph). In some of the same cells EPSP amplitude was varied while the frequency and duration of the EPSP train were held constant (500 Hz, 1 s). The increase in input resistance varied linearly with EPSP amplitude from 8% to 60% on average, over the sub–threshold voltage range up to 15 mV above rest (Figure 2.5B, right graph).

To observe the time course over which input resistance changes develop, we delivered EPSC trains of uniform amplitude and frequency (adjusted to elicit 8–10 mV EPSPs at either 250 or 500 Hz) and varied train duration from 10 ms to 2000 ms (Figure 2.5C). The increase in input resistance of MSO principal neurons could be fit well with a dual exponential function (Figure 2.5C). For 500 Hz EPSP trains, the fast and the slow time constants averaged 45.1 ± 10.1 ms and 915.9 ± 215 ms, respectively, whereas for a 250 Hz train, time constants approximately doubled, at 74.8 ± 34.7 ms, and 1642.3 ± 1940 ms. Once initiated, input resistance changes were long lasting. The time course of input resistance decay was assessed using either a 200–ms or 2000–ms stimulus train (9 mV

EPSPs at 500 Hz; Figure 2.5D). As with the development of the increase in input

resistance, the decay of input resistance followed a dual exponential time course.

The decay of input resistance from the 200 ms train was significantly more rapid

than for the 2000 ms train (for 200 ms: τ_{fast} = 24.1 ± 5.4 ms, τ_{slow} = 231.5 ± 57.3

ms; for 2000 ms: τ_{fast} = 36.6 ± 1.9 ms, τ_{slow} = 440.9 ± 28.7 ms).
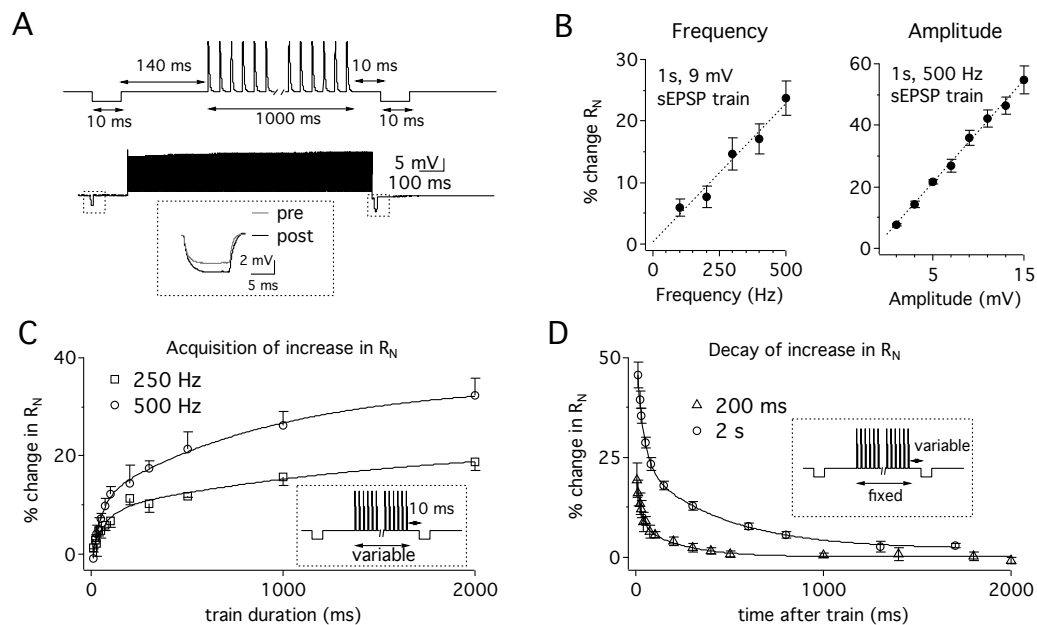
Figure 2.5. Trains of simulated synaptic stimuli trigger increase in input resistance, which accumulates and decays at slow rates, reporting the frequency and amplitude of input train. A. Top: (Schematic) Input resistance was probed 140 ms before and 10 ms after a 1 s, 500 Hz train of EPSCs using short hyperpolarizing test pulses (10 ms duration, -300 pA amplitude). EPSC amplitude was adjusted to produce EPSPs of ~9 mV. Voltage responses to the input resistance probes, exhibit increase in amplitude due to trains of EPSPs (middle). Expanded view of pre and post-stimulus input resistance measurements produced a 25% increase in input resistance in this example. B. Input resistance changes are linearly related to both amplitude and frequency of EPSP trains. Left panel: R_N changes induced by a train of 9 mV EPSPs of varying frequency. Linear fit (dotted line): 4.5%/100 Hz. Right panel: R_N changes induced by a 500 Hz train of variable amplitude. Linear fit (dotted line): 4.6%/mV. C. The increase in input resistance is gradual and biexponential. Subthreshold EPSP trains of 9 mV are delivered at either 500 (open circles, n=5), or 250 Hz (open squares, n=4), and varied in duration between 10 and 2000 ms (schematic: dotted inset) while input resistance is measure 10 ms after the train. Time constants for 500 Hz train are 45.1 ± 10.1 ms and 915.9 ± 215 ms, and for 250 Hz train are 74.8 ± 34.7 ms, and 1642.3 ± 1940 ms respectively. D. The input resistance changes last for 100s of milliseconds. Subthreshold 500 Hz EPSP trains of 9 mV are delivered either for 2000 ms (open circles, n=9) or 200 ms (open triangles, n=5), while the post train input resistance is measured at

varying intervals after train (schematic: dotted inset). The time constants for the decay of input resistance increases for 200 ms train are 24.1 ± 5.4 ms and 231.5 ± 57.3 ms, while for 2000 ms train are 36.6 ± 1.9 ms and 440.9 ± 28.7 ms.

$I_{K–LVA}$ inactivation and I_h deactivation results in a cumulative increase of input resistance

In experiments similar to those described in Figure 2.5A, input resistance changes were blocked by 80% in the presence of extracellular 50 µM ZD7288 (Figure 2.6A, 2.6B, n=6, 8.7±4.0% change in input resistance in ZD7288, vs. 44.2±6.2% in control), or 85% in presence of intracellular 20 µM ZD7288 (n=5) or 10 mM extracellular cesium (88% input resistance reduction; n=5). These changes were also partially blocked (57%) by blocking $I_{K–LVA}$ (80 nM DTX–k, n=9, Figure 2.6A, 2.6B).   Thus both I_h and $I_{K–LVA}$ are contributing to cumulative increase of input resistance in MSO.

The experimental results strongly suggest a dynamic interaction of the two conductances; however due to limitations of the pharmacological approaches and different starting input resistances in different conditions like I_h or $I_{K–LVA}$ block we cannot quantitatively dissociate the separate effects of $I_{K–LVA}$ inactivation and $I_{K–LVA}$ activation/deactivation block. Thus we explore these issues in more detail in a point–neuron model. The single–compartment neuron model includes three ionic currents: the voltage–dependent I_h and $I_{K–LVA}$, and a passive membrane current I_L. All parameters and current descriptions were based on experimental data from MSO cells (see Methods). Unknown

parameters (peak conductance of g_{K-LVA} and leak, and the leak reversal potential) were set such that we could account for experimental measurements of the input resistance R_N, membrane time constant τ_m, and the resting membrane potential V_{rest}.
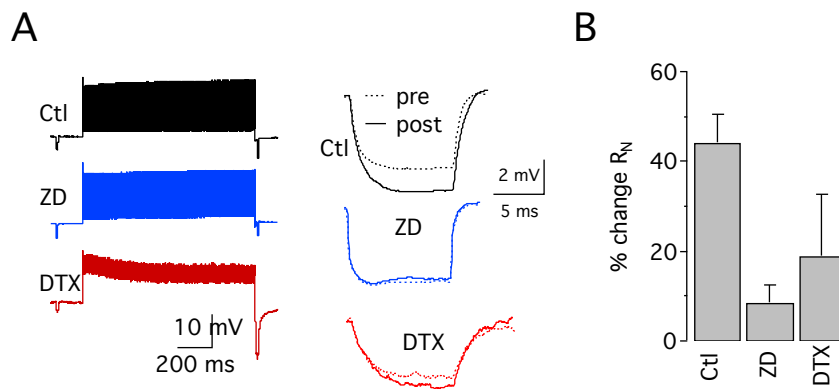
Figure 2.6. Ih and IK-LVA mediate dynamic regulation of input resistance. A. Voltage responses of trains (left) in normal ACSF (Ctl: top), I_h block (middle) in the presence of 50 µM ZD7288 and I_{K-LVA} block (80 nM DTX-K). Right traces: Expanded view of pre and post-stimulus input–resistance measurements in Ctl, ZD7288 and DTX-K conditions. Input resistance changes were diminished in I_h or I_{K-LVA} block. B. Summary of group data showing sensitivity of input resistance changes in control, I_h (n=6) and I_{K-LVA} blockers (n=9).

Model illustrates cumulative deactivation of I_h and inactivation of I_{K-LVA} during train and its resulting decrease of the total membrane conductance g_m

Simulating the response to trains of EPSCs under control conditions reproduced the experimental recordings remarkably well (Figure 2.7). The model shows a relatively constant amplitude EPSP train followed by a fast restoration of the

resting membrane potential (Figure 2.7A). With the model we show the dynamics that underlie these responses. We see fast fluctuations in I_{K-LVA} activation and a slow cumulative deactivation of I_h and cumulative inactivation of I_{K-LVA} (Figure 2.7B, 2.7C). As a result the total membrane conductance g_m (i.e., the sum of instantaneous conductances) decreases over the course of the 1 s EPSC train (Figure 2.7D). Following the input train, g_m is decreased by ~24% and recovers to values close to baseline levels over the next ~300 ms.

While we find strong deactivation of I_h and inactivation of I_{K-LVA}, the amplitude of the EPSP train remains fairly constant (insets Figure 2.7A, 2.7B). A central factor in this is that the I_h deactivation and I_{K-LVA} inactivation counter each other (Figure 2.7B), producing simultaneous decreases of an inward current and an outward current. Note that the counteraction of I_h deactivation and I_{K-LVA} inactivation is also observed at much lower or higher EPSC train frequencies, than 500–Hz (data not shown).

The hyperpolarization after the train has a surprisingly small amplitude (~1.5 mV) considering the large conductance changes that occur during the input train (Figure 2.7D). We computed the time course of the after–train potential V_{aft}, i.e., the voltage to which the cell relaxes immediately after the input ends (see Methods). This variable shows whether deactivation of I_h and (in)activation of I_{K-LVA} have a net depolarizing or hyperpolarizing effect on the membrane potential. We find that V_{aft} gradually hyperpolarizes with the duration of the EPSC train

(green trace in Figure 2.7A). After the stimulus ends, the membrane potential tracks V_{aft}. The small change in V_{aft} results from the opposing effects that I_h deactivation and I_{K-LVA} inactivations have on the membrane potential.
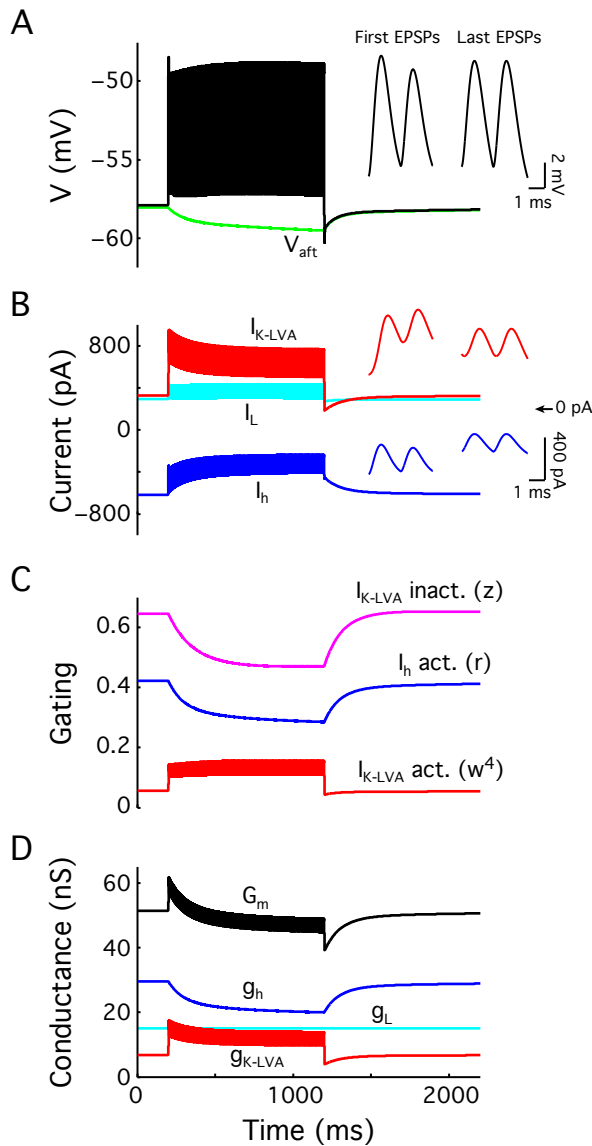
Figure 2.7. Model illustrates cumulative deactivation of I_h and inactivation of I_{K-LVA} during EPSC train and its resulting decrease of the total membrane conductance G_m. Model input consists of 1 second 500 Hz EPSC trains with 850 pA peak amplitude. A. Membrane potential (black curve) and instantaneous resting potential (V_{aft}, green curve). Inset: zooms of the first and the last two EPSPs. B. Ionic currents I_{K-LVA} (red), I_h (blue) and I_L (cyan). Inset: zooms of current traces during

first and last two EPSPs. C. Gating variables: $I_{K\text{-LVA}}$ activation (red), $I_{K\text{-LVA}}$ inactivation (magenta) and I_h activation (blue). D. Conductances of individual ionic currents $g_{K\text{-LVA}}$ (red), g_h (blue), g_L (cyan) and their sum g_m (black).

Simulations show buildup and decay of input resistance R_N during and after EPSC trains under control and current block conditions

The above simulation illustrates the dynamics of the model but does not show the R_N increases during and after the EPSC train. For a single–compartment cell model with a passive membrane, R_N is simply equal to R_m (i.e., the reciprocal of the total membrane conductance G_m). However, this is not true for a cell with subthreshold membrane currents that are strongly voltage–dependent. Injecting currents into MSO cells yields input resistances that are typically very different from R_m. Measuring the model's R_N with a 100 ms hyperpolarizing pulse (as in Figure 2.1F) gives an R_N of 8.5 MΩ, while the cell's total resting membrane resistance is 19.5 MΩ.

The model shows R_N increases in response to EPSC trains that match closely to the experimental results. We simulated experiments as in Figures 2.5 and 2.6, determining R_N by injecting 10 ms current pulses before and after a 1 sec EPSP train. The model produces an R_N increase of 41.1% relative to initial values (see also Figure 2.6C). With the model we can show the gradual increase of R_N with the duration of the EPSC train and its decay back to baseline levels after the stimulus ends (Figure 2.8A, solid line in middle panel, left column). The reciprocal of R_N is the input conductance G_N, which is the sum of g_L, g_h and $g_{K–LVA–eff}$ (Figure 2.8A bottom panel, left column). $G_{K–LVA–eff}$ is the effective $g_{K–LVA}$

conductance and incorporates the effects of its fast voltage–dependent properties (see Methods). Note that it exceeds $G_{K–LVA}$ (see Figure 2.7D). The computation of $G_{K–LVA–eff}$ and R_N makes use of the fact that $I_{K–LVA}$ activation acts on a time scale of ~1 msec and reaches its steady state level well within a 10 ms current pulse, while both $I_{K–LVA}$ inactivation and I_h activation are much slower (with time constants of at least tens of milliseconds) and hence remain approximately constant during a 10 ms current pulse. We observe large decreases in $g_{K–LVA–eff}$ and somewhat smaller decreases in g_h under control conditions.

Also the model reproduces the R_N increases that are observed under I_h or $I_{K–LVA}$ block. We first determined R_N by injecting 10 ms current pulses before and after a 1 sec EPSP train (see Figures 2.5 and 2.6). The model produced relative R_N increases of 11.5% and 22.7% with respect to initial values, under I_h block and $I_{K–LVA}$ block, respectively, fitting well with the experimental data (Figure 2.6C). The time course of the R_N increases show a relatively small buildup of R_N under I_h block (ZD, middle column in Figure 2.8A), resulting solely from a decrease of $g_{K–LVA–eff}$. Note that the decrease is smaller than under control conditions (see below). Under $I_{K–LVA}$ block (DTX–K, right column in Figure 2.8A) we find that the initial R_N for 10 msec pulses has approximately doubled. During the EPSP train, R_N increases strongly, resulting from strong deactivation of g_h.

The relative increase of R_N during the stimulus and decay of R_N after the stimulus

(Figure 2.8B) under control conditions compares favorably with the experimental data (Figure 2.5C and 2.5D, respectively). Figure 2.8B shows that most (67 %) of the relative R_N increases persist under I_{K-LVA} block but are greatly reduced (24 %) under I_h block. Considering only these results suggests that I_h deactivation is the dominant factor in explaining the observed R_N increases. However, the model shows a large contribution of I_{K-LVA} to these increases under control conditions (Figure 2.8A, bottom panel). The key factor underlying this seemingly contradictory result is the strong sensitivity of I_{K-LVA} activation to the membrane potential. Under control conditions we find a small hyperpolarization of V_{aft}. However, we find a depolarization of V_{aft} when I_h is blocked, because the effects of I_{K-LVA} inactivation on V_{aft} are not countered by I_h deactivation (Figure 2.8A, middle column). At this depolarized potential I_{K-LVA} is more strongly activated, partly countering the inactivation of I_{K-LVA}. Hence $G_{K-LVA-eff}$ decreases less during the EPSC train than under control conditions, and consequently we find a smaller R_N increase during the EPSC train. Also note that when I_{K-LVA} is blocked, the effects of I_h deactivation on R_N are larger because g_h forms a larger fraction of the total membrane conductance (Figure 2.8A, right column).

Because the contributions of I_h and I_{K-LVA} to the R_N increases can be overestimated and underestimated, respectively, with the blocking experiments due to the different voltage time courses, we adjusted for these different time courses by computing R_N at one particular voltage (at V_{rest} = -58 mV). We then see that the relative R_N increases under all three conditions are in fact very
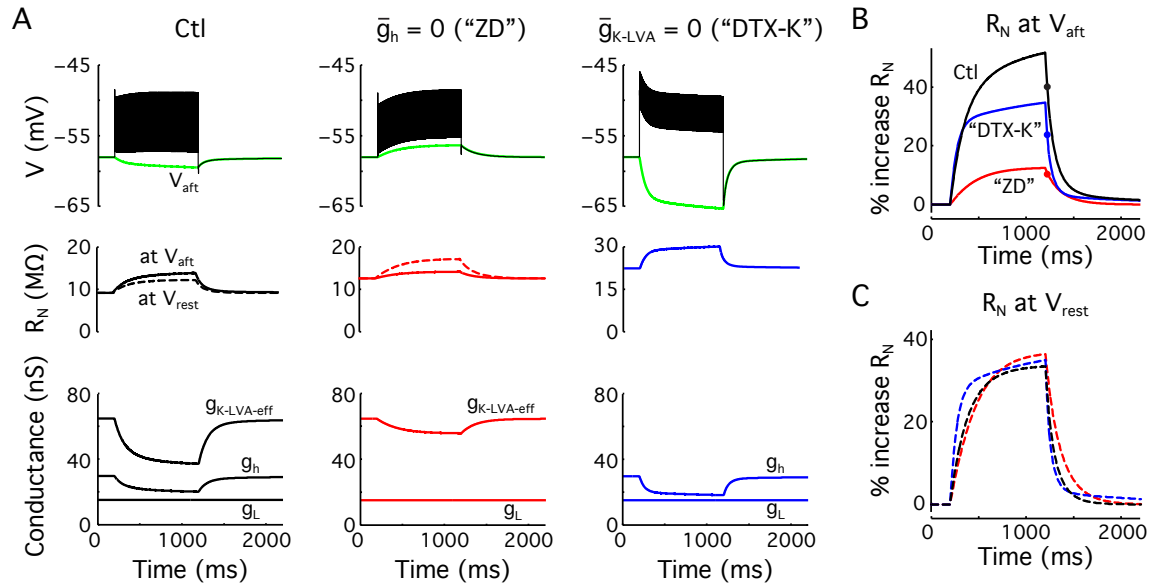
similar (dashed curves in Figure 2.8A–C).

Figure 2.8. Simulations showing buildup and decay of input resistance R_N during and after EPSC trains under control conditions, I_h block or I_{K-LVA} block. A. Top panels: membrane potential (black) and instantaneous resting potential V_{aft} (green) during 500 Hz EPSC train under control (Ctl), I_h block ("ZD") and I_{K-LVA} block ("DTX-K"). As in the experiments, the V_{rest} under I_h block or I_{K-LVA} block is restored to control values (-58 mV) with a bias current. The peak EPSC amplitude is adjusted to obtain a mean train peak amplitude of 9 mV under all three conditions. Middle panels: time course of input resistance R_N during and after the input train. R_N is computed for short (10 msec) pulses at the instantaneous resting potential (solid curves) or at V_{rest} (-58 mV) (dashed curves). Note that both R_N measurements overlap under DTX-K conditions. Bottom panels: time course of effective conductances underlying R_N: g_h, g_L and $g_{K-LVA-eff}$. The three conductances sum up to the input conductance, i.e., the reciprocal of R_N. The effective I_{K-LVA} conductance $g_{K-LVA-eff}$ at V_{aft} consists of two terms: the instantaneous voltage-dependent conductance and a derivative term resulting from fast voltage-dependent recruitment of I_{K-LVA} (see text). Note that g_h and g_L under control conditions are as in Figure 2.7D. B. R_N data from panel A, computed relative to initial R_N values, with R_N determined at V_{aft}. Marks relate to experimental measurements in Figure 2.6C. C. Relative increases in R_N during and after EPSC trains, with R_N determined at resting potential V_{rest} (-58 mV), see dashed red curves in middle panels of A.

Long EPSC input trains lead to large R_N increases and small changes in V_{aft} over a wide range of I_h and $I_{K–LVA}$ peak conductances

The large relative increases in R_N and small changes in V_{aft} described above can

be obtained over a large range of peak conductances $\bar{g}_h$ and $\bar{g}_{K\text{-}LVA}$. Using the model we varied $\bar{g}_h$ and $\bar{g}_{K\text{-}LVA}$ from 0 to more than double the control values used in Figures 2.7 and 2.8, and determined both the after train potential V_{aft} (Figure 2.9, top panel) and the relative increase in R_N (Figure 2.9, bottom panel) resulting from long EPSC trains (see Methods). The contour plots of V_{aft} show a linear relation between $\bar{g}_h$ and $\bar{g}_{K\text{-}LVA}$, illustrating that both peak conductances need to co-vary in order to maintain a constant V_{aft}. Increases of $\bar{g}_h$ produce stronger hyperpolarization of V_{aft}, and conversely, increasing $\bar{g}_{K\text{-}LVA}$ depolarizes V_{aft}.

The model produces R_N increases after long EPSC trains over the entire range of $\bar{g}_h$ and $\bar{g}_{K\text{-}LVA}$ shown in Figure 9 (bottom panel). Increasing $\bar{g}_h$ leads to larger %R_N increases. However, increasing $\bar{g}_{K\text{-}LVA}$ can lead to smaller %R_N increases. The depolarizing effect of $\bar{g}_{K\text{-}LVA}$ on V_{aft} is key to explaining this effect. More depolarized potentials lead to increased $I_{K\text{–}LVA}$ activation, counteracting the buildup of $I_{K\text{–}LVA}$ inactivation and its effects on R_N.

Experimentally observed values of V_{aft} and relative R_N increases can be accounted for by a large range of peak conductances (dashed lines in Figure 2.9), emphasizing that the results are robust to the naturally observed variations in $\bar{g}_h$ and $\bar{g}_{K\text{-}LVA}$. Examples traces are shown for the control model (filled circle); a model with $\bar{g}_{K\text{-}LVA}$ doubled (filled triangle); and a model with $\bar{g}_h$ and $\bar{g}_{K\text{-}LVA}$ halved (filled diamond). All three models show dynamics that agree with the

experimentally observed values for V_{aft} and %R_N increases. Note that the models

do differ in the amount of temporal summation of the EPSPs. Central in

explaining this difference is the membrane time constant of the three models,

which is considerably larger for the model with $\bar{g}_h$ and $\bar{g}_{K\text{-}LVA}$ halved, than for the

model with $\bar{g}_{K\text{-}LVA}$ doubled.
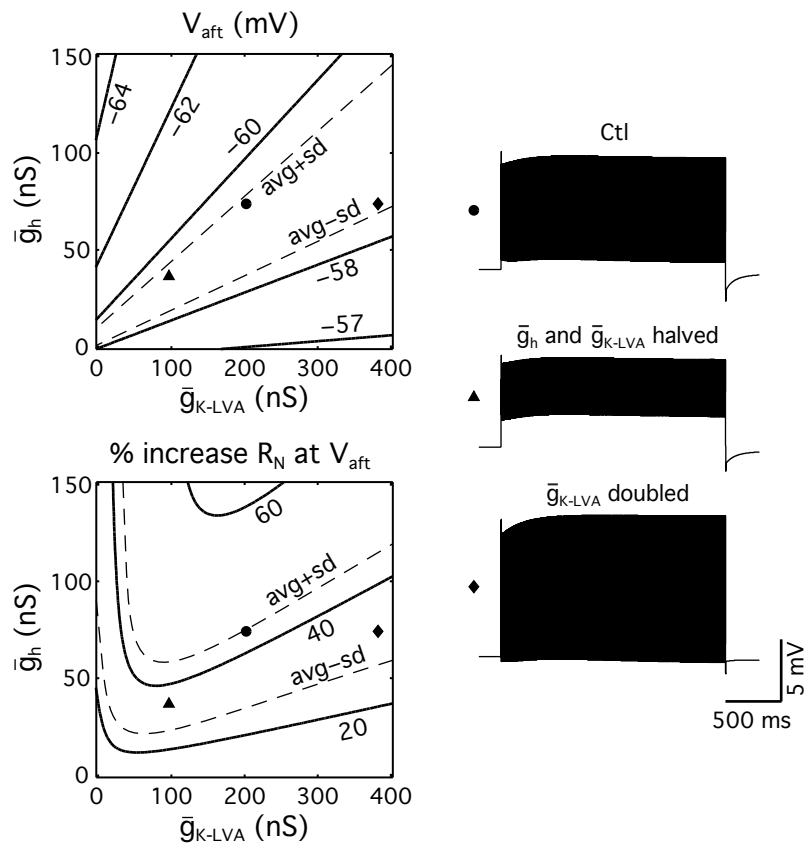
Figure 2.9. Long EPSP input trains lead to small changes in Vaft and large changes in R_N over a wide range of I_h and $I_{K\text{-}LVA}$ conductance densities. Left panels show change in V_{aft} (top) and percent change in R_N determined at V_{aft} (bottom) that accumulate after long (> 500 ms) trains of EPSPs with 5 mV mean depolarization (see Methods). Experimentally observed range of V_{aft} and R_N changes are denoted by dashed contour lines 'avg+std' and 'avg-std'. Three example voltage traces are shown for varying peak conductance densities: top trace (filled circle) uses same $g_h$bar and $g_{K\text{-}LVA}$bar as Ctl model in Figures 2.7 and 8; middle trace (filled triangle) uses half the $g_h$bar and $g_{K\text{-}LVA}$bar values of the Ctl model; bottom trace (filled diamond) uses twice the $g_{K\text{-}LVA}$bar and equal $g_h$bar as the Ctl model. Note that a bias current is added to obtain a resting potential of -58 mV for all combinations of $g_h$bar and $g_{K\text{-}LVA}$bar.

Cumulative decrease in membrane conductance is only sensitive to cumulative membrane depolarization

One may expect trains of action potentials to further increase the increase in input resistance, above and beyond large EPSPs. Nonetheless when EPSP amplitude was adjusted to consistently trigger action potentials, the average change in input resistance in response to a 500 Hz stimulus increased further (53.2±7.7%, n=21, data not shown). This is due to the fact that the action potentials in MSO are really small (Scott et al., 2005; Scott et al., 2007) making the net depolarization due to action potential similar to a large EPSP.

Both the experimental and modeling results demonstrate that I_h and $I_{K–LVA}$ mediated gain changes develop cumulatively, and persist on a time scale of tens of milliseconds to seconds. To assess the sensitivity of these gain changes to variable temporal patterns, we constructed trains of brief depolarizations of identical average frequency but differing in their degree of regularity. These trains (0.5 ms step pulses, 350 Hz average frequency, 1s duration) were constructed with interspike intervals (ISI) that randomly varied according to a Gaussian distribution with a mean standard deviation either of 0, 0.5, 1.0, 1.5, or 2.0 ms (Figure 2.10A). Ten random train patterns exhibiting each standard deviation of ISI were generated, delivered to MSO principal cells in current clamp mode, and input resistance changes were determined as in Figure 2.4A. In these experiments, stimulus intensity was adjusted to elicit supra–threshold responses in order to augment input resistance changes and improve the ability to

discriminate subtle changes in input resistance. In each cell, neither the mean nor the variance of the input resistance changes was altered by decreases in the regularity of the input trains (Figure 2.10B; no statistically significant difference across different SD conditions; $p > 0.6$, ANOVA). For this analysis, the standard deviations of the input resistance measurements were normalized to the respective mean values. If I_h deactivation or I_{K-LVA} inactivation was sensitive to the short–term temporal structure of the input train then with increasing values of standard deviations of ISI, there should be a systematic increase in the variance of the input resistance measurements. However, no systematic differences were observed in the five cells tested, with the mean standard deviation of input resistance changes ranging from 3.3 to 4.0% across the different conditions of stimulus regularity (Figure 2.10C). In addition, the mean input resistance change recorded in these cells was also consistent, ranging from 22% to 26%. These results show that I_h and I_{K-LVA} mediated gain change are determined by the average level of synaptic excitation, and are comparatively insensitive to its fine temporal structure.
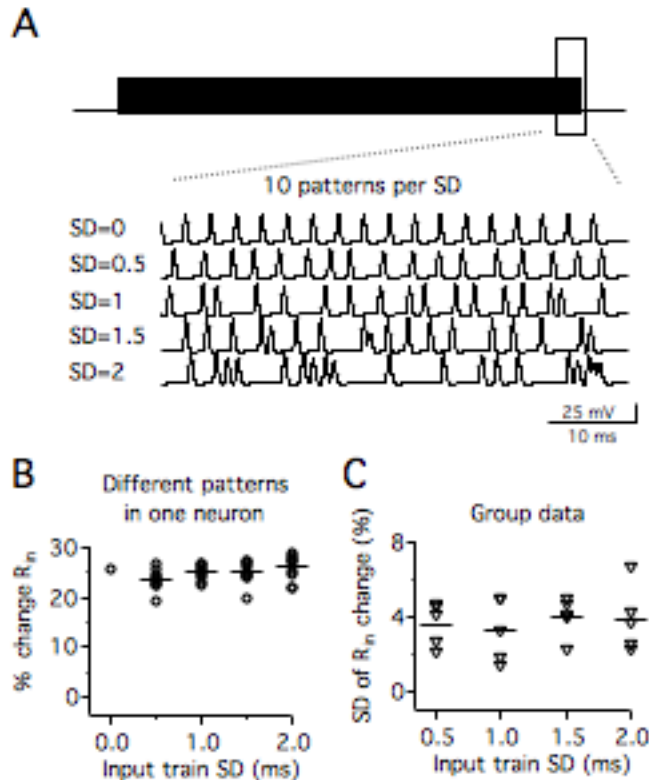
Figure 2.10. Changes in intrinsic gain are relatively insensitive to the pattern of membrane depolarizations. A. Trains of suprathreshold depolarizations (0.5 ms, 4.8 nA square pulses, 350 Hz train for 1 s) were constructed to exhibit varying degrees of regularity. The inter-spike interval (ISI) of each stimulus with a train was varied according to a Gaussian distribution with a standard deviation (SD) of either 0 (uniform ISI), 0.5, 1, 1.5, or 2 ms. Ten random patterns of stimuli were generated for each nonzero value of SD (only one excerpt is shown for each SD). B. Percent change in input resistance does not change systematically as a function of train regularity. Points within each SD category represent input resistance changes for a different random pattern. Average input resistance changes represented by thick bars. C. The average variance (thick bars) of input resistance changes does not vary systematically with variance in the regularity of the input train.

Increase in input resistance counteracts synaptic depression

How might I_h and I_{K-LVA} mediate gain changes manifest themselves in response to realistic patterns of high frequency auditory excitation? To address this question, we used voltage–clamp recordings to characterize the patterns of EPSCs to high frequency stimuli at the synapses between bushy cells and MSO

principal neurons. As expected, averaged responses to activation of contralateral excitatory inputs at frequencies of 250, 350, or 500 Hz showed strong synaptic depression after 1 second (74, 82, and 88%, respectively). Synaptic depression followed a dual time course at all frequencies. At higher frequencies, asynchronous release of neurotransmitter was apparent both during the train and for tens of milliseconds afterwards (Figure 2.11A). However, single trials exhibited a high degree of variability in EPSC amplitudes (Figure 2.11A, 2.11B). In the example in Figure 2.8B, in response to 500 Hz synaptic stimulation individual EPSCs between 0.5 and 1 s could far exceed the average, and were reflected in the amplitude distributions of individual trials in single experiments (Figure 2.11C) as well as the average EPSC amplitude distributions across the population of recorded MSO neurons (Figure 2.11D). These results indicate that excitatory synapses on MSO principal neurons exhibit a remarkable capability for maintaining effective synaptic transmission during long trains of presynaptic activity.

To test the functional significance of these input resistance changes due to cumulative increase in conductance, we decided to reduce the cumulative loss of total MSO conductance and replace it by equivalent amount of voltage–insensitive conductance (leak). Given that I_{K-LVA} has a faster activation and deactivation kinetics (which change on individual EPSPs), apart from slow inactivation, elimination of I_{K-LVA} cannot be replaced by a corresponding leak without affecting the shape of the individual EPSPs and the summation of

EPSPs. Thus, we tested the effect of cumulative decrease in conductance through I_h deactivation on the firing output of MSO neurons in response to realistic patterns of synaptic excitation, we incorporated the relative amplitudes of EPSC trains from a representative cell (Cell 1, 500 Hz condition in Figure 2.8A), and scaled these trains to trigger average firing rates encompassing the dynamic range observed in MSO principal neurons (up to ~200 Hz). To determine how I_h deactivation influences these firing patterns, we compared frequency–intensity (f–I) relationships in normal ACSF (control) vs. in the presence of 50 µM ZD7288. In order to isolate the contribution of the deactivation of I_h from its contribution to resting membrane properties, we used the dynamic clamp technique in the ZD7288 condition to reintroduce a static leak conductance exhibiting a reversal potential of –40 mV ("static g_h", or $g_{h(S)}$). The magnitude of $g_{h(S)}$ was increased until the resting potential, previously hyperpolarized in the presence of ZD7288, was restored to control levels. While this manipulation cannot reproduce the spatial distribution of I_h along the somatodendritic axis, it restored input resistance and membrane time constant near the site of action potential initiation in the axon to near–control values. Thus, we were able to closely match the normal time course of synaptic depolarization as well as the normal firing threshold (Figure 2.12A). Under control and static I_h conditions, 3–5 different 500 Hz patterns of EPSCs were selected from a representative recording (Cell 1 in Figure 2.11A) and injected into MSO neurons recorded in whole–cell current clamp. The magnitude of these trains was scaled to different amplitudes based on the first EPSC, and the range of amplitudes was adjusted to induce average

89

firing rates encompassing a large, physiologically relevant range (up to ~ 200 Hz). The initial 30 ms of responses, prior to substantial I_h deactivation, the 500 Hz train elicited a similar pattern and frequency of action potential firing in control and static g_h conditions. However, over the rest of the 1 second response, when I_h deactivation would be expected to become more significant, the f–I curve was shifted rightward in the static g_h condition, and appeared more non–linear. These results show that the intrinsic gain changes mediated by I_h deactivation helps restore the firing sensitivity of MSO neurons during the progress of synaptic depression at high frequencies.
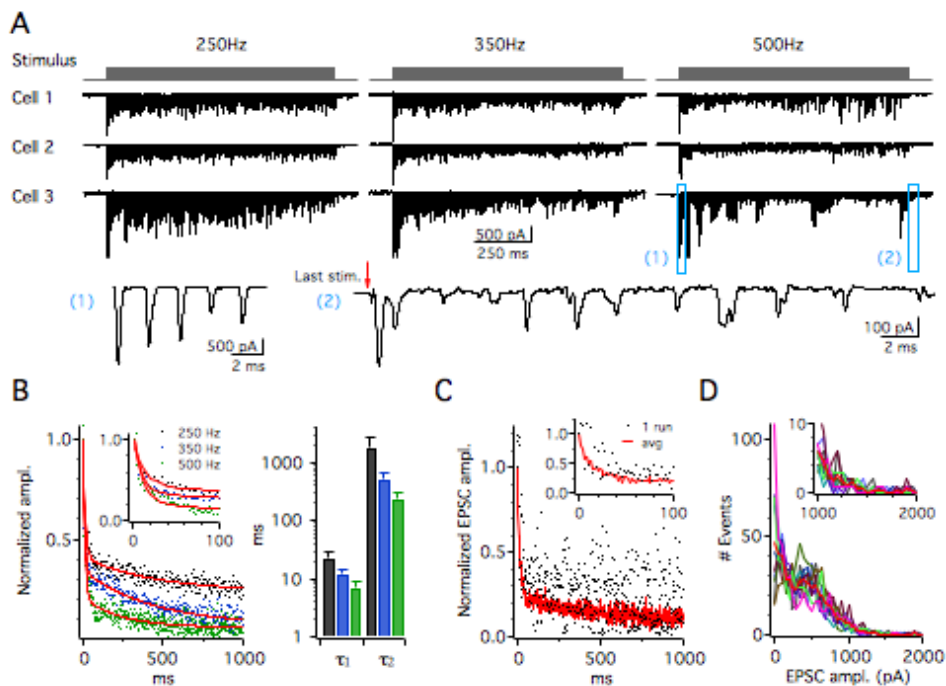
Figure 2.11. Characterization of synaptic depression during at high frequencies in MSO principal neurons. A. Whole cell voltage clamp responses of synaptic currents from three different cells for 250, 350 and 500 Hz trains. During high frequency unilateral stimulation, EPSC responses during trains can reach significant amplitude of the first response, especially following, small amplitude response and failures. Asynchronous responses are apparent towards the end of response (*lower right expanded traces*). B. Average synaptic depression for population. (n=7 for 250 and 350 Hz and n=9 for 500Hz). The average depression varies from 74% to 88% and shows two time constants of decay. C. The response variability of a single synaptic response (cell 1 in A) is contrasted with the average of ten responses (red) to 1 s, 500 Hz synaptic stimulation. The

individual response shows high variability, with many responses far exceeding the average. Synaptic currents are normalized to the first response. D. Frequency distribution of the amplitude of individual events of ten 500 Hz trials in the same experiments as in B (cell 1 in A). Instead of showing a steep decline, most trials had significant events with large amplitudes. Red is the average of all trials.
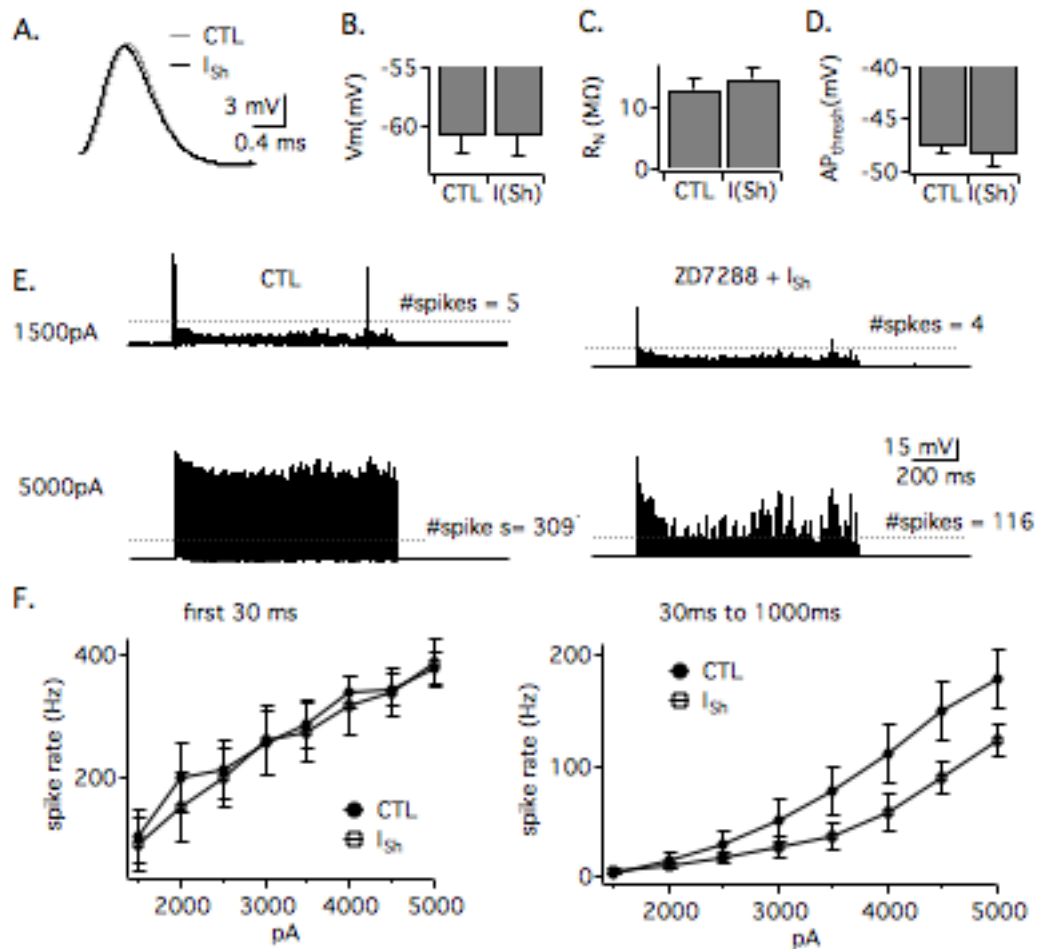
Figure 2.12. Influence of I_h deactivation on action potential firing. A. A realistic pattern of EPSCs was injected into MSO neurons in control conditions and when I_h was blocked by 50 µM ZD7288 and replaced by a static leak conductance with dynamic clamp ("static g_h", or $g_{h(S)}$). The level of $g_{h(S)}$ was adjusted until the amplitude and duration of EPSP responses in ZD7288 matched those in control conditions. B. Group data. The resting potential, input resistance and action potential thresholds in control and ZD7288+ static g_h were similar. C. Responses of an MSO neuron to two different amplitudes of a realistic pattern of EPSCs. For the low amplitude stimulus, the firing rate is similar for control static g_h conditions, while for the higher amplitude stimulus a marked difference in firing rates was apparent in the two conditions. D. Cumulative deactivation of I_h increased firing sensitivity in the face of synaptic depression during long EPSC trains. Group

data, showing the average frequency-intensity curves in control and static g_h conditions. On average the responses in the initial 30 ms of the train are similar in control and static g_h conditions, a time window where synaptic currents are relatively large, and cumulative deactivation of I_h is not significant (n=9). Between 30 and 1000 ms, however, the frequency-intensity curve shifts rightward in the static g_h condition and appears more nonlinear, reflecting the absence of a cumulative, I_h-mediated increase in gain.

DISCUSSION

In MSO principal cells, the encoding of sound–localization cues requires the detection of both the onset and the ongoing temporal registry of binaural synaptic inputs. The central finding of this study is that the dynamical interaction of I_h and $I_{K–LVA}$ is critical for regulating the ongoing component of ITD encoding by MSO. I_h and $I_{K–LVA}$ are crucial for maintaining constant synaptic amplitude over ongoing trains of high–frequency inputs. This interaction of the two conductances also results in accumulation of large conductance changes, in form of increase in input resistance of MSO. The input resistance changes increase linearly with amplitude and frequency and both accumulate and decay over time scales relevant to common auditory stimuli, suggesting a potential role as a history function of preceding auditory stimulus. The cumulative increase in I_h deactivation and $I_{K–LVA}$ inhibition results in counteracting decreasing EPSP amplitude due to synaptic depression.

We show that I_h comprises a major portion of a large resting conductance, depolarizes the resting potential, and establishes a membrane time constant in the sub-millisecond range. We find that $I_{K–LVA}$ has similar effects on the input resistance and membrane time constant, although its contribution to the resting

92

potential is smaller and potentially is counteracted by active transport mechanisms. During trains of excitatory synaptic activity, I_h and I_{K-LVA} undergo a cumulative deactivation and inactivation respectively, decreasing membrane conductance. This does not result in a significant increase in amplitude of EPSPs during trains, due to gradual hyperpolarization of membrane potential during trains. Development of each of the current, I_h deactivation and I_{K-LVA} inactivation, plays an inhibitory influence on each other, thus bringing back the post–stimulus potentials quickly to pre–train values. This interaction also has an additive role in accumulation of input resistance, which manifests after the end of stimulus.

I_h is a major conductance in MSO principal neurons and almost half of it is activated at the resting potential. The role of I_h in setting resting potential and governing input resistance has been demonstrated in numerous other neurons at early stages of auditory processing. These include spiral ganglion cells (Chen, 1997; Mo and Davis, 1997), bushy, stellate, and octopus cells of ventral cochlear nucleus (Bal and Oertel 2000; Cao et al., 2007; Rodrigues and Oertel 2006), neurons in the superior olivary complex (Banks et al., 1993; Cuttle et al., 2001; Leao 2005), transiently firing neurons of the inferior colliculus (Koch and Grothe 2003) and neurons of the nucleus laminaris, the MSO analog in the binaural pathway of birds (Yamada et al., 2005). The steady–state role in setting input resistance and the dynamic role of I_{K-LVA} in enhancing signal–to–noise ratio and phase–locking in the auditory system has been well characterized (Scott et al., 2005; Svirskis et al., 2002). In avian analogous structures, nucleus

magnocellularis and nucleus laminaris, I_{K-LVA} is known to enhance the output of the neurons over long duration stimuli (Slee et al., 2005; Kuznetsova et al., 2008).

Our results show that in MSO both I_h and I_{K-LVA} can be cumulatively deactivated and inactivated, respectively, during high–frequency trains of non–summating excitatory synaptic activity. In brainstem auditory neurons like those in the MSO, such interactions occur cumulatively, because the time course of glutamatergic EPSPs, which is approximately 1–2 ms (Trussell, 1999), is at least an order of magnitude more rapid than the slower time scales of I_h deactivation and I_{K-LVA} inactivation.

A key feature of I_h in MSO principal neurons is its relatively negative reversal potential, which ranged from –34 to –43 mV (average –40.1 mV). The voltage proximity of near–threshold EPSP trains to the reversal potential of I_h (and thus a reduction in driving force on permeant cations) results in a smaller hyperpolarization, than would have resulted in the case of conventional reversal of I_h. However this hyperpolarization is counterbalanced to an extent by I_{K-LVA} inactivation, which results in a hasty return of the post–stimulus membrane potential to pre–train values. During the trains, apart from I_h deactivation, I_{K-LVA} activation provides a hyperpolarizing influence, thus resulting in relatively stable MSO output, despite increases in input resistance. The low input resistance of

the cell itself is an equally important factor preventing huge changes in the post–stimulus potentials.

Thus, unlike avian system where one conductance dominates changes in input resistance, in mammals an interplay of I_{K-LVA} and I_h regulates a near constant output of MSO, also forcing a quick return of cells to an optimal membrane potential, situated in the activation ranges of I_h and I_{K-LVA}. Even though a stable output can be achieved, if one replaces I_{K-LVA} and I_h with leak, this situation would render the system incapable of active pruning of EPSPs enabled by I_{K-LVA} and moreover will not result in generation of a post–stimulus increase in input resistance.

Cumulative I_{K-LVA} inactivation and I_h deactivation results in an increased sensitivity of MSO neurons after the stimulus. These changes in input resistance accumulate on the time scales of physiologically relevant auditory stimuli and decay on the same time scales, suggesting a potential role in encoding a history function of stimulation. This change in input resistance increases linearly with frequency and amplitude and has contributions from both I_h deactivation and I_{K-LVA} inactivation. Abstract models of sound encoding have pointed to duration selectivity of neurons evolving from the combination of slow conductances (Hooper et al., 2002) and these slow changes in input resistance can be an interesting underlying substrate for these changes in many auditory neurons. Nonetheless even at the level of MSO, generation of history function of sound

stimulus can be an underlying mechanism for gap detection and increased resolution of clicks; information which can be inherited by higher centers.

The excitatory inputs from bushy cells of the cochlear nucleus to MSO principal neurons *in vivo* can deliver entrained, excitatory inputs up to ~600 Hz, and phase–locking of individual axons within the larger MSO input population can extend up to approximately 2–3 kHz depending on the species. Thus, the current cumulative changes are likely an under–estimate of *in vivo* increase in input resistance. How does the MSO response appear, in the wake of synaptic depression and how the balance of the two conductances plays out for a depressing train of stimuli is going to be next step in the field towards understanding of encoding of ongoing inter–aural sound disparity. Many synaptic inputs can reach far higher amplitudes in dendrites than in soma. Whether real synaptic responses trigger increased deactivation of I_h, as compared to somatic current injections that result in increased input resistance changes, yet remains to seen. Also, what role does the dynamics of inhibitory inputs plays must await further information on synaptic depression of inhibition and in vivo activity patterns. Added information about spatial distribution of the two conductances might change nuances of the interaction, nonetheless our current study demonstrates a pivotal role of the interplay of $I_{K–LVA}$ and I_h in regulating a constant output of MSO, while generating a history function of auditory activity.

Chapter 5

DISCUSSION

The central finding presented in this thesis has been that I_h plays an important role in regulating the responses of the MSO neurons. I find that I_h, which acquires its unique properties during postnatal development, is a key regulator of the MSO coincidence window. During long trains of input to the cell, in conjunction with I_{K-LVA}, I_h dynamically regulates the responses of MSO neurons. This dynamic interaction of I_h and I_{K-LVA} results in a near–constant response for equal–amplitude inputs, a hasty return of MSO to resting potential after the cessation of inputs and accumulation of input resistance by MSO neurons to trains of depolarizing inputs.

Development of I_h in MSO and it's physiological consequences

In chapter 3, I describe that I_h is one of the major determinants of MSO neuron properties, transforming it from a slow "conventional" neuron to a brief sub-millisecond processing neuron. This is accomplished by two changes: increase in conductance over age and modulation of *VAC* of HCN channels. Even when normalized for the decrease in membrane area of MSO neurons, the G_h density increases with age. Because we did not conduct single–channel analysis (which is very difficult, given the small conductance of the HCN channels), we cannot

distinguish between an increase in numbers of channels and increase in single–channel conductance. However a parsimonious explanation would be an insertion of more channels in the membrane.

To the best of our knowledge, the developmental shift in *VAC* of +30mV is the largest reported for any voltage–gated ion channel over postnatal development. We show that this shift in the *VAC* functionally corresponds into making the MSO membrane time constants briefer and hence a temporally small synaptic coincidence window.

Mechanisms underlying changes of HCN properties

We observe a developmental reduction in cAMP sensitivity of I_h in MSO. The most parsimonious explanation for the decrease in cAMP and the hastening of I_h kinetics is a change in HCN subunits. One would expect HCN to be dominated by HCN2 and HCN4 before hearing onset and by HCN1 after hearing onset (see Figure 2.2). Nonetheless, given the absence of good immuno-cytochemistry data from gerbil MSO, that explanation is not the only one. Given that we find that a few signaling pathways, namely PIP_2 and P38MAPK can change *VAC* of I_h in mature MSO, it is entirely possible that the changes in HCN properties are mediated by biochemical signaling. Nucleated patch experiments (data not presented) in mature MSO neurons exhibit HCN properties akin to the young

MSO cells, supporting the idea of a biochemical regulation of HCN channels to adult like phenotype.

In recent years different splice variants of Trip8b have been shown to modulate HCN properties in a manner such that changes in the I_h of MSO can be accounted for by expression of Trip8b auxiliary subunit (Santoro et al., 2004; Lewis et al., 2009; Santoro et al., 2009; Zolles et al., 2009; Lipscombe and Pan, 2009). Our next step is going to focus on understanding the HCN subunit composition in MSO and potential role of auxiliary subunits in regulating its properties.

Dynamical interaction of I_h and I_{K-LVA}

The study of dynamical interaction of I_h and I_{K-LVA} has succeeded at two fronts: (1) it is the first study to explore the responses of MSO to trains of stimuli, thus taking a step beyond current explorations, all of which have been limited to exploration of single stimulus; (2) it is one of the few studies in the auditory system to concomitantly look at the roles of multiple channels dictating properties of a neuron.

In chapter 4 we find that dynamical interactions of I_h and I_{K-LVA} are critical for regulating the ITD encoding by MSO. I_h and I_{K-LVA} are crucial in maintaining constant responses to ongoing trains of high–frequency inputs. This interaction of

the two conductances also results in accumulation of large conductance changes in the form of increase in input resistance of MSO. The input resistance changes increase linearly with amplitude and frequency of input stimulus train, accumulate and decay over time scales relevant to most auditory stimuli, suggesting a potential role as a history function of preceding auditory stimulus.

The limitations of the current study have been (1) Use of very artificial uniform amplitude stimuli and thus lack of direct understanding of MSO neuron properties to realistic stimuli; (2) inability to dissect out the functional consequence of an increase in the input resistance. It is unclear whether input resistance increase, which will mean broader coincidence window, is a boon as a "history function", or a constraint of evolutionary tinkering in optimizing the output of MSO. Though evolutionary questions may have to stay unanswered for a bit, in collaboration with Prof. Nace Golding, Dr. Michiel Remme and Prof. John Rinzel, I expect to be able to explore the role of the dynamical interaction of two ion channels in context of physiological inputs to MSO.

The excitatory inputs from bushy cells of the cochlear nucleus to MSO principal neurons *in vivo* can deliver entrained, excitatory inputs up to ~600 Hz, and phase locking of individual axons within the larger MSO input population can extend up to approximately 2-3 kHz depending on the species. Since MSO receive broadband inputs, the current cumulative changes of I_h and $I_{K\text{-}LVA}$ interaction are likely an under-estimate of *in vivo* increase in the input resistance. How the MSO

responses appear in wake of synaptic depression and how the balance of the two conductances plays out for a depressing train of stimuli is the next step in understanding the of encoding of ongoing inter-aural time differences. Many synaptic inputs can reach far higher amplitudes in dendrites than in soma. Whether real synaptic responses can trigger an increased deactivation of I_h as compared to somatic current injections, resulting in increased input resistance changes, remains to be seen. Also, what role the dynamics of inhibitory inputs plays must await further information on synaptic depression of inhibition and *in vivo* activity patterns. Added information about the spatial distribution of I_h is going to be necessary towards a more complete understanding of the responses of MSO.

EPILOGUE

Most, though not all animal studies, where brainstem neurophysiological recordings have been made, are still plagued by the use of tonal stimuli and the use of either only onset or ongoing temporal disparity, leaving much room for exploration and improvement in this area.

Gerbils have a larger MSO than other rodents. They have a well-developed low–frequency hearing, somewhat comparable to humans. Gerbils are also known to employ ITD to localize sound sources. Given the above-mentioned reasons gerbils have been the choice of animal system to study MSO physiology. MSO is known to have different properties in different animals, even to project bilaterally in moles, many bats, and opossums (Oertel, 1999). MSO might also be playing additional roles in different mammals, something a model system driven research tends to ignore. This current trend in biomedical research occasionally leads to overreaching in generic interpretations, sometimes extending findings to human physiology without adequate factual backing. Thus with the current lack of extensive data from evolutionary proximate primate preparations, caution should be observed in extending the validity of results obtained from gerbils to human hearing. An appreciation of differences in the inter-aural phase and timing disparity cues being used somewhat differently in animals with different head sizes will be prudent. It is entirely likely that the MSO in small-headed animals is playing somewhat different roles than in large-headed animals.

Slice physiology has both advantages and limitations. The advantages of slice physiology are easy access of tissue for electrophysiological analysis, control over stimulus, pharmacological dissection of mechanisms. MSO preparation offers additional advantage of the proximity to sensory inputs. In future studies it will be important to try to bridge the gap between psychophysics and cellular physiology. Also, MSO can be reasonably speculated to be involved in many other auditory timing processes like echo suppression, gap detection, certain aspects of precedence effects and potentially speech recognition. I hope that apart from the advances in cellular physiology of MSO, a comprehensive *in vivo* exploration of MSO functions will be underway in near future. Most importantly, many models of ITD encoding arising out of slice physiology and computational and theoretical exploration are only nice ideas until an *in vivo* research validates or disproves them. Thus, I hope that future research in MSO slice physiology will evolve more integrative exploration of cellular properties and circuitry to construct models of ITD detection and that the *in vivo* research will put those models through a litmus test.

GLOSSARY

ACSF	artificial cerebrospinal fluid
AHP	after-hyperpolarization
AN	auditory nerve
AP	action potential
AVCN	anterior ventral cochlear nucleus
CA1	*Cornu Ammonis* 1
CA3	*Cornu Ammonis* 3
cAMP	cyclic adenosine monophosphate
CNBD	cyclic-nucleotide-binding domain
CNS	central nervous system
DNLL	dorsal nucleus of lateral lemniscus
EPSC	excitatory post–synaptic currents
EPSP	excitatory post–synaptic potential
g/G	conductance
HCN	Hyperpolarization-activated, Cyclic Nucleotide–sensitive, Cation Non-selective channels
Hearing onset	time of clearance of auditory canal, ~ PND 12
I	current
IC	inferior colliculus
I_h	hyperpolarization activated cyclic nucleotide gated current
$I_{K\text{-}LVA}$	low-voltage-activated potassium current
ILD	inter-aural level disparity
IPSP	inhibitory post–synaptic potential
IPI	inter pulse interval
ISI	inter spike interval
ITD	Interaural time disparity
k	slope of the Boltzmann fit to the VAC
LSO	lateral superior olive
MiRP1	MinK-related protein, an accessory protein interacting with HCN channels
MSO	medial superior olive
MNTB	Medial nucleus of the trapezoid body
PIP_2	phosophatidylinositol-4,5-bisphosphate
PND	post-natal day, with day of birth counted as PND 0
SBC	spherical bushy cells
Trip8b	tetratricopeptide-repeat containing Rab8b-interacting protein, an accessory protein interacting with HCN channels
$V_{1/2}$	voltage of half activation of channels obtained by the Boltzmann fit to the VAC
VAC	voltage activation curve
V_{aft}	after–train hyperpolarization

BIBLIOGRAPHY

Abbott, G.W., Sesti, F., Splawski, I., Buck, M.E., Lehmann, M.H., Timothy, K.W., Keating, M.T., and Goldstein, S.A. (1999). MiRP1 forms IKr potassium channels with HERG and is associated with cardiac arrhythmia. Cell *97*, 175-187.

Agmon-Snir, H., Carr, C.E., and Rinzel, J. (1998). The role of dendrites in auditory coincidence detection. Nature *393*, 268-272.

Altomare, C., Terragni, B., Brioschi, C., Milanesi, R., Pagliuca, C., Viscomi, C., Moroni, A., Baruscotti, M., and DiFrancesco, D. (2003). Heteromeric HCN1-HCN4 channels: a comparison with native pacemaker channels from the rabbit sinoatrial node. J Physiol *549*, 347-359.

Bal, R., and Oertel, D. (2000). Hyperpolarization-activated, mixed-cation current (I(h)) in octopus cells of the mammalian cochlear nucleus. J Neurophysiol *84*, 806-817.

Bal, R., and Oertel, D. (2001). Potassium currents in octopus cells of the mammalian cochlear nucleus. J Neurophysiol *86*, 2299-2311.

Banks, M.I., Pearce, R.A., and Smith, P.H. (1993). Hyperpolarization-activated cation current (Ih) in neurons of the medial nucleus of the trapezoid body: voltage-clamp analysis and enhancement by norepinephrine and cAMP suggest a modulatory mechanism in the auditory brain stem. J Neurophysiol *70*, 1420-432.

Barbuti, A., Baruscotti, M., and DiFrancesco, D. (2007). The pacemaker current: from basics to the clinics. J Cardiovasc Electrophysiol *18*, 342-47.

Barbuti, A., Gravante, B., Riolfo, M., Milanesi, R., Terragni, B., and DiFrancesco, D. (2004). Localization of pacemaker channels in lipid rafts regulates channel kinetics. Circ Res *94*, 1325-331.

Beaumont, V., and Zucker, R.S. (2000). Enhancement of synaptic transmission by cyclic AMP modulation of presynaptic Ih channels. Nat Neurosci *3*, 133-141.

Beaumont, V., Zhong, N., Froemke, R.C., Ball, R.W., and Zucker, R.S. (2002). Temporal synaptic tagging by I(h) activation and actin: involvement in long-term facilitation and cAMP-induced synaptic enhancement. Neuron *33*, 601-613.

Becker, M., Nothwang, H.G., and Friauf, E. (2003). Differential expression pattern of chloride transporters NCC, NKCC2, KCC1, KCC3, KCC4, and AE3 in the developing rat auditory brainstem. Cell Tissue Res *312*, 155-165.

Beckius, G.E., Batra, R., and Oliver, D.L. (1999). Axons from anteroventral cochlear nucleus that terminate in medial superior olive of cat: observations related to delay lines. J Neurosci *19*, 3146-161.

Brand, A., Behrend, O., Marquardt, T., McAlpine, D., and Grothe, B. (2002). Precise inhibition is essential for microsecond interaural time difference coding. Nature *417*, 543-47.

Brewster, A.L., Chen, Y., Bender, R.A., Yeh, A., Shigemoto, R., and Baram, T.Z. (2007). Quantitative analysis and subcellular distribution of mRNA and protein

expression of the hyperpolarization-activated cyclic nucleotide-gated channels throughout development in rat hippocampus. Cereb Cortex *17*, 702-712.

Caicedo, A., and Eybalin, M. (1999). Glutamate receptor phenotypes in the auditory brainstem and mid-brain of the developing rat. Eur J Neurosci *11*, 51-74.

Cao, X.J., Shatadal, S., and Oertel, D. (2007). Voltage-sensitive conductances of bushy cells of the Mammalian ventral cochlear nucleus. J Neurophysiol *97*, 3961-975.

Carr, C.E., and Konishi, M. (1988). Axonal delay lines for time measurement in the owl's brainstem. Proc Natl Acad Sci U S A *85*, 8311-15.

Carr, C.E., and Konishi, M. (1990). A circuit for detection of interaural time differences in the brain stem of the barn owl. J Neurosci *10*, 3227-246.

Chen, C. (1997). Hyperpolarization-activated current (Ih) in primary auditory neurons. Hear Res *110*, 179-190.

Cherry, E.C. (1953). Some experiments on the recognition of speech, with one and with two ears. Journal of the Acoustical Society of America *25*, 975-79.

Chirila, F.V., Rowland, K.C., Thompson, J.M., and Spirou, G.A. (2007). Development of gerbil medial superior olive: integration of temporally delayed excitation and inhibition at physiological temperature. J Physiol *584*, 167-190.

Cuttle, M.F., Rusznák, Z., Wong, A.Y., Owens, S., and Forsythe, I.D. (2001). Modulation of a presynaptic hyperpolarization-activated cationic current (I(h)) at an excitatory synaptic terminal in the rat auditory brainstem. J Physiol *534*, 733-744.

Day, M.L., Doiron, B., and Rinzel, J. (2008). Subthreshold K+ channel dynamics interact with stimulus spectrum to influence temporal coding in an auditory brain stem model. J Neurophysiol *99*, 534-544.

Decher, N., Bundis, F., Vajna, R., and Steinmeyer, K. (2003). KCNE2 modulates current amplitudes and activation kinetics of HCN4: influence of KCNE family members on HCN4 currents. Pflugers Arch *446*, 633-640.

DiFrancesco, D. (1981). A new interpretation of the pace-maker current in calf Purkinje fibres. J Physiol *314*, 359-376.

DiFrancesco, D. (1981). A study of the ionic nature of the pace-maker current in calf Purkinje fibres. J Physiol *314*, 377-393.

DiFrancesco, D. (1984). Characterization of the pace-maker current kinetics in calf Purkinje fibres. J Physiol *348*, 341-367.

DiFrancesco, D. (1984). Properties of the cardiac pacemaker (if) current. Boll Soc Ital Biol Sper *60 Suppl 4*, 29-33.

DiFrancesco, D. (1986). Characterization of single pacemaker channels in cardiac sino-atrial node cells. Nature *324*, 470-73.

DiFrancesco, D., and Mangoni, M. (1994). Modulation of single hyperpolarization-activated channels (i(f)) by cAMP in the rabbit sino-atrial node. J Physiol *474*, 473-482.

Fischer, B.J., and Peña, J.L. (2009). Bilateral matching of frequency tuning in neural cross-correlators of the owl. Biol Cybern *100*, 521-531.

Forsythe, I.D., and Barnes-Davies, M. (1993). The binaural auditory pathway: membrane currents limiting multiple action potential generation in the rat medial nucleus of the trapezoid body. Proc Biol Sci *251*, 143-150.

George, M.S., Abbott, L.F., and Siegelbaum, S.A. (2009). HCN hyperpolarization-activated cation channels inhibit EPSPs by interactions with M-type K(+) channels. Nat Neurosci *12*, 577-584.

Gisselmann, G., Gamerschlag, B., Sonnenfeld, R., Marx, T., Neuhaus, E.M., Wetzel, C.H., and Hatt, H. (2005). Variants of the Drosophila melanogaster Ih-channel are generated by different splicing. Insect Biochem Mol Biol *35*, 505-514.

Goldberg, J.M., and Brown, P.B. (1969). Response of binaural neurons of dog superior olivary complex to dichotic tonal stimuli: some physiological mechanisms of sound localization. J Neurophysiol *32*, 613-636.

Golding, N.L., Ferragamo, M.J., and Oertel, D. (1999). Role of intrinsic conductances underlying responses to transients in octopus cells of the cochlear nucleus. J Neurosci *19*, 2897-2905.

Golding, N.L., Robertson, D., and Oertel, D. (1995). Recordings from slices indicate that octopus cells of the cochlear nucleus detect coincident firing of auditory nerve fibers with temporal precision. J Neurosci *15*, 3138-153.

Gravante, B., Barbuti, A., Milanesi, R., Zappi, I., Viscomi, C., and DiFrancesco, D. (2004). Interaction of the pacemaker channel HCN1 with filamin A. J Biol Chem *279*, 43847-853.

Grothe, B. (2003). New roles for synaptic inhibition in sound localization. Nat Rev Neurosci *4*, 540-550.

Hagiwara, N., and Irisawa, H. (1989). Modulation by intracellular Ca2+ of the hyperpolarization-activated inward current in rabbit single sino-atrial node cells. J Physiol *409*, 121-141.

Hancock, K.E., and Delgutte, B. (2004). A physiologically based model of interaural time difference discrimination. J Neurosci *24*, 7110-17.

Hassfurth, B., Magnusson, A.K., Grothe, B., and Koch, U. (2009). Sensory deprivation regulates the development of the hyperpolarization-activated current in auditory brainstem neurons. Eur J Neurosci *30*, 1227-238.

Henkel, C.K., and Spangler, K.M. (1983). Organization of the efferent projections of the medial superior olivary nucleus in the cat as revealed by HRP and autoradiographic tracing methods. J Comp Neurol *221*, 416-428.

Henning, G.B. (1974). Lateralization and the binaural masking-level difference. J Acoust Soc Am *55*, 1259-262.

Herrmann, S., Stieber, J., and Ludwig, A. (2007). Pathophysiology of HCN channels. Pflugers Arch *454*, 517-522.

Herrmann, S., Stieber, J., Stöckl, G., Hofmann, F., and Ludwig, A. (2007). HCN4 provides a 'depolarization reserve' and is not required for heart rate acceleration in mice. EMBO J *26*, 4423-432.

Hogg, R.C., Harper, A.A., and Adams, D.J. (2001). Developmental changes in hyperpolarization-activated currents I(h) and I(K(IR)) in isolated rat intracardiac neurons. J Neurophysiol *86*, 312-320.

Hooper, S.L., Buchman, E., and Hobbs, K.H. (2002). A computational role for slow conductances: single-neuron models that measure duration. Nat Neurosci *5*, 552-56.

Hughes, J.W. (1940). The Upper Frequency Limit for the Binaural Localization of a Pure Tone by Phase Difference. Proceedings of the Royal Society of London. Series B, Biological Sciences *128*, 293-305.

Jeffress, L.A. (1948). A place theory of sound localization. J Comp Physiol Psychol *41*, 35-39.

Jones, G.L., and Litovsky, R.Y. (2008). Role of masker predictability in the cocktail party problem. J Acoust Soc Am *124*, 3818-830.

Joris, P., and Yin, T.C. (2007). A matter of time: internal delays in binaural processing. Trends Neurosci *30*, 70-78.

Joris, P.X., and Yin, T.C. (1998). Envelope coding in the lateral superior olive. III. Comparison with afferent pathways. J Neurophysiol *79*, 253-269.

Joris, P.X., Carney, L.H., Smith, P.H., and Yin, T.C. (1994). Enhancement of neural synchronization in the anteroventral cochlear nucleus. I. Responses to tones at the characteristic frequency. J Neurophysiol *71*, 1022-036.

Joris, P.X., Van de Sande, B., Louage, D.H., and van der Heijden, M. (2006). Binaural and cochlear disparities. Proc Natl Acad Sci U S A *103*, 12917-922.

Kimura, K., Kitano, J., Nakajima, Y., and Nakanishi, S. (2004). Hyperpolarization-activated, cyclic nucleotide-gated HCN2 cation channel forms a protein assembly with multiple neuronal scaffold proteins in distinct modes of protein-protein interaction. Genes Cells *9*, 631-640.

Kitzes, L.M., Kageyama, G.H., Semple, M.N., and Kil, J. (1995). Development of ectopic projections from the ventral cochlear nucleus to the superior olivary complex induced by neonatal ablation of the contralateral cochlea. J Comp Neurol *353*, 341-363.

Koch, U., Braun, M., Kapfer, C., and Grothe, B. (2004). Distribution of HCN1 and HCN2 in rat auditory brainstem nuclei. Eur J Neurosci *20*, 79-91.

Koch, U., and Grothe, B. (2003). Hyperpolarization-activated current (Ih) in the inferior colliculus: distribution and contribution to temporal processing. J Neurophysiol *90*, 3679-687.

Kole, M.H., Hallermann, S., and Stuart, G.J. (2006). Single Ih channels in pyramidal neuron dendrites: properties, distribution, and impact on action potential output. J Neurosci *26*, 1677-687.

Kuba, H., Koyano, K., and Ohmori, H. (2002). Development of membrane conductance improves coincidence detection in the nucleus laminaris of the chicken. J Physiol *540*, 529-542.

Kuba, H., Yamada, R., Fukui, I., and Ohmori, H. (2005). Tonotopic specialization of auditory coincidence detection in nucleus laminaris of the chick. J Neurosci *25*, 1924-934.

Kullmann, P.H., and Kandler, K. (2001). Glycinergic/GABAergic synapses in the lateral superior olive are excitatory in neonatal C57Bl/6J mice. Brain Res Dev Brain Res *131*, 143-47.

Kuyper, P. (1972). The cocktail party effect. Audiology *11*, 277-282.

Kuznetsova, M.S., Higgs, M.H., and Spain, W.J. (2008). Adaptation of firing rate and spike-timing precision in the avian cochlear nucleus. J Neurosci *28*, 11906-915.

Leao, R.N., Svahn, K., Berntson, A., and Walmsley, B. (2005). Hyperpolarization-activated (I) currents in auditory brainstem neurons of normal and congenitally deaf mice. Eur J Neurosci *22*, 147-157.

Lewis, A.S., Schwartz, E., Chan, C.S., Noam, Y., Shin, M., Wadman, W.J., Surmeier, D.J., Baram, T.Z., Macdonald, R.L., and Chetkovich, D.M. (2009). Alternatively spliced isoforms of TRIP8b differentially control h channel trafficking and function. J Neurosci *29*, 6250-265.

Li, C.H., Zhang, Q., Teng, B., Mustafa, S.J., Huang, J.Y., and Yu, H.G. (2008). Src tyrosine kinase alters gating of hyperpolarization-activated HCN4 pacemaker channel through Tyr531. Am J Physiol Cell Physiol *294*, C355-362.

Lipscombe, D., and Pan, J.Q. (2009). Tripping the HCN breaker. Neuron *62*, 747-750.

Ludwig, A., Zong, X., Jeglitsch, M., Hofmann, F., and Biel, M. (1998). A family of hyperpolarization-activated mammalian cation channels. Nature *393*, 587-591.

Maccaferri, G., and McBain, C.J. (1996). The hyperpolarization-activated current (Ih) and its contribution to pacemaker activity in rat CA1 hippocampal stratum oriens-alveus interneurones. J Physiol *497 (Pt 1)*, 119-130.

MacLean, J.N., Zhang, Y., Goeritz, M.L., Casey, R., Oliva, R., Guckenheimer, J., and Harris-Warrick, R.M. (2005). Activity-independent coregulation of IA and Ih in rhythmically active neurons. J Neurophysiol *94*, 3601-617.

Magee, J.C. (1998). Dendritic hyperpolarization-activated currents modify the integrative properties of hippocampal CA1 pyramidal neurons. J Neurosci *18*, 7613-624.

Magee, J.C. (1999). Dendritic Ih normalizes temporal summation in hippocampal CA1 neurons . Nat Neurosci *2*, 848.

Magnusson, A.K., Kapfer, C., Grothe, B., and Koch, U. (2005). Maturation of glycinergic inhibition in the gerbil medial superior olive after hearing onset. J Physiol *568*, 497-512.

McAlpine, D., and Palmer, A.R. (2002). Blocking GABAergic inhibition increases sensitivity to sound motion cues in the inferior colliculus. J Neurosci *22*, 1443-453.

McAlpine, D., Jiang, D., and Palmer, A.R. (2001). A neural code for low-frequency sound localization in mammals. Nat Neurosci *4*, 396-401.

McFadden, D., and Pasanen, E.G. (1975). Binaural beats at high frequencies. Science *190*, 394-96.

McFadden, D., and Pasanen, E.G. (1976). Lateralization of high frequencies based on interaural time differences. J Acoust Soc Am *59*, 634-39.

Michels, G., Brandt, M.C., Zagidullin, N., Khan, I.F., Larbig, R., van Aaken, S., Wippermann, J., and Hoppe, U.C. (2008). Direct evidence for calcium conductance of hyperpolarization-activated cyclic nucleotide-gated channels and human native If at physiological calcium concentrations. Cardiovasc Res *78*, 466-475.

Michels, G., Er, F., Khan, I., Südkamp, M., Herzig, S., and Hoppe, U.C. (2005). Single-channel properties support a potential contribution of hyperpolarization-activated cyclic nucleotide-gated channels and If to cardiac arrhythmias. Circulation *111*, 399-404.

Michels, G., Er, F., Khan, I.F., Endres-Becker, J., Brandt, M.C., Gassanov, N., Johns, D.C., and Hoppe, U.C. (2008). K+ channel regulator KCR1 suppresses heart rhythm by modulating the pacemaker current If. PLoS One *3*, e1511.

Mistrík, P., Pfeifer, A., and Biel, M. (2006). The enhancement of HCN channel instantaneous current facilitated by slow deactivation is regulated by intracellular chloride concentration. Pflugers Arch *452*, 718-727.

Mo, Z.L., and Davis, R.L. (1997). Heterogeneous voltage dependence of inward rectifier currents in spiral ganglion neurons. J Neurophysiol *78*, 3019-027.

Moore, J.K., Ponton, C.W., Eggermont, J.J., Wu, B.J., and Huang, J.Q. (1996). Perinatal maturation of the auditory brain stem response: changes in path length and conduction velocity. Ear Hear *17*, 411-18.

Moosmang, S., Biel, M., Hofmann, F., and Ludwig, A. (1999). Differential distribution of four hyperpolarization-activated cation channels in mouse brain. Biol Chem *380*, 975-980.

Morest, D.K. (1968). The collateral system of the medial nucleus of the trapezoid body of the cat, its neuronal architecture and relation to the olivo-cochlear bundle. Brain Res *9*, 288-311.

Moushegian, G., Rupert, A.L., and Langford, T.L. (1967). Stimulus coding by medial superior olivary neurons. J Neurophysiol *30*, 1239-261.

Much, B., Wahl-Schott, C., Zong, X., Schneider, A., Baumann, L., Moosmang, S., Ludwig, A., and Biel, M. (2003). Role of subunit heteromerization and N-linked glycosylation in the formation of functional hyperpolarization-activated cyclic nucleotide-gated channels. J Biol Chem *278*, 43781-86.

Munsch, T., and Pape, H.C. (1999). Modulation of the hyperpolarization-activated cation current of rat thalamic relay neurones by intracellular pH. J Physiol *519 Pt 2*, 493-504.

Narayanan, R., and Johnston, D. (2007). Long-term potentiation in rat hippocampal neurons is accompanied by spatially widespread changes in intrinsic oscillatory dynamics and excitability. Neuron *56*, 1061-075.

Narayanan, R., and Johnston, D. (2008). The h channel mediates location dependence and plasticity of intrinsic phase response in rat hippocampal neurons. J Neurosci *28*, 5846-860.

Nolan, M.F., Malleret, G., Dudman, J.T., Buhl, D.L., Santoro, B., Gibbs, E., Vronskaya, S., Buzsáki, G., Siegelbaum, S.A., et al. (2004). A behavioral role for dendritic integration: HCN1 channels constrain spatial memory and plasticity at inputs to distal dendrites of CA1 pyramidal neurons. Cell *119*, 719-732.

Nolan, M.F., Malleret, G., Lee, K.H., Gibbs, E., Dudman, J.T., Santoro, B., Yin, D., Thompson, R.F., Siegelbaum, S.A., et al. (2003). The hyperpolarization-activated HCN1 channel is important for motor learning and neuronal integration by cerebellar Purkinje cells. Cell *115*, 551-564.

Notomi, T., and Shigemoto, R. (2004). Immunohistochemical localization of Ih channel subunits, HCN1-4, in the rat brain. J Comp Neurol *471*, 241-276.

Oertel, D. (1997). Encoding of timing in the brain stem auditory nuclei of vertebrates. Neuron *19*, 959-962.

Oertel, D. (1999). The role of timing in the brain stem auditory nuclei of vertebrates. Annu Rev Physiol *61*, 497-519.

Oertel, D., Shatadal, S., and Cao, X.J. (2008). In the ventral cochlear nucleus Kv1.1 and subunits of HCN1 are colocalized at surfaces of neurons that have low-voltage-activated and hyperpolarization-activated conductances. Neuroscience *154*, 77-86.

Okoyama, S., Moriizumi, T., Kitao, Y., Kawano, J., and Kudo, M. (1995). Postnatal development of the projection from the medial superior olive to the inferior colliculus in the rat. Hear Res *88*, 65-70.

Ouyang, Q., Goeritz, M., and Harris-Warrick, R.M. (2007). Panulirus interruptus Ih-channel gene PIIH: modification of channel properties by alternative splicing and role in rhythmic activity. J Neurophysiol *97*, 3880-892.

Pape, H.C. (1996). Queer current and pacemaker: the hyperpolarization-activated cation current in neurons. Annu Rev Physiol *58*, 299-327.

Pecka, M., Brand, A., Behrend, O., and Grothe, B. (2008). Interaural time difference processing in the mammalian medial superior olive: the role of glycinergic inhibition. J Neurosci *28*, 6914-925.

Pian, P., Bucchi, A., Robinson, R.B., and Siegelbaum, S.A. (2006). Regulation of gating and rundown of HCN hyperpolarization-activated channels by exogenous and endogenous PIP2. J Gen Physiol *128*, 593-604.

Pickles, J.O. (2008). An introduction to the physiology of hearing (Bingley, UK: Emerald).

Poolos, N.P., Bullis, J.B., and Roth, M.K. (2006). Modulation of h-channels in hippocampal pyramidal neurons by p38 mitogen-activated protein kinase. J Neurosci *26*, 7995-8003.

Pyott, S.J., Meredith, A.L., Fodor, A.A., Vázquez, A.E., Yamoah, E.N., and Aldrich, R.W. (2007). Cochlear function in mice lacking the BK channel alpha, beta1, or beta4 subunits. J Biol Chem *282*, 3312-324.

Qu, J., Kryukova, Y., Potapova, I.A., Doronin, S.V., Larsen, M., Krishnamurthy, G., Cohen, I.S., and Robinson, R.B. (2004). MiRP1 modulates HCN2 channel expression and gating in cardiac myocytes. J Biol Chem *279*, 43497-3502.

Rautenberg, P.L., Grothe, B., and Felmy, F. (2009). Quantification of the three-dimensional morphology of coincidence detector neurons in the medial superior olive of gerbils during late postnatal development. J Comp Neurol *517*, 385-396.

Rayleigh, J.W.S. (1877). The theory of sound (London,:

Rayleigh, J.W.S. (1937). The theory of sound (London,:

Reyes, A.D., Rubel, E.W., and Spain, W.J. (1994). Membrane properties underlying the firing of neurons in the avian cochlear nucleus. J Neurosci *14*, 5352-364.

Robinson, R.B., and Siegelbaum, S.A. (2003). Hyperpolarization-activated cation currents: from molecules to physiological function. Annu Rev Physiol *65*, 453-480.

Rodrigues, A.R., and Oertel, D. (2006). Hyperpolarization-activated currents regulate excitability in stellate cells of the mammalian ventral cochlear nucleus. J Neurophysiol *95*, 76-87.

Rothman, J.S., and Manis, P.B. (2003). Kinetic analyses of three distinct potassium conductances in ventral cochlear nucleus neurons. J Neurophysiol *89*, 3083-096.

Rothman, J.S., and Manis, P.B. (2003). The roles potassium currents play in regulating the electrical activity of ventral cochlear nucleus neurons. J Neurophysiol *89*, 3097-3113.

Russell, F.A., and Moore, D.R. (1999). Effects of unilateral cochlear removal on dendrites in the gerbil medial superior olivary nucleus. Eur J Neurosci *11*, 1379-390.

Sanes, D.H., and Takács, C. (1993). Activity-dependent refinement of inhibitory connections. Eur J Neurosci *5*, 570-74.

Santoro, B., and Tibbs, G.R. (1999). The HCN gene family: molecular basis of the hyperpolarization-activated pacemaker channels. Ann N Y Acad Sci *868*, 741-764.

Santoro, B., Chen, S., Luthi, A., Pavlidis, P., Shumyatsky, G.P., Tibbs, G.R., and Siegelbaum, S.A. (2000). Molecular and functional heterogeneity of hyperpolarization-activated pacemaker channels in the mouse CNS. J Neurosci *20*, 5264-275.

Santoro, B., Grant, S.G., Bartsch, D., and Kandel, E.R. (1997). Interactive cloning with the SH3 domain of N-src identifies a new brain specific ion channel protein, with homology to eag and cyclic nucleotide-gated channels. Proc Natl Acad Sci U S A *94*, 14815-820.

Santoro, B., Liu, D.T., Yao, H., Bartsch, D., Kandel, E.R., Siegelbaum, S.A., and Tibbs, G.R. (1998). Identification of a gene encoding a hyperpolarization-activated pacemaker channel of brain. Cell *93*, 717-729.

Santoro, B., Piskorowski, R.A., Pian, P., Hu, L., Liu, H., and Siegelbaum, S.A. (2009). TRIP8b splice variants form a family of auxiliary subunits that regulate gating and trafficking of HCN channels in the brain. Neuron *62*, 802-813.

Santoro, B., Wainger, B.J., and Siegelbaum, S.A. (2004). Regulation of HCN channel surface expression by a novel C-terminal protein-protein interaction. J Neurosci *24*, 10750-762.

Scott, L.L., Hage, T.A., and Golding, N.L. (2007). Weak action potential backpropagation is associated with high-frequency axonal firing capability in principal neurons of the gerbil medial superior olive. J Physiol *583*, 647-661.

Scott, L.L., Mathews, P.J., and Golding, N.L. (2005). Posthearing developmental refinement of temporal processing in principal neurons of the medial superior olive. J Neurosci *25*, 7887-895.

Seidl, A.H., and Grothe, B. (2005). Development of sound localization mechanisms in the mongolian gerbil is shaped by early acoustic experience. J Neurophysiol *94*, 1028-036.

Simeone, T.A., Rho, J.M., and Baram, T.Z. (2005). Single channel properties of hyperpolarization-activated cation currents in acutely dissociated rat hippocampal neurones. J Physiol *568*, 371-380.

Slee, S.J., Higgs, M.H., Fairhall, A.L., and Spain, W.J. (2005). Two-dimensional time coding in the auditory brainstem. J Neurosci *25*, 9978-988.

Smith, P.H. (1995). Structural and functional differences distinguish principal from nonprincipal cells in the guinea pig MSO slice. J Neurophysiol *73*, 1653-667.

Smith, P.H., Joris, P.X., and Yin, T.C. (1993). Projections of physiologically characterized spherical bushy cell axons from the cochlear nucleus of the cat: evidence for delay lines to the medial superior olive. J Comp Neurol *331*, 245-260.

Stevens, D.R., Seifert, R., Bufe, B., Müller, F., Kremmer, E., Gauss, R., Meyerhof, W., Kaupp, U.B., and Lindemann, B. (2001). Hyperpolarization-activated channels HCN1 and HCN4 mediate responses to sour stimuli. Nature *413*, 631-35.

Stieber, J., Herrmann, S., Feil, S., Löster, J., Feil, R., Biel, M., Hofmann, F., and Ludwig, A. (2003). The hyperpolarization-activated channel HCN4 is required for the generation of pacemaker action potentials in the embryonic heart. Proc Natl Acad Sci U S A *100*, 15235-240.

Stieber, J., Wieland, K., Stöckl, G., Ludwig, A., and Hofmann, F. (2006). Bradycardic and proarrhythmic properties of sinus node inhibitors. Mol Pharmacol *69*, 1328-337.

Surges, R., Brewster, A.L., Bender, R.A., Beck, H., Feuerstein, T.J., and Baram, T.Z. (2006). Regulated expression of HCN channels and cAMP levels shape the properties of the h current in developing rat hippocampus. Eur J Neurosci *24*, 94-104.

Svirskis, G., Kotak, V., Sanes, D.H., and Rinzel, J. (2002). Enhancement of signal-to-noise ratio and phase locking for small inputs by a low-threshold outward current in auditory neurons. J Neurosci *22*, 11019-025.

Taraska J. W., & Zagotta W. N. (2007). Structure. In *Cyclic nucleotide-regulated ion channels: spotlight on symmetry..* United States:

Tinel, N., Diochot, S., Lauritzen, I., Barhanin, J., Lazdunski, M., and Borsotto, M. (2000). M-type KCNQ2-KCNQ3 potassium channels are modulated by the KCNE2 subunit. FEBS Lett *480*, 137-141.

Trussell, L.O. (1999). Synaptic mechanisms for coding timing in auditory neurons. Annu Rev Physiol *61*, 477-496.

Vasilyev, D.V., and Barish, M.E. (2002). Postnatal development of the hyperpolarization-activated excitatory current Ih in mouse hippocampal pyramidal neurons. J Neurosci *22*, 8992-9004.

Wahl-Schott, C., and Biel, M. (2009). HCN channels: structure, cellular regulation and physiological function. Cell Mol Life Sci *66*, 470-494.

Wahl-Schott, C., Baumann, L., Zong, X., and Biel, M. (2005). An arginine residue in the pore region is a key determinant of chloride dependence in cardiac pacemaker channels. J Biol Chem *280*, 13694-3700.

Wainger, B.J., DeGennaro, M., Santoro, B., Siegelbaum, S.A., and Tibbs, G.R. (2001). Molecular mechanism of cAMP modulation of HCN pacemaker channels. Nature *411*, 805-810.

Wang, D., and Brown, G.J. (2006). Computational auditory scene analysis (Piscataway, N.J.:

Wang, J., Chen, S., and Siegelbaum, S.A. (2001). Regulation of hyperpolarization-activated HCN channel gating and cAMP modulation due to interactions of COOH terminus and core transmembrane regions. J Gen Physiol *118*, 237-250.

Werthat, F., Alexandrova, O., Grothe, B., and Koch, U. (2008). Experience-dependent refinement of the inhibitory axons projecting to the medial superior olive. Dev Neurobiol *68*, 1454-462.

Wightman, F.L., and Kistler, D.J. (1992). The dominant role of low-frequency interaural time differences in sound localization. J Acoust Soc Am *91*, 1648-661.

Willms, A.R.(2002). NEUROFIT: software for fitting Hodgkin-Huxley models to voltage-clamp data. J Neurosci Methods *121*, 139-150.

Williams, S.R., Christensen, S.R., Stuart, G.J., and Häusser, M. (2002). Membrane potential bistability is controlled by the hyperpolarization-activated current I(H) in rat cerebellar Purkinje neurons in vitro. J Physiol *539*, 469-483.

Yamada, R., Kuba, H., Ishii, T.M., and Ohmori, H. (2005). Hyperpolarization-activated cyclic nucleotide-gated cation channels regulate auditory coincidence detection in nucleus laminaris of the chick. J Neurosci *25*, 8867-877.

Yin, T.C., and Chan, J.C. (1990). Interaural time sensitivity in medial superior olive of cat. J Neurophysiol *64*, 465-488.

Young, S.R., and Rubel, E.W. (1983). Frequency-specific projections of individual neurons in chick brainstem auditory nuclei. J Neurosci *3*, 1373-78.

Yu, H., Wu, J., Potapova, I., Wymore, R.T., Holmes, B., Zuckerman, J., Pan, Z., Wang, H., Shi, W., et al. (2001). MinK-related peptide 1: A beta subunit for the HCN ion channel subunit family enhances expression and speeds activation. Circ Res *88*, E84-87.

Yu, X., Chen, X.W., Zhou, P., Yao, L., Liu, T., Zhang, B., Li, Y., Zheng, H., Zheng, L.H., et al. (2007). Calcium influx through If channels in rat ventricular myocytes. Am J Physiol Cell Physiol *292*, C1147-155.

Yu, X., Duan, K.L., Shang, C.F., Yu, H.G., and Zhou, Z. (2004). Calcium influx through hyperpolarization-activated cation channels (I(h) channels) contributes to activity-evoked neuronal secretion. Proc Natl Acad Sci U S A *101*, 1051-56.

Zagotta, W.N., Olivier, N.B., Black, K.D., Young, E.C., Olson, R., and Gouaux, E. (2003). Structural basis for modulation and agonist specificity of HCN pacemaker channels. Nature *425*, 200-05.

Zhang, M., Jiang, M., and Tseng, G.N. (2001). minK-related peptide 1 associates with Kv4.2 and modulates its gating function: potential role as beta subunit of cardiac transient outward channel? Circ Res *88*, 1012-19.

Zhang, S., and Trussell, L.O. (1994). Voltage clamp analysis of excitatory synaptic transmission in the avian nucleus magnocellularis. J Physiol *480 (Pt 1)*, 123-136.

Zhao, M., and Wu, S.H. (2001). Morphology and physiology of neurons in the ventral nucleus of the lateral lemniscus in rat brain slices. J Comp Neurol *433*, 255-271.

Zolles, G., Klöcker, N., Wenzel, D., Weisser-Thomas, J., Fleischmann, B.K., Roeper, J., and Fakler, B. (2006). Pacemaking by HCN channels requires interaction with phosphoinositides. Neuron *52*, 1027-036.

Zolles, G., Wenzel, D., Bildl, W., Schulte, U., Hofmann, A., Müller, C.S., Thumfart, J.O., Vlachos, A., Deller, T., et al. (2009). Association with the auxiliary subunit PEX5R/Trip8b controls responsiveness of HCN channels to cAMP and adrenergic stimulation. Neuron *62*, 814-825.

Zong, X., Eckert, C., Yuan, H., Wahl-Schott, C., Abicht, H., Fang, L., Li, R., Mistrik, P., Gerstner, A., et al. (2005). A novel mechanism of modulation of hyperpolarization-activated cyclic nucleotide-gated channels by Src kinase. J Biol Chem *280*, 34224-232.

Zong, X., Stieber, J., Ludwig, A., Hofmann, F., and Biel, M. (2001). A single histidine residue determines the pH sensitivity of the pacemaker channel HCN2. J Biol Chem *276*, 6313-19.

VITA

Sukant Khurana attended The University of Delhi, Delhi, India from 1997 to 2000 to obtain Bachelor of Science (with honors) in Microbiology. From July 2000 to July 2003 he conducted learning and memory research at the National Center for Biological Sciences (Tata Institute of Fundamental Research), Bangalore, India, to obtain his Masters in Science (with specialization in molecular biology). He joined the Graduate program in Neuroscience at The University of Texas at Austin in August 2003 and has conducted research on the cellular properties of auditory brainstem neurons involved in sound localization. He has explored the role of voltage gated ion channels in regulating the responses of neurons of the medial superior olive.

Permanent Address: 15A Dhruv Apartments, Sector 13. Rohini, Delhi 110085, India

This manuscript was typed by the author.